

Washington University in St. Louis

## Washington University Open Scholarship

---

McKelvey School of Engineering Theses & Dissertations

McKelvey School of Engineering

---

Winter 12-15-2021

### Development and Application of a Novel Acoustic Microfluidic Technology for Single Cell per Well Trapping and High-Resolution Analysis of Cilia Motion in *Chlamydomonas Reinhardtii*

Mingyang Cui

*Washington University in St. Louis*

Follow this and additional works at: [https://openscholarship.wustl.edu/eng\\_etds](https://openscholarship.wustl.edu/eng_etds)



Part of the [Mechanical Engineering Commons](#)

---

#### Recommended Citation

Cui, Mingyang, "Development and Application of a Novel Acoustic Microfluidic Technology for Single Cell per Well Trapping and High-Resolution Analysis of Cilia Motion in *Chlamydomonas Reinhardtii*" (2021).

*McKelvey School of Engineering Theses & Dissertations*. 721.

[https://openscholarship.wustl.edu/eng\\_etds/721](https://openscholarship.wustl.edu/eng_etds/721)

This Dissertation is brought to you for free and open access by the McKelvey School of Engineering at Washington University Open Scholarship. It has been accepted for inclusion in McKelvey School of Engineering Theses & Dissertations by an authorized administrator of Washington University Open Scholarship. For more information, please contact [digital@wumail.wustl.edu](mailto:digital@wumail.wustl.edu).

WASHINGTON UNIVERSITY IN ST. LOUIS

McKelvey School of Engineering  
Department of Mechanical Engineering and Materials Science

Dissertation Examination Committee:

J. Mark Meacham, Chair

Philip V. Bayly

Susan K. Dutcher

Amit Pathak

Patricia Weisensee

Development and Application of a Novel Acoustic Microfluidic Technology for Single Cell per  
Well Trapping and High-Resolution Analysis of Cilia Motion in *Chlamydomonas Reinhardtii*

by

Mingyang Cui

A dissertation presented to  
The Graduate School  
of Washington University in  
partial fulfillment of the  
requirements for the degree  
of Doctor of Philosophy

December 2021  
St. Louis, Missouri

© 2021, Mingyang Cui

# Table of Contents

List of Figures .....	iv
Acknowledgments.....	viii
Abstract of the Dissertation .....	xi
Chapter 1: Introduction .....	1
1.1 Introduction to Microfluidics .....	1
1.2 Acoustic Microfluidics.....	3
1.3 Microorganism: <i>Chlamydomonas reinhardtii</i> .....	8
1.4 Specific Aims and Thesis Outline .....	11
1.4.1 Specific Aims.....	11
1.4.2 Thesis Outline .....	11
Chapter 2: Theory, Modeling, and Fabrication.....	13
2.1 Theory of Acoustofluidics.....	13
2.1.1 Basic Rules of Microfluidics.....	13
2.1.2 Ultrasonics in Fluid.....	16
2.2 Modeling .....	21
2.3 Fabrication.....	25
2.3.1 Interdigital Transducer Design and Fabrication.....	26
2.3.2 Microfluidic Channel Fabrication.....	27
Chapter 3: Thermal Considerations for Surface Acoustic Wave (SAW) Devices .....	30
3.1 Introduction .....	31
3.2 Methods.....	36
3.2.1 Device Fabrication .....	36
3.2.2 Cell Culture and Preparation.....	38
3.2.3 Experimental Setup.....	38
3.2.4 Video Microscopy.....	39
3.2.5 Infrared Imaging and Analysis.....	39
3.4 Results and Discussion.....	42
3.3.1 Thermal Response of 10 MHz Devices .....	43
3.3.2 <i>C. reinhardtii</i> Trap-and-Release in 10 MHz Devices .....	45
3.3.3 Thermal Response and <i>C. reinhardtii</i> Trap-and-Release in 25 MHz Devices.....	47

3.4	Conclusions .....	50
Chapter 4: Cilia Dynamics Probing .....		53
4.1	Introduction .....	53
4.2	Trapping and Patterning Cell Populations .....	56
4.2.1	Cell Patterning in Square/Diamond Chambers .....	57
4.2.2	Cell Patterning in Circular Chambers .....	61
4.3	Single Cell Trapping .....	62
4.3.1	Cilia Waveform Probing .....	63
4.3.2	Observation of Cell Helical Motion in Biciliate <i>C. reinhardtii</i> .....	71
4.3.3	Analysis of Cilia Synchronization in Biciliate <i>C. reinhardtii</i> .....	73
4.3.4	Perturbation of Cilia Motion in Uniciliate <i>C. reinhardtii</i> .....	78
4.3.5	Acoustic Effects on Cilia Beating .....	81
4.3.6	Temperature Effects on Cilia Beating .....	83
4.3.7	Hybrid Acoustofluidic Systems for Manipulating Other Particles and Cells .....	86
4.4	Conclusion.....	87
Chapter 5: Optimization and Pressure Mapping of BAW/SAW devices .....		89
5.1	Introduction .....	89
5.2	Optimization of BAW/SAW Devices .....	90
5.3	Pressure Mapping of Glass-Based SAW Devices.....	94
5.4	Summary .....	97
Chapter 6: Conclusion.....		98
6.1	Summary of Work.....	98
6.2	Limitations, and Future Directions .....	99
6.3	Final Thoughts.....	101
References.....		102

# List of Figures

**Figure 1.1.** A schematic of a typical bulk acoustic wave (BAW) device using a piezoelectric transducer to generate rigid structure vibrations. When the operating frequency matches the dimension of the microfluidic chamber (width), strong standing bulk acoustic waves (SBAWs) are formed inside of the fluidic chamber. .... 4

**Figure 1.2.** A schematic of a surface acoustic wave (SAW) device generating standing surface acoustic waves (SSAWs) on a piezoelectric substrate using a pair of interdigital electrodes. The SSAWs on the substrate surface leak into the fluid chamber and form SSAWs inside of the fluidic chamber. The PDMS channel has a similar acoustic impedance as the fluid; thus, the reflection of waves by the PDMS channel walls can be neglected..... 5

**Figure 1.3.** (a) Transmitted light microscopy of cilia motion for a wild-type biciliated *C. reinhardtii* cell over one beat cycle in an acoustic trap. (b) A schematic image of *C. reinhardtii*, whose cell body is about 7–8  $\mu\text{m}$  in diameter and with a cilia length of about 8–10  $\mu\text{m}$ . Courtesy of Minji Kim. .... 9

**Figure 2.1.** Geometry of a full 2D cross section finite element model. The substrate is lithium niobate, which is 500  $\mu\text{m}$  thick. The PDMS slab is on top, which is 3 mm wide and 1.5 mm tall. The channel is 545  $\mu\text{m}$  wide and 50  $\mu\text{m}$  tall. To reduce the computational cost, only three pairs of IDTs are modeled. .... 22

**Figure 2.2.** (a) Illustration of 10  $\mu\text{m}$  PS beads focusing in a 9.6 MHz PDMS-based SAW device. (b) The acoustic radiation force dominated as the 10  $\mu\text{m}$  PS beads moved to pressure nodes or local pressure minima. .... 24

**Figure 2.3.** (a) Illustration of 1  $\mu\text{m}$  PS beads focusing in a 9.6 MHz PDMS-based SAW device. (b) The Stokes drag force dominated as the 1  $\mu\text{m}$  PS beads move with acoustic streaming flow all the time..... 24

**Figure 2.4.** Illustration of glass channel wet-etching process and ‘stamp and stick’ bonding method using SU-8 as an adhesive layer. Color corresponds to the type of material used. .... 25

**Figure 2.5.** Illustration of IDTs fabrication process and PDMS channel fabrication process. A thin photoresist was spin-coated on lithium niobate first, followed by metal layer and  $\text{SiO}_2$  deposition. The color references to Figure 2.4. .... 26

**Figure 3.1.** Trap-and-release illustration and mechanisms of PDMS-based and glass-based SAW device operation. (a) A standing acoustic field first traps (acoustic field on) and then releases (field off) *C. reinhardtii* cells. When trapped, the acoustic radiation force  $F^{\text{ac}}$  balances the swimming capability of the cells (characterized by a swimming velocity  $U_0$  and reorientation time  $\tau$ ). (b) PDMS-based SAW device mechanism: standing substrate acoustic waves (SSAWs) leak into the fluid channel and generate standing waves; glass-based SAW device mechanism: SSAWs leak into the fluid chamber and generate standing bulk acoustic waves (SBAWs). (c) Acoustic trap-and-release experiment in a glass-based SAW device. (d) Top-view of a glass-

based SAW device. (e) Device mounted on a temperature-controlled stage insert. Note that temperature control is not used during the current trap-and-release experiments to assess the effect of temperature rise on cell viability. .... 35

**Figure 3.2.** Infrared (IR) thermography experimental setup. (a) Top view of a glass-based SAW device with black paint (BP). (b) A bottom-view IR image of a PDMS-based channel during actuation. The region of interest (ROI) inside the channel is  $180\ \mu\text{m} \times 540\ \mu\text{m}$ . (c) The custom assembly used for temperature measurements. .... 40

**Figure 3.3.** Comparison of the thermal response within the ROI for uncoated devices and devices with BP when the channel is loaded with cell medium. (a) PDMS-based SAW device comparison. (b) Glass-based SAW device comparison. Experimental duration is 120 s, 30 s with the signal on and 90 s off. .... 41

**Figure 3.4.** Heat maps of a 10 MHz PDMS-based SAW device (experimental actuation frequency  $f = 9.62\ \text{MHz}$ ). (a) The thermal response of the region between the IDTs for different drive voltages ( $V = 5\text{--}25\ \text{V}_{\text{pp}}$ ). Cases highlighted in red indicate possible cell death due to heat stress. (b) Progression of the ROI temperature  $T_{\text{ROI}}$  for different drive voltages. The *C. reinhardtii* thermotolerance threshold ( $T = \sim 37\ ^\circ\text{C}$ ) is shown for reference. .... 44

**Figure 3.5.** Progression of  $T_{\text{ROI}}$  for PDMS-based SAW, glass-based SAW, and no-channel SAW devices. (a) The  $T_{\text{ROI}}$  of glass-based SAW and no-channel SAW are under the *C. reinhardtii* thermotolerance threshold throughout the experiment. (b) Heat maps at 30 s, the time of maximum device temperature. .... 45

**Figure 3.6.** Trap-and-release at 9.62 MHz and 25 V<sub>pp</sub>. (a) The PDMS-based device is not able to trap swimming *C. reinhardtii* but focuses immotile cells. Immotile *C. reinhardtii* cells do not redistribute after the signal is turned off. (b) The glass-based device successfully traps live *C. reinhardtii* at SBAW nodal positions. The motile *C. reinhardtii* cells redistribute evenly throughout the channel after the signal is removed. .... 46

**Figure 3.7.** Thermal response and trap-and-release are correlated for the 24 MHz device operated at 24.05 MHz and 25 V<sub>pp</sub>. (a) The  $T_{\text{ROI}}$  progression of PDMS-based and glass-based SAW devices. (b) The PDMS-based device is not able to trap swimming *C. reinhardtii*, which become immotile at  $\sim 20\ \text{s}$ . (c) The glass-based device is able to trap-and-release live cells. .... 48

**Figure 3.8.** Brightfield microscopy images of heat-induced damage to *C. reinhardtii* cells after trap-and-release in the PDMS-based microchannel driven at 24.05 MHz and 25 V<sub>pp</sub>. .... 49

**Figure 4.1.** Square chamber cell trapping for BAW driven by SAW device. (a) A random pattern formed by *C. reinhardtii* at  $\sim 10\ \text{MHz}$ ; the side length of the microfluidic chamber is  $545\ \mu\text{m}$ . (b) One dimensional cell pattern formed in  $\sim 20\ \text{MHz}$  devices; the side length of the microfluidic chamber is  $270\ \mu\text{m}$ . .... 58

**Figure 4.2.** Cell patterning matrices. (a) 5 x 5 nodal positions for a 6.6 MHz device, (b) 6 x 6 for a 8.1 MHz device, (c) 7 x 7 for a 9.6 MHz device, and (d) 7 x 7 for a  $\sim 20\ \text{MHz}$  device. Chambers

for (a)-(c) have a side length of 545  $\mu\text{m}$ , while the chamber for (d) has a side length of 270  $\mu\text{m}$ .  
..... 60

**Figure 4.3.** Cells patterned in concentric ring shapes at  $\sim 10$  MHz and  $\sim 20$  MHz. (a) The circular chamber resonant shape of a  $\sim 10$  MHz device. (b)  $\sim 20$  MHz device resonance imaged using swimming *C. reinhardtii*. The circular chamber in (a) has a diameter of 545  $\mu\text{m}$ , while the chamber in (b) has a diameter of 270  $\mu\text{m}$ . ..... 61

**Figure 4.5.** Acoustic trapping of individual unciliated and biciliated wild-type *C. reinhardtii* cells. (a) Unciliated cell (*uni1*) in an acoustic trap. (b) Biciliated cell (CC125) in an acoustic trap. .... 64

**Figure 4.6.** Quantification of periodicity of ciliary beating. Example plot of the normalized autocovariance of the cilium tangent angle  $a_c(\tau)$ , plotted versus the time lag,  $\tau$ . The period of beating is defined by the first peak with a magnitude greater than a specified threshold (0.15) at a nonzero lag (red circle). ..... 65

**Figure 4.7.** Dimensionless waveforms of each cilia group. (a) Representative dimensionless waveform of the *cis*-cilium of CC125. (b) Representative dimensionless waveform of the *trans*-cilium of CC125. (c) Representative dimensionless waveform of the *uni1* unciliated mutant. .. 67

**Figure 4.8.** A detailed comparison of key waveform parameters between the *cis*-cilium and *trans*-cilium during a ‘slip’ motion. (a) Amplitude comparison of the *cis*-cilium and *trans*-cilium. The *cis*-cilium has periodic beating during asynchrony, however, the *trans*-cilium beats faster during asynchrony, which highlighted by the red dashed line. (b) Waveform comparison of the *cis*-cilium and *trans*-cilium during asynchrony. (c) Mean beat frequency, waveform shape comparison ((d) amplitude and (e) curvature) during ‘slip’ motion. .... 70

**Figure 4.9.** Rotation frequency comparison for biciliated *C. reinhardtii* cells in an acoustic trap at different temperatures ranging from 15  $^{\circ}\text{C}$  to 25  $^{\circ}\text{C}$ . ..... 73

**Figure 4.10.** Frequency comparison of the *cis*-cilium and *trans*-cilium groups. For both groups, the frequency decreases with increasing viscosity..... 74

**Figure 4.11.** Amplitude comparison of the *cis*-cilium and *trans*-cilium groups. (a) *cis*-cilium and (b) *trans*-cilium. .... 75

**Figure 4.12.** Curvature comparison of the *cis*-cilium and *trans*-cilium groups. (a) *cis*-cilium and (b) *trans*-cilium. .... 76

**Figure 4.13.** Histograms of response of cilia to varied fluid viscosity. The asynchronization appears to increase as viscosity increased. The trending of asynchrony to a high beat frequency ratio ( $f\text{-cis}/f\text{-trans}$ ) is clearly shown as viscosity increases. .... 77

**Figure 4.14.** Examples of cell body rotation speed increasing with acoustically induced translation (a)-(c) and decreasing (d)-(f), respectively. .... 79

**Figure 4.15.** A unciliated cell (*uni1*) that is rotating around its cell body (a) out of and (b) in an acoustic field. .... 82

<b>Figure 4.16.</b> A uniciliated cell ( <i>uni1</i> ) that is rotating around its cell body (a) frequency comparison (b) amplitude comparison (c) curvature comparison. ....	82
<b>Figure 4.17.</b> Uniciliated cells ( <i>uni1</i> ) exposed to an acoustic field for 60 seconds at various setpoint temperatures. Median and interquartile ranges of frequency in the whole actuation period is shown. ....	84
<b>Figure 4.18.</b> Waveform shape comparison (amplitude and curvature) for uniciliated cells ( <i>uni1</i> ) exposed to an acoustic field for 60 seconds at various setpoint temperatures. ....	85
<b>Figure 4.19.</b> Passive particles trapping using BAW/SAW system at ~6.6 MHz. ....	87
<b>Figure 5.1.</b> Fabrication process of thin glass/Si BAW/SAW devices. An Si wafer with Si <sub>3</sub> N <sub>4</sub> on both sides was used to fabricate acoustofluidic channels. After etching the microfluidic channels using DRIE, Si <sub>3</sub> N <sub>4</sub> was removed from one side using RIE, and the Si wafer was anodically bonded with thin glass (~175 μm thick). The other side of the Si wafer was first wet etched to a depth that was near to the designed channel height. Then, the bottoms of the Si channels were etched through by RIE. The thin-Si/glass channels were then bonded to the SAW substrate using the previously described method from Chapter 2. ....	91
<b>Figure 5.2.</b> The thin-Si/glass diamond channel on LiNbO <sub>3</sub> with IDTs. The channel walls are made of silicon that is 25 μm thick. The channel top is sealed by thin glass (~175 μm), which allows for oil-immersion microscopy. ....	92
<b>Figure 5.3.</b> The acoustic cell patterning to form 8 x 8 matrices in (a) 10 MHz and (b) 20 MHz thin Si/glass BAW/SAW devices. The input power that drives the IDTs was lower compared to that needed for the previously described thin-glass BAW/SAW devices. In addition, the patterns are more uniform. ....	93
<b>Figure 5.4.</b> Resonance identification for glass-based SAW device with a straight fluidic channel. The five images at the top show cell distributions at peaks of the correlation coefficient, which can be easily identified as resonant frequencies. ....	94
<b>Figure 5.5.</b> Qualitative mapping of the acoustic field amplitude for the fifth half-wavelength resonance of the glass-based SAW device with a straight channel. Acoustic potential, brightfield images, heat maps of the cell distribution density, and line plots of cell distribution density summed along the channel length with increasing voltage. The pressure, the acoustic radiation force, and normalized cell distribution density are shown on the bottom-right. ....	96

# Acknowledgments

Prof. J. Mark Meacham, I still remember the first time when we met in your office back five years ago in Urbauer Hall. I did not believe that I could make it through a PhD program someday. Thank you for giving me a chance to try it out. It is your guidance that makes me alive on various disparate projects over the past years. Your guidance and encouragement makes me stronger when I am down in both work and life, which I will remember forever.

Prof. Phil Bayly, you have always been there for me with your thoughtful ideas on the cilia project, great guidance in academia, and constructive feedback on everything I asked. I learned so much from your management of time, leadership in Bayly Lab and MEMS department. I am blessed to have you advise me during my PhD thesis work.

I would like to express my thanks to my other committee members. Prof. Susan Dutcher, your enthusiasm, and achievements in academia will influence me forever. I am so grateful for your incisive perspectives in cilia research. Prof. Amit Pathak, I got so much help from you since taking your continuum mechanics class, further in teaching assistant experience under your guidance, and other personal help in academia. I will always remember your advice and encouragement when I was in a difficult situation. Prof. Patricia Weisensee, to be honest, without the facilities from your lab, I don't think I could finish my PhD work so smoothly. It is so lucky to have your lab being a great and generous neighbor of the Meacham Lab.

I have worked with many collaborators during my PhD career, both inside and outside Wash U. Their intelligence, eagerness, and kindness to instruct students with lofty ambitions will encourage me to do my best in my future career. I am eternally grateful to them: Prof. Richard Cote, Prof. Peter Goedegebuure, Prof. Guy Genin, Prof. Mark Watson, Prof. Ram Dixit, Prof. Mark Thompson from USC, Prof. Chongwu Zhou from USC, Prof. Siyang Zheng from CMU,

etc. I was very luck to work with Dr. Mathieu Bottier, for his kindly guidance when I started on the cilia project. Lastly, I would express my special thanks to Dr. Ye Bi, who taught me to do cell assay work over half a year. I will remember her guidance on doing cell experimental work, and endless patience in helping me understand the most fundamental aspects of cell biology.

To Meacham lab members and alumni: Dr. Michael Binkley and Dr. Wenming Li, I started shadowing cleanroom fabrication and experiments from you. I will always remember your patience when you taught me design, fabrication, and experimental testing. Dr. Minji Kim and Dr. Husain Shekhani gave me so much help on the cilia project, from learning basics to performing experiments. I would also express my thanks to current Meacham Lab members, Dr. Li Shan and Andreea Stoica, for being with me as sincere friends and great lab mates. Lastly, I want to give my best wishes to Maggie Ruding and Advaith Narayan, for having a great graduate experience.

I am fortunate in my life of being a son of my parents. Without their unconditional support and motivation, I would have been doomed from the beginning. I am so lucky to have my sister with me all the time, for keeping me calm, and having fun in life. I am blessed to have my girlfriend with me. Her support, encouragement, and love made me through this special journey in my life.

Nothing in my academic career and life was without help. I will always be grateful and remember all these people who helped or will help me to get through this life long journey.

Mingyang Cui(崔明阳)

*Washington University in St. Louis*

*December 2021*

*Dedicated to my grandparents Wenhua Zhao and Xiangting Wei,  
and my beloved cousin Yangyang Guo*

## ABSTRACT OF THE DISSERTATION

Development and Application of a Novel Acoustic Microfluidic Technology for Single Cell per Well Trapping and High-Resolution Analysis of Cilia Motion in *Chlamydomonas Reinhardtii*

by

Mingyang Cui

Doctor of Philosophy in Mechanical Engineering

Washington University in St. Louis, 2021

Professor J. Mark Meacham, Chair

Acoustic manipulation of cells and microorganisms is a label-free and contact-free technique with promise for biological and biomedical applications. When exposed to an ultrasonic standing wave field, particles suspended in microfluidic channels will be moved to pressure minima (nodes) or maxima (antinodes) due to the acoustic impedance mismatch between particles and the suspension medium.

Cilia motion is fundamental to understanding biological and biomedical problems related to dysfunctional human cilia, including primary ciliary dyskinesia, blindness, and male infertility. However, *in vivo* and *ex vivo* mammalian ciliated cell research is laborious and time-consuming due to difficulty in growing, maintaining, and imaging these cells. Therefore, *Chlamydomonas reinhardtii* (*C. reinhardtii*), a unicellular alga, has long been used as a genetic and biomedical research model to study cilia. Unfortunately, traditional micropipette-based trapping methods are also laborious and have many limitations including a requirement for physical-contact and being low throughput. So, it is urgent to develop a robust method to trap and study *C. reinhardtii* cells.

In my doctoral research, I developed a novel acoustic technique to trap and analyze *C. reinhardtii*. First, I completed a thermal analysis of surface acoustic wave (SAW) devices for trapping individual and populations of swimming *C. reinhardtii* without thermal damage. This study showed that only glass-based SAW can be used to trap swimming *C. reinhardtii*. Then, I developed a novel acoustic technique to generate two-dimensional standing bulk acoustic waves (BAW) driven by one pair of SAW transducers, which allows trapping and manipulating individual *C. reinhardtii* with high temporal and spatial resolution. Lastly, cell and cilia dynamics were studied assisted by this novel technique. These studies included probing cilia waveforms, quantitative assessment of *C. reinhardtii* helical motion, analysis of cilia dynamics variations due to increased fluid viscosity, and the effects of rapid acoustically driven cell translation.

# **Chapter 1: Introduction**

This dissertation focuses on the manipulation of motile microorganisms and probing of their dynamics using novel acoustic microfluidic devices. This introductory chapter describes the current state of the art acoustic microfluidic technologies for biological and biomedical applications. As the general introduction to this thesis, it includes an overview of microfluidics and its classification, the state of the art and challenges of acoustic microfluidics, and general particle manipulation using acoustofluidics. Background information on the motile microorganism, *Chlamydomonas reinhardtii* (*C. reinhardtii*), is also introduced. Finally, the chapter concludes with a summary of the thesis and an outline of specific topics of the doctoral work.

## **1.1 Introduction to Microfluidics**

Microfluidics, a study of particle and fluid manipulation in submillimeter-sized systems, has emerged as a revolutionary platform in biology, chemistry, and medicine.<sup>1-5</sup> The microfluidic devices are often referred to as lab-on-a-chip (LOC) referring to the concept of shrinking of an entire laboratory to a chip. The promise of microfluidic technology, compared to traditional laboratory techniques in chemistry and biomedicine, includes platform miniaturization, low cost, reduced reagent and sample consumption, automation, precise microenvironmental control, and rapid production cycles. At the microscale level, the flow is usually completely laminar (i.e., no turbulence occurs) as the viscosity dominates over inertia in this low Reynolds number regime. In addition, the surface forces, such as surface tension and gradients and shear stresses, become dominant. However, the volume forces, such as gravity and inertia, which are very evident in our daily life, are largely unimportant. Due to these characteristics in microfluidics, researchers have

continued to introduce new physics into the microlevel systems to improve their versatility, functionality, and performance. A variety of microfluidic platforms have been developed, depending on the physics underlying the particular method. These methods are classified as hydrodynamic,<sup>6-9</sup> electric,<sup>10-12</sup> magnetic,<sup>13-15</sup> optical,<sup>16, 17</sup> and acoustic.<sup>18-20</sup> Each method utilizes either an external force or internal dynamic fluidic forces, and each force type presents its pros and cons. The following introduction is focused on cell or particle manipulation.

Hydrodynamic microfluidics, also known as inertial microfluidics, is a passive microfluidic technology depending entirely on the channel geometry or intrinsic hydrodynamic forces. Compared to other active microfluidic platforms, this method is simple, robust, and relatively high-throughput.<sup>6, 7, 21, 22</sup> Inertial microfluidics works in an intermediate Reynolds number range ( $\sim 1 < Re < \sim 100$ , where both fluidic inertia and viscosity are finite), which brings about interesting inertial effects, such as inertial migration and secondary flow that form the fundamentals of inertial microfluidics. Continuous particle and bioparticle trapping, sorting, focusing, and separation have been demonstrated using this method, for which representative work and comprehensive reviews can be found in cited references.<sup>7, 23</sup>

Electric microfluidics is an active method that uses electrical forces to manipulate particles and fluids. Depending on whether the electric forces act on fixed or induced charge of particles, this technique can be classified into electrophoresis (EP) or dielectrophoresis (DEP).<sup>11, 12, 24, 25</sup> In EP case, the charged particles experience electrical forces that move them to the electrode that has the opposite charge polarity when a uniform electric field is applied, while the neutral particles are not affected. However, in DEP case where a nonuniform electric field is applied, a net DEP force can also be generated on a neutral particle. The interaction of a

particle's dipole and the electrical gradient results in the force magnitude difference at each end of the particle. For detailed theory and applications, please check the cited references.<sup>26-28</sup>

In magnetic microfluidics, magnetic or magnetically labeled particles migrate in a magnetic field.<sup>13, 14, 29, 30</sup> Particle manipulation using this method can be classified into positive magnetophoresis – the magnetic particles move in diamagnetic medium; or negative magnetophoresis – the diamagnetic particles moves in magnetic medium. The performance of magnetophoresis is highly dependent on several key parameters, such as the magnetic permeability, the magnetic flux density, and the susceptibility. Some recent reviews and state of the art articles can be found in the cited references.<sup>31, 32</sup>

The method of manipulating particles in optical microfluidics, also known as ‘optical tweezers’, was first demonstrated by Arthur Ashkin, Steven Chu, and colleagues in 1986.<sup>33</sup> When exposed to a highly focused laser beam, particles that are much smaller than the light's wavelength will move along the electric field gradient, due to the electric dipole moment generated on the particle. This well-established and high precision method is a great tool to manipulate single cells or particles.<sup>34</sup> More detailed explanation and applications of this method can be found in review articles and classical or recent publications listed in the cited references.<sup>35-37</sup>

Finally, acoustic microfluidics uses ultrasonic waves to manipulate micro- or nanoparticles or fluids.<sup>38, 39</sup> I will introduce this approach in more detail in the following section, as this is the main method used in my research.

## **1.2 Acoustic Microfluidics**

Acoustic microfluidics, also known as acoustofluidics, are useful tools to manipulate micro- or nanoscale particles or fluids using ultrasonics. Acoustofluidics permits non-contact, label-free

particle manipulation, which minimizes the potential for undesirable surface interactions and physical stress on sensitive biological samples, making this technique a promising tool for chemical, biological, or biomedical research. Based on the operating mechanisms, the acoustic microfluidic systems can be categorized into two kinds: bulk acoustic waves (BAWs) and surface acoustic waves (SAWs).

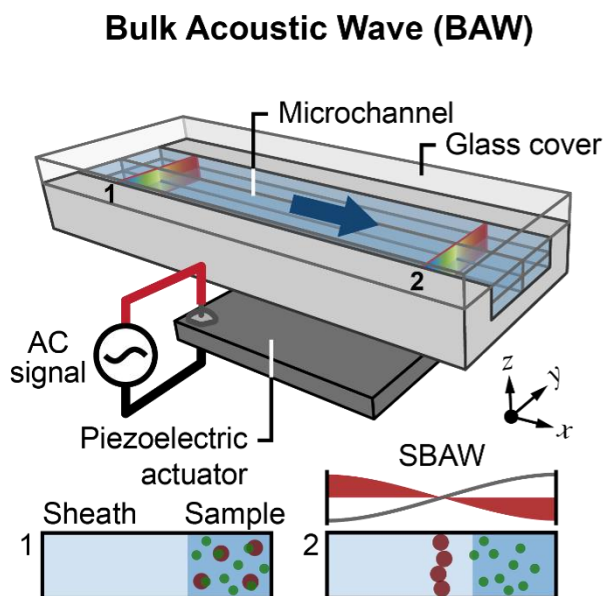


**Figure 1.1.** A schematic of a typical bulk acoustic wave (BAW) device using a piezoelectric transducer to generate rigid structure vibrations. When the operating frequency matches the dimension of the microfluidic chamber (width), strong standing bulk acoustic waves (SBAWs) are formed inside of the fluidic chamber.

Bulk acoustic waves are defined as compressional waves in a solid that propagate through the bulk material. Shown in Figure 1.1 is a schematic of a typical BAW system, which is comprised of a piezoelectric transducer and a fluidic microchannel made of silicon, glass, metal or other high acoustic impedance materials. When an electrical field (alternating current) is applied on piezoelectric transducers, the electrical signal is converted into mechanical vibrations, which is known as the inverse piezoelectric effect. The actuation frequency must match the dimension of the microfluidic chamber (width for most cases), so that standing bulk acoustic

waves (SBAWs) can be generated inside of the fluidic chamber. However, due to the material limitations, BAW are usually operated at low frequency range (tens of kHz to ~10 MHz).

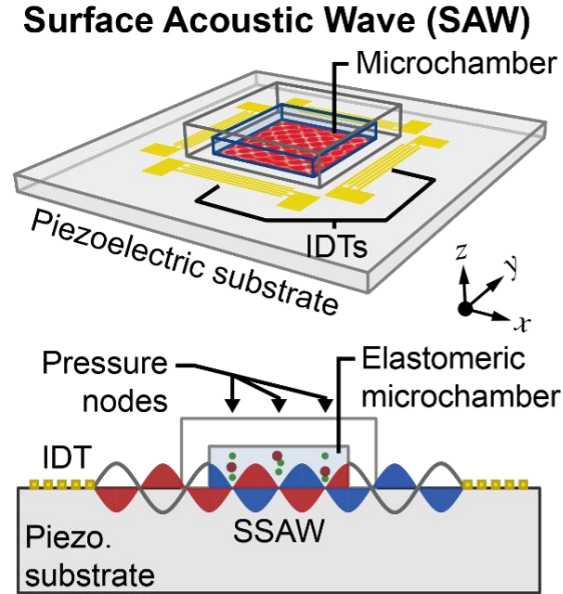


**Figure 1.2.** A schematic of a surface acoustic wave (SAW) device generating standing surface acoustic waves (SSAWs) on a piezoelectric substrate using a pair of interdigital electrodes. The SSAWs on the substrate surface leak into the fluid chamber and form SSAWs inside of the fluidic chamber. The PDMS channel has a similar acoustic impedance as the fluid; thus, the reflection of waves by the PDMS channel walls can be neglected.

Surface acoustic waves are defined as waves that propagate along the surface of a material. Shown in Figure 1.2 is a schematic of a typical SAW system, which is comprised of interdigital transducers (IDTs) and a fluidic microchannel made of an elastomeric material. The IDTs are made by different designs of finger-spaced metal electrodes deposited on top of a piezoelectric substrate material, such as lithium niobate ( $\text{LiNbO}_3$ ). The fluidic microchannel is made of polydimethylsiloxane (PDMS) to match the acoustic impedance of fluids, which minimizes reflected waves inside of the fluidic chamber. Standing waves inside the fluidic chamber are formed by standing surface acoustic waves (SSAWs) on the piezoelectric substrate

that ‘leak’ into the fluid domain. This technique is good for operating at high frequency, typically from ~10 MHz to hundreds of MHz or even higher up to the gigahertz range.

In both cases, standing waves are generated in the fluidic domain. Particles suspended in the fluidic domain experience acoustic radiation forces from scattering of acoustic waves. The motion of particles suspended in the liquid is controlled by the acoustic radiation force and the fluidic drag, based on the particle size, density, and compressibility relative to that of the fluid. More details about the theory can be found in the following chapter.<sup>40-43</sup>

Another effect observed is called acoustic streaming, which is a steady fluid flow formed by viscous attenuation of an acoustic wave. However, it is often misunderstood due to its many forms that arise. Thus, it is also seen as problematic because of its inadvertent generation inside of acoustofluidic devices. Whilst it is sometimes undesirable and can be seen in a bad light, when used correctly it can be utilized to overcome challenges in low Reynolds number flows, such as pumping, mixing, and sorting. As this thesis is focus on manipulation of *Chlamydomonas reinhardtii* (6-8  $\mu\text{m}$  in diameter) that exceeds a threshold size where the acoustic streaming phenomenon are thought to be important, the effect of acoustic streaming can be neglected. More information about acoustic streaming can be found in the cited references.<sup>44-50</sup>

Acoustofluidic methods can be used in various applications such as oscillation, wettability manipulation, pumping, jetting, atomization, and particle manipulation inside of closed environments or sessile drops.<sup>51-55</sup> Due to the topic of this thesis, it focuses on introducing particle manipulation (sorting, trapping, and separation) inside of microfluidic channels using acoustic waves. For interested readers, review articles of applications of acoustics can be found in the cited references.<sup>38, 56</sup>

Using BAW, Antfolk *et al.* separated tumor cells from white blood cells with a high recovery rate, using a single inlet two-stage acoustophoresis chip.<sup>57</sup> Ku *et al.* successfully enriched extracellular vesicles from cell culture conditioned media, urine, and blood plasma.<sup>58</sup> Binkley *et al.* recently demonstrated nanoscale molecular synthesis and detection using a novel longitudinal standing bulk acoustic wave device.<sup>59, 60</sup> Similarly, utilizing SAW, Wu *et al.* were able to separate circulating tumor cells from white blood cells, using a high-throughput acoustic platform.<sup>61</sup> Collins *et al.* used high-frequency SAW devices to separate and trap single human lymphocyte cells and red blood cells infected by malarial parasites.<sup>62</sup> Recently, Richard *et al.* used an advanced two-stage SAW device to enrich platelets in an SU-8-based channel at whole blood concentration.<sup>63</sup>

Though many successful implementations of acoustofluidic devices have been reported, only a few studies have demonstrated trapping and manipulation of swimming particles, because the acoustic radiation force needed to manipulate such particles is high leading to sample damage by thermal or electrical stimulation. Ding *et al.* were able to trap and manipulate *Caenorhabditis elegans* using pairs of orthogonally arranged chirped IDTs in a SAW system.<sup>19</sup> Kim *et al.* quantified the swimming motility of *C. reinhardtii* and its mutants using BAW.<sup>64</sup> Takatori *et al.* used a single-beam transducer to trap active Janus particles and assess their swimming pressure.<sup>65</sup> Thus, using surface acoustic waves to trap *C. reinhardtii* is promising but also challenging due to the device's high flexibility and low trapping force. In this thesis, I describe the design and fabrication of surface acoustic wave devices that are able to meet this challenge and trap single *C. reinhardtii* cells. More information on this microorganism is introduced in the following section.

### 1.3 Microorganism: *Chlamydomonas reinhardtii*

*Chlamydomonas reinhardtii* (*C. reinhardtii*) has been used as a biological model for cilia research because of its structural and dynamical similarity to human cilia. One goal of my doctoral research is focused on trapping individual *C. reinhardtii* and probing its swimming dynamics.

Motile flagellated/ciliated organisms generate oscillatory propulsive waveforms that can move themselves and surrounding fluids.<sup>66</sup> Cilia can be found in human organs, such as kidneys, lungs, the brain, and the reproductive system. The motion of cilia plays an important role to maintain organ function, such as to keep airways clear of dirt and mucus, move cerebrospinal fluid in the brain, and help propel sperm in the reproductive system. However, dysfunctional cilia exhibit non-motile or impaired motility and are considered or suspected to cause cilia-related disorders (ciliopathies), including primary ciliary dyskinesia (PCD), blindness, and male infertility.<sup>67-71</sup> Cilia motion is fundamental to understanding biological and biomedical problems related to cilia, but the mechanism of cilia motion remains a mystery. Therefore, understanding the mechanism of cilia motion provides a framework for understanding oscillations and waves, complementary to imaging, genetics and cell biology.

Unfortunately, like much biological and biomedical research, *in vivo* and *ex vivo* mammalian ciliated cell research is laborious and time-consuming, and such samples are difficult to grow, maintain, and image. In cilia research, *C. reinhardtii*, a unicellular alga, is used as a genetic and biomedical research model.<sup>72-74</sup> The wild-type *C. reinhardtii* cell body is 6–8  $\mu\text{m}$  in diameter and incorporates two cilia that are 10–12  $\mu\text{m}$  long and ~200 nm in diameter, and that propel the cell body movement as shown in Figure 1.3.

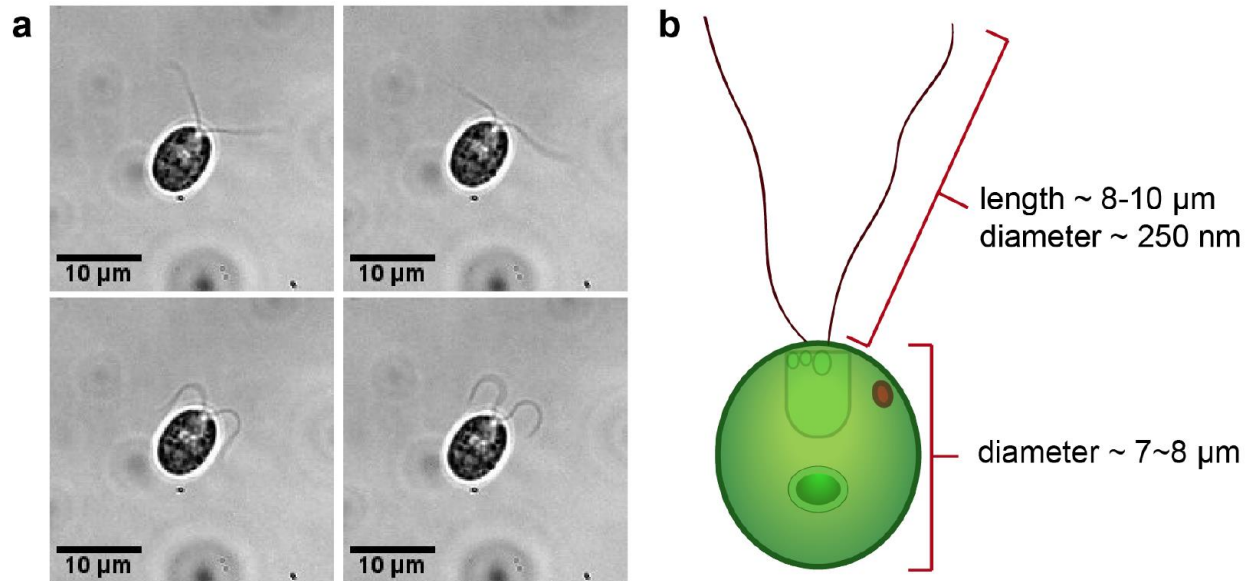


**Figure 1.3.** (a) Transmitted light microscopy of cilia motion for a wild-type biciliated *C. reinhardtii* cell over one beat cycle in an acoustic trap. (b) A schematic image of *C. reinhardtii*, whose cell body is about 7–8  $\mu\text{m}$  in diameter and with a cilia length of about 8–10  $\mu\text{m}$ . Courtesy of Minji Kim.

Wild-type *C. reinhardtii* cilia are a useful model for cilia research because both its structure and beating waveform are strikingly similar to human cilia. *C. reinhardtii* cilia share a common axonemal structure with mammalian cilia. The axoneme of cilia is composed of a central pair of two microtubule singlets connected by radial spokes to the surrounding nine microtubule doublets ('9+2' axoneme).<sup>75</sup> The surrounded microtubule doublets are connected to each other by the nexin-dynein regulatory complex.

Aside from structure equivalency to mammalian cilia, the *C. reinhardtii* cilia waveform is also surprisingly similar to that of human cilia. Wild-type *C. reinhardtii* cilia usually exhibit an asymmetric waveform (like human lung cilia) to propel the cell forward, but they can also beat symmetrically (like sperm cilia) to propel the cell backward. Genetic mutations and chemical treatment can be used on *C. reinhardtii* to vary parameters and test hypotheses related to cilia

motion. Thus, valuable insight into cilia behavior can be gained by probing and characterizing cell body motion and cilia waveform during swimming.

Different approaches have been used to study how structural ciliary defects can be related to impaired cilia motility. High-resolution optical microscopic imaging has been used to trace and characterize cilia waveform.<sup>76,77</sup> Computational modeling has been established to complement the experimental study of cilia beating waveform generation.<sup>78-82</sup> Electron microscopy and cryo-electron tomography are used to identify the main structure of the cilia axoneme.<sup>83-85</sup> However, due to limitations of each technique, trapping wild-type *C. reinhardtii* is needed using a robust method that has no physical contact, and is high-throughput, easy to operate, allows long time and high-resolution observation, and is biocompatible. Part of this thesis developed a method that meets all requirements.

Lastly, *C. reinhardtii* cells are easy to prepare and culture in the lab. Gametes of *C. reinhardtii* cells are relatively uniform in size, which is ideal for cilia dynamics probing during acoustic trapping. In addition, a wide selection of strains and cell media are available via resources such as the Chlamydomonas Resource Center at the University of Minnesota. Our lab acquires cells through the Dutcher lab at Washington University School of Medicine. *C. reinhardtii* cells are grown as previously described.<sup>86</sup> Cells are grown on an agar plate for 48 hours in Sager and Granick rich liquid medium supplemented with sodium acetate at 25 °C in constant light. After incubation, cells on the agar plate can be stored at room temperature for weeks without special care. Before each experiment, cells are suspended in a tube containing a medium lacking nitrogen adapted from medium I of Sager and Granick to promote gametogenesis. To maintain cell viability and avoid clumping, the tube is turned at 10 rpm using a rotator at room temperature. After 3 hours, cells are ready for an experiment.

## 1.4 Specific Aims and Thesis Outline

### 1.4.1 Specific Aims

The overall objective of my doctoral research is to utilize an acoustic microfluidic technique to trap individual *C. reinhardtii* cells and analyze their cilia motion. A new acoustic microfluidic method needed to be developed to trap *C. reinhardtii* (Aim 1), which allows for probing and characterization of cilia dynamics under a static trapping condition (Aim 2) and different stimuli (Aim 3).

The work has three main specific aims:

Aim 1: Develop a new acoustic microfluidic device that can trap single cells.

Aim 2: In a static trap (no introduced flow), probe and characterize the ciliary waveforms of biciliated and uniciliated *C. reinhardtii*.

Aim 3: Probe and characterize the changes in cellular/ciliary motion in response to temperature, varying fluid viscosity, and acoustic induced translational perturbation.

### 1.4.2 Thesis Outline

Chapter 1 covered the background information of microfluidics, acoustofluidics, and *C. reinhardtii*, as well as the motivation and outline of this doctoral work.

Chapter 2 introduces the theory, modeling, and fabrication work of general acoustofluidic devices. Only basic theory, basic modeling, and brief fabrication details related to this project are introduced here. I started as a theoretical modeling researcher in the Meacham lab group, and I pioneered both surface acoustic wave and bulk acoustic wave COMSOL modeling in the lab, including acoustic streaming and particle tracing model. I further investigated acoustofluidic device modeling using weak-form equations (mathematic modeling). But due to the lab direction

and time limitations, my theoretical modeling work has concluded at a stage needed to support my thesis work. Future work will include will include further model investigations including accurate modeling of active swimmers trapped within acoustofluidic devices. I will briefly introduce modeling aspects to assist future researchers with these tasks in the Meacham lab. The fabrication work was tedious and time-consuming; however, I believe it is an essential part of becoming an adept acoustofluidics researcher. My thesis work demonstrates my experience in designing and fabricating almost all kinds of acoustic wave-based devices. I briefly introduce fabrication of SAW devices and other cilia program-related fabrication work. For other fabrication details or questions, I am willing to share additional fabrication details and am happy to answer any questions of the interested reader, as this is part of my lifetime research philosophy.

Chapter 3 details the thermal investigation of PDMS-based and glass-based SAW devices taken from a paper published on Lab on a Chip.<sup>87</sup> Chapter 4 is described trapping of cell populations using the developed acoustic microfluidic method, as well as probing and characterization of cilia waveforms under various conditions, which is the main part of my PhD thesis work. Finally, Chapter 5 is a summary of my thesis work, including current limitations and future directions.

# **Chapter 2: Theory, Modeling, and Fabrication**

The following chapter introduces basic theory of acoustofluidic devices, the basic computational method the author used to predict the device resonant frequency and particle motion, and general fabrication processes for making devices related to this project. Specific channel information, including dimensions, will be introduced in Chapter 3 and Chapter 4.

A brief summary of SAW modeling is also discussed in this chapter. The mesh parameters (mesh dependency study) and other material properties are not discussed as such detailed description of the modeling is beyond the scope of this thesis work. The modeling is used to predict the resonant frequency, and size selectivity of SAW for the author himself.<sup>88, 89</sup>

## **2.1 Theory of Acoustofluidics**

Acoustofluidics describes the incorporation and exploitation of acoustic phenomena in microfluidic systems. The characteristic wavelength of ultrasound in water is of a similar order to the length scales of most microfluidic devices (from 1 to tens to hundreds of  $\mu\text{m}$ ) enabling manipulation of fluids and suspended microparticles in ways that are not possible with other LOC technologies. In this section, two basic theoretical aspects of acoustofluidics, microfluidics and ultrasonics in fluids, are described with emphasis on those most relevant to acoustic separation and enrichment.

### **2.1.1 Basic Rules of Microfluidics**

Microfluidics is a class of fluidic system wherein a fluid is confined in at least one dimension to the microscale domain. Today, microfluidic technologies often comprise essential components of LOC or micro total analysis systems ( $\mu\text{TAS}$ ). These technologies are attractive for several

reasons: low power consumption, inherently laminar flow, short reaction and analysis times, small sample volumes, and potential for low manufacturing cost.

### **Scaling Laws**

Tabeling<sup>90</sup> and Bruus<sup>91</sup> provide detailed discussions of scaling in microfluidic domains. Scaling laws express how physical quantities vary with the size of a given system or subject, while keeping quantities such as time, pressure, temperature, etc. constant. As an example, consider body forces, such as gravity and inertia, and surface forces, such as surface tension and viscous shear. The basic scaling law for the ratio of these two types of forces can be expressed as:

$$\frac{\text{volume forces}}{\text{surface forces}} \propto \frac{l^3}{l^2} = l \xrightarrow{l \rightarrow 0} 0 \quad (2.1)$$

This scaling law implies that as we decrease the length scale  $l$  of a system to the microscale, the ratio of volume forces to surface forces goes to zero. Thus, volume forces, which are important at the macroscale, become largely unimportant at the microscale. Instead, surface forces become dominant. The most essential implication of this law is that viscous effects dominate over inertia in microfluidics, which render the fluid flow laminar.

### **Laminar Flow**

Laminar flow, as opposed to turbulent or chaotic flow, is characterized by fluid flowing without lateral mixing between adjacent laminae and by high momentum diffusion with low momentum advection. The Reynolds number  $Re$ , which predicts whether a flow will be laminar or turbulent, is defined as:

$$Re = \frac{\rho v l}{\eta} \quad (2.2)$$

where  $\rho$  is fluid density,  $v$  is characteristic flow velocity,  $l$  is characteristic length, and  $\eta$  is fluid viscosity. For a typical microfluidic system, the Reynolds number is less than or approximately unity, which often allows for analytical determination of the flow profile and other hydrodynamic parameters of interest.

### **Stokes Drag**

As a particle moves relative to a liquid medium, its motion is opposed by viscous drag. Under laminar flow conditions, in which non-linear terms are expected to be negligible and where there is a no-slip boundary condition on the particle surface, viscous drag  $F_d$  on the particle can be calculated using Stokes drag:

$$F_d = 6\pi\eta av \quad (2.3)$$

where  $\eta$  is fluid viscosity,  $a$  is particle radius, and  $v$  is characteristic flow velocity. Therefore, for purposes of this thesis, drag is proportional to radius. The drag force carries particles along in a fluid flow and will also counteract motion induced by an acoustic field or other external forces.

### **Gravity**

In microfluidic systems, volume (or body) forces, such as gravity, are often neglected; however, when the particles in a medium are denser than the medium, particles can settle to the bottom of a channel given sufficient residence time. Polystyrene beads and glass microspheres under consideration here sink slowly as the particle density is only slightly greater than that of water. Assuming terminal velocity for sedimentation is reached instantaneously, particle settling time is given by:

$$\tau = \frac{9\eta h}{2(\rho_p - \rho)a^2 g} \quad (2.4)$$

where,  $\eta$  is fluid viscosity,  $h$  is the channel height,  $\rho_p$  is the particle density,  $\rho$  is the fluid density, and  $g$  is the gravitational constant. After determining a characteristic settling time, researchers can incorporate a vertical ultrasonic force (or levitation) to offset particle sedimentation. For our purposes (i.e., for the time scales relevant to the current investigations), gravity and particle settling are neglected.

### **2.1.2 Ultrasonics in Fluid**

Sound is the propagation of a deviation from static conditions in a mechanical property of a medium. The property can be velocity or displacement of particles in a medium as a function of time and space, or stress and strain, which in fluids yields the sound pressure field, one of the most essential parameters in acoustofluidics. The pressure field is typically found by solving the wave equation. Due to the characteristic lengths involved, ultrasound is employed in acoustic microfluidics. Operating frequencies exceed 0.5 MHz, which is well above the audible threshold, and most devices operate between 0.5 and 200 MHz. Sound (vibration) behaves differently in fluids than in solids, and as sound propagation in fluids is most relevant to the current work it will be emphasized in the following sections.

#### **Ultrasound in Fluids**

The description of sound in a fluid is mathematically simpler than that of sound in solids, the main reason being that a fluid deforms continuously under shear stress. Normal stress can exist in a great degree, which leads to an expression for pressure. The pressure induced by sound is different from the more familiar hydrostatic fluid pressure. In a microfluidic system, where a fluid is usually treated as incompressible, hydrostatic pressure is assumed constant throughout the system. Thus, the pressure as discussed in this thesis, if not specified, refers to sound pressure. In addition, we also assume that the bulk velocity of the fluid is much smaller than the

speed of sound. The basic acoustic theory presented here is based largely on acoustics texts by Blackstock and Kingsler.<sup>92,93</sup>

We first introduce velocity potential, which relates to the pressure and velocity fields as:

$$t\mathbf{v}(\mathbf{r}, t) = \nabla\varphi(\mathbf{r}, t), \text{ and} \quad (2.5)$$

$$p(\mathbf{r}, t) = -\rho \frac{\partial}{\partial t} \varphi(\mathbf{r}, t) \quad (2.6)$$

where  $\mathbf{v}$  is the velocity of displacement at position  $\mathbf{r}$  and time  $t$ .  $p$  is the sound pressure, and  $\rho$  is the density of the fluid medium. The velocity potential satisfies the wave equation for describing the sound field, so we have:

$$\nabla^2 \varphi = \frac{1}{c^2} \frac{\partial^2 \varphi}{\partial t^2} \quad (2.7)$$

where  $c$  is the speed of sound in the fluid. The speed of sound in the fluid is one of the key parameters in problems of interest and is found from the compressibility  $\kappa$  and density of the fluid  $\rho$ :

$$c = \frac{1}{\sqrt{\kappa\rho}} = \sqrt{\frac{K}{\rho}} \quad (2.8)$$

where  $K$  is the bulk modulus, which is more widely used in solid mechanics and materials science than is compressibility.

In this work, we neglect effects of viscosity of the fluid. In reality, fluid viscosity gives rise to damping of the sound field due to viscous losses in the fluid; however, for aqueous mixtures and ultrasound at MHz frequencies, this effect should be minimal.

## Acoustic Radiation Force

When a particle is immersed in a fluid medium and subjected to a sound field, it will be acted upon by time-averaged (steady-state) forces due to the differences in acoustic properties of a particle and the fluid medium (i.e., acoustic impedance mismatch). Two kinds of radiation force are significant in acoustic microfluidic particle manipulation: the primary radiation force and the secondary radiation force. To simplify this analysis, it is assumed that spherical polymer microbeads or cells with positive acoustic contrast are immersed in water and subjected to an ultrasonic standing wave. The primary radiation force tends to drive the particles towards the zero pressure nodes of the field, and the secondary acoustic radiation force is an attractive interparticle force that tends to agglomerate the particles. We will discuss these two radiation forces separately, based on seminal work reported in the early to mid-20<sup>th</sup> century.<sup>40, 42, 43</sup>

### *Primary Radiation Force*

The most commonly used expression for the forces acting on particles in an arbitrary sound field is given by Gor'kov.<sup>40</sup> For a spherical particle with radius  $a$  in an inviscid fluid (i.e., neglecting viscous effects and heat conduction in the fluid), the primary radiation force is expressed in terms of the gradient of both pressure and velocity fields:

$$F_{rad} = -\frac{4\pi a^3}{3} \left[ f_1 \frac{\kappa}{2} \nabla \langle p^2 \rangle - f_2 \frac{3\rho}{4} \nabla \langle v^2 \rangle \right] \quad (2.9)$$

Parameters  $f_1$  and  $f_2$  are functions of relevant material parameters of the medium and fluid, defined as:

$$f_1 = 1 - \frac{\kappa_p}{\kappa}, \text{ and} \quad (2.10)$$

$$f_2 = \frac{2(\rho_p - \rho)}{2\rho_p + \rho} \quad (2.11)$$

where  $\kappa$  is compressibility, index “p” refers to parameters pertaining to the particle (otherwise pertaining to the fluid). It is important to note that  $f_1$  is determined by the compressibility difference and couples to the pressure gradient, and  $f_2$  is determined by the density difference and couples to the velocity gradient.

As stated earlier, it is the primary acoustic radiation force that drives particles to the nodes or antinodes of the pressure field, but it is the acoustic contrast factor that determines whether particles move to the nodes (minimum pressure) or antinodes (maximum pressure). The acoustic contrast factor  $\Phi$  is calculated as follows:

$$\Phi = \frac{f_1}{3} + \frac{f_2}{2} \quad (2.12)$$

Particles with a positive acoustic contrast factor are driven to nodes when subjected to an ultrasonic standing wave, while particles with a negative acoustic contrast factor are driven to antinodes. Polystyrene beads have a density of  $1060 \text{ kg/m}^3$  and a compressibility of  $2.16 \times 10^{-10} \text{ Pa}^{-1}$ , whereas water, which is representative of the fluids used in the reported work, has a density of  $998 \text{ kg/m}^3$  and a compressibility of  $4.56 \times 10^{-10} \text{ Pa}^{-1}$ ; therefore, the acoustic contrast factor is always positive, which means that the trapping of such particles will occur at nodes (pressure minima) of the pressure fields.

#### *Secondary Radiation Force*

If a large number of particles are present in the fluid, which is often the case particularly as particles focus to a single location, each particle will produce a scattered sound field that can influence other adjacent particles. Interactions between these particles give rise to secondary radiation forces. If the incident field is a plane wave in one dimension, the secondary radiation force between two identical spherical particles can be derived as:

$$F_{sec} = 4\pi a^6 \left[ \frac{(\rho_p - \rho)^2 (3 \cos^2 \theta - 1)}{6\rho d^4} v^2(x) - \frac{\omega^2 \rho (\kappa_p - \kappa)^2}{9d^2} p^2(x) \right] \quad (2.13)$$

where  $\theta$  is the angle between the line connecting the particle centers and the propagation direction of the incident wave,  $d$  is the center-to-center distance between the two particles, and  $\omega$  is the angular frequency. By convention, a positive secondary radiation force means a repulsive force, while a negative secondary radiation force means an attractive force.

The secondary radiation force is strongly dependent on the distance between the particles. The longer the distance between two particles, the smaller the secondary radiation force, which is often neglected for this reason. In this work, we observe clusters of swimming cells near the nodes of the acoustic fields. It is possible that these effects become significant during cell trapping; however, the swimming nature of the cells precludes extremely close contact between cell bodies so this effect is thought to be less important than the primary radiation force.

Equation (2.13) assumes that the incident field is a one-dimensional plane wave, which can be a limitation when applied to complex fields such as those present in our acoustofluidic devices; however, since the force is only significant at very short distances, the plane wave approximation is still likely appropriate for these cases. As the drag, swimming, and primary radiation forces are active at the same time, one must consider these forces and the secondary radiation force together to determine the final positions of the particles (for single cell trapping) or the semi-steady state distributions of populations of cells under the action of an acoustic field, which are of utmost importance when doing particle tracking or analyzing active matter in acoustofluidics.

## **Acoustic Streaming**

Acoustic streaming arises due to viscous losses in a fluid and may take one of three forms:

Schlichting, Rayleigh, or Eckart streaming.<sup>44-46</sup> Schlichting streaming is induced by the viscous boundary layer close to a surface and has vortices much smaller than the acoustic wavelength. Rayleigh streaming stems from boundary layers driving streaming vortices on the scale of a quarter wavelength outside of the boundary layer itself. Eckart streaming typically gives flow in the sound propagation direction. In acoustic microfluidic separations, streaming is usually considered undesirable, as it induces drag on the particles, which tends to adversely affect the static trapping in a microfluidic chip. Thoughtful microchannel design is used to minimize acoustic streaming effects. Under certain operating conditions, we observe weak acoustic streaming phenomena in this thesis work; however, under design conditions, streaming does not significantly affect the acoustic field or the equilibrium positions of trapped cells. Therefore, acoustic streaming is neglected in our post analysis.

## **2.2 Modeling**

Due to the complexity and novelty of the various channel designs presented in this thesis, computational modeling is primarily used as a supplementary method to experiments, guiding an understanding of experimental observations. Here, a 2D PDMS-based SAW is used for prediction of a general SAW system performance regarding its operating frequencies, acoustic pressure field, acoustic streaming field, and associated particle trajectories, which is sufficient to guide further resonant frequency prediction as an extension of this computational modeling method.

The problem has been solved using the finite element software package COMSOL Multiphysics 5.3. A full 2D model including the piezoelectric lithium niobate ( $\text{LiNbO}_3$ )

substrate, PDMS channel, and fluidic domain was built (See Figure 2.1) The module ‘Thermoviscous Acoustics’ in the frequency domain was used to solve for the acoustic pressure numerically. The ‘Laminar Flow’ module was used to model the acoustic streaming numerically. Particle tracing simulations were carried out in the module ‘Particle Tracing for Fluidic Flow’. A mesh-independence test was conducted to ensure the consistency of the modeling. For an accurate modeling consideration, a minimum size of 1  $\mu\text{m}$  for elements near the fluidic boundary was employed. Simulations were used to predict the particle motion in the cross section of a straight PDMS channel under the acoustic radiation force and the Stokes drag induced by acoustic streaming. The secondary acoustic radiation force was neglected to reduce computational cost and complexity.

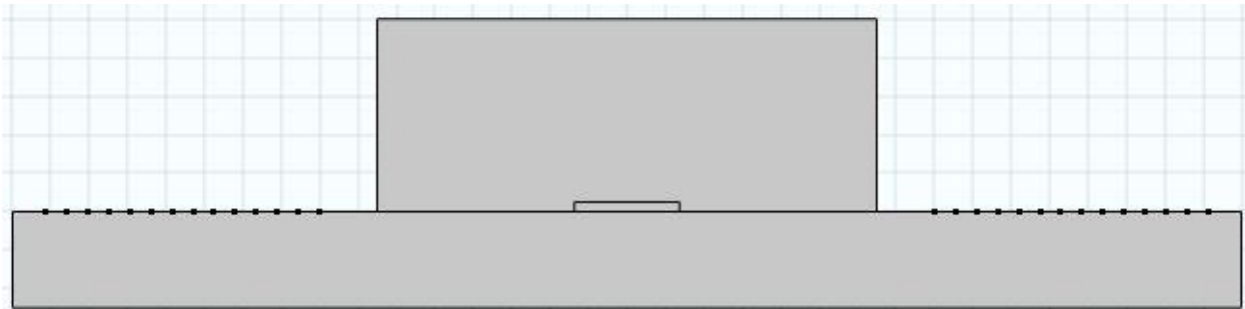


**Figure 2.1.** Geometry of a full 2D cross section finite element model. The substrate is lithium niobate, which is 500  $\mu\text{m}$  thick. The PDMS slab is on top, which is 3 mm wide and 1.5 mm tall. The channel is 545  $\mu\text{m}$  wide and 50  $\mu\text{m}$  tall. To reduce the computational cost, only three pairs of IDTs are modeled.

To predict the particle locations, there are three main steps in COMSOL simulation modeling. First, the acoustic pressure field of SAW was solved at one frequency. After the acoustic pressure field was calculated, the acoustic streaming field was numerically solved by incorporating the first-order acoustic pressure field. Last, the particle locations were determined from the balance of acoustic radiation force and the Stokes drag using a transient model. It is important to note that the fluidic mesh is critical to solution in the transient model. However, use

of a dense mesh is computationally expensive, which takes days to solve and the solution is not always converged.

The cross section of the PDMS superstrate has dimensions of 3 mm x 1.5 mm, and the fluidic chamber is 545  $\mu\text{m}$  wide x 50  $\mu\text{m}$  tall. Only three pairs of IDTs were modeled to reduce the computational cost needed to generate surface acoustic waves. Due to the scope of this thesis, additional details regarding modeling parameters are not included; however, the general approach is detailed elsewhere by other researchers.<sup>94, 95</sup> Here, only the results of simulations involving 10  $\mu\text{m}$  polystyrene beads (Shown in Figure 2.2) and 1  $\mu\text{m}$  polystyrene beads (Shown in Figure 2.3) are shown to illustrate key features of particle focusing within an acoustic field. In these two cases, a transition occurs from acoustic radiation force dominated to Stokes drag force dominated conditions. For the swimming cells, which have a diameter of  $\sim 10 \mu\text{m}$ , these results suggest that streaming should have a minimal effect on the equilibrium position of the cells in an acoustic field.

It can be seen that for the 10  $\mu\text{m}$  PS beads case, the particles are initially evenly distributed inside of the fluidic channel. The PS beads moved to pressure nodes and local pressure minima (left and right corners) due to the combined effects of acoustic radiation force and Stokes drag, where acoustic radiation force was dominant. Conversely, for the 1  $\mu\text{m}$  PS beads case, the PS beads were entrained in the streaming flow at all times due to the dominance of Stokes drag. This model is useful to predict operating frequencies, the acoustic pressure field, acoustic streaming field, and most importantly the particle locations.

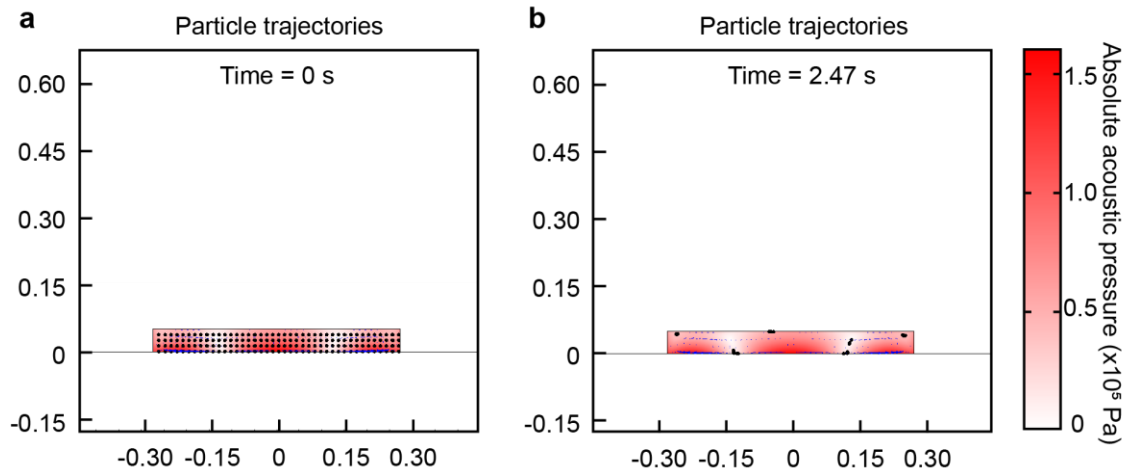


**Figure 2.2.** (a) Illustration of 10  $\mu\text{m}$  PS beads focusing in a 9.6 MHz PDMS-based SAW device. (b) The acoustic radiation force dominated as the 10  $\mu\text{m}$  PS beads moved to pressure nodes or local pressure minima.

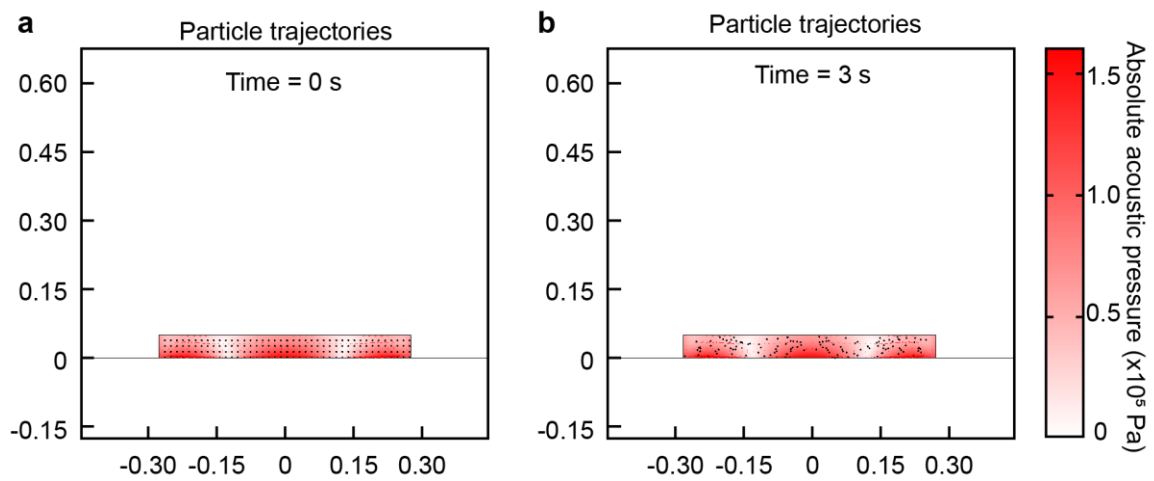


**Figure 2.3.** (a) Illustration of 1  $\mu\text{m}$  PS beads focusing in a 9.6 MHz PDMS-based SAW device. (b) The Stokes drag force dominated as the 1  $\mu\text{m}$  PS beads move with acoustic streaming flow all the time.

## 2.3 Fabrication

An overview of general fabrication processes of this thesis is provided in this section, as illustrated in Figure 2.4 and Figure 2.5. The SSAW devices consisted of a 500- $\mu\text{m}$  thick, 128° Y-cut, x-propagating LiNbO<sub>3</sub> substrate patterned with a pair of interdigital transducers, and a microfluidic channel of PDMS or glass. There are several kinds of designs of IDTs in this work, including straight IDTs, dual-resonant frequency IDTs, and focused IDTs. For the fabrication illustration, only straight IDTs design is listed as an example here.

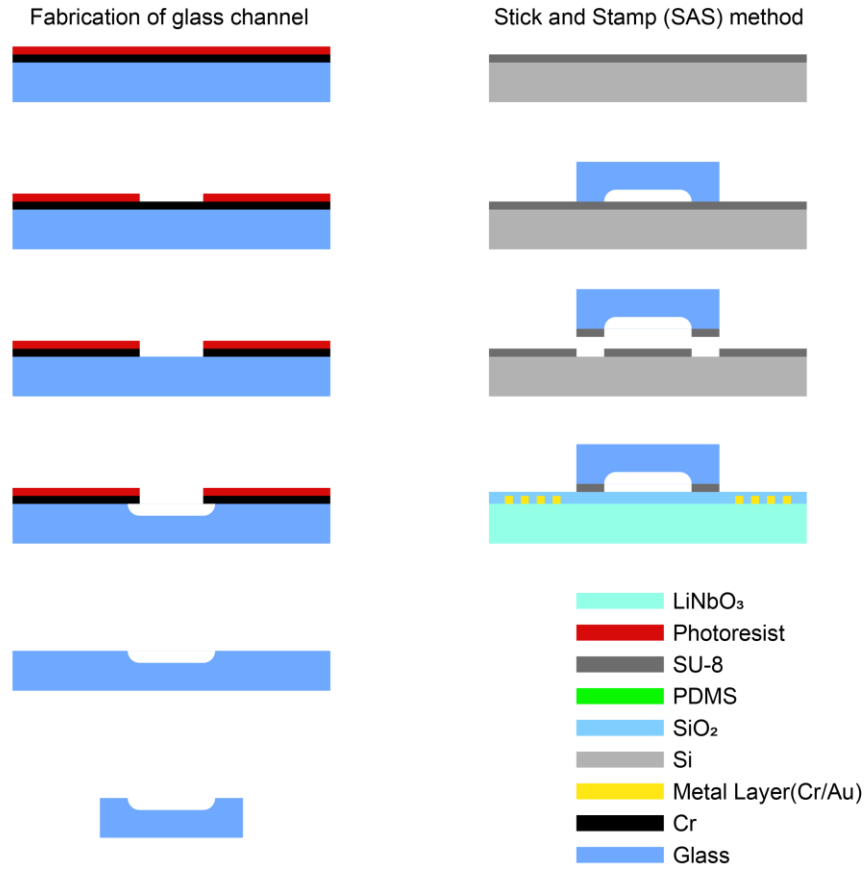


**Figure 2.4.** Illustration of glass channel wet-etching process and ‘stamp and stick’ bonding method using SU-8 as an adhesive layer. Color corresponds to the type of material used.

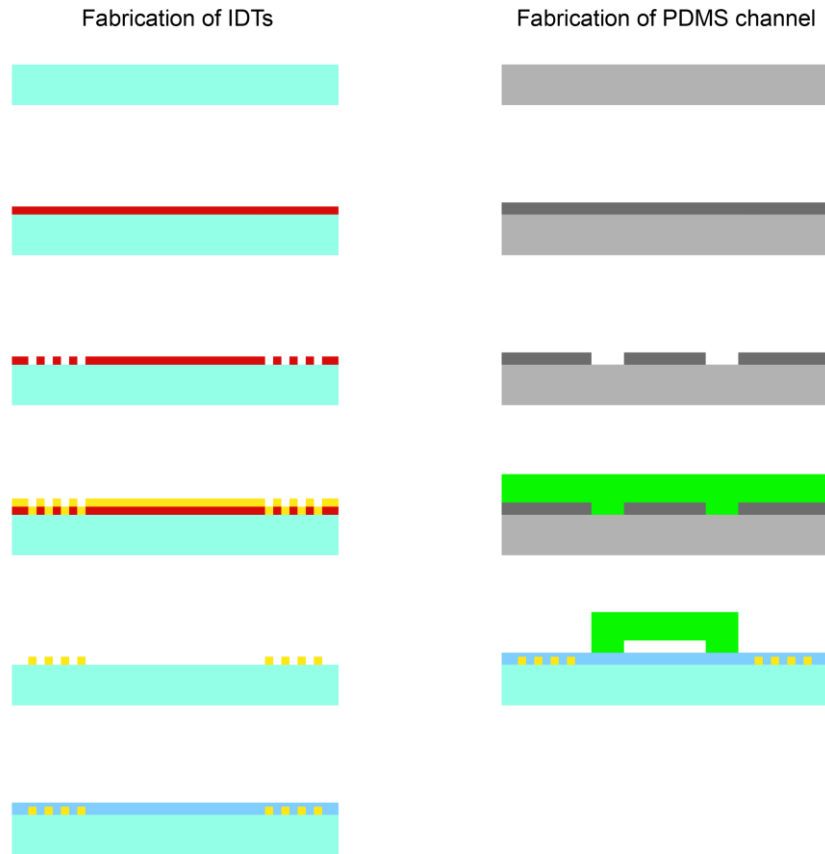


**Figure 2.5.** Illustration of IDTs fabrication process and PDMS channel fabrication process. A thin photoresist was spin-coated on lithium niobate first, followed by metal layer and SiO<sub>2</sub> deposition. The color references to Figure 2.4.

### 2.3.1 Interdigital Transducer Design and Fabrication

A thin layer of photoresist (AZP4620 or S1827) was spin-coated (4000 rpm for AZP4620 or 3000 rpm for S1827) on a clean LiNbO<sub>3</sub> wafer. The photoresist was then pre-baked on a hotplate at 95 °C for 90 seconds to avoid potential thermal stress. The wafer was put into the laser writer (Heidelberg DWL66+) and the primary wafer flat was aligned to the x-axis of the laser writer stage prior to exposure using optimized parameters. After exposure, the wafer was developed in photoresist developer (AZ 400 K for AZP4620, MF319 for S1827). Development time was determined manually to make sure the photoresist was not over-developed. Here, note that the MF319 needs more caution than AZ 400K because it is easier to over develop.

Metal layers (Cr/Au, 10 nm/80 nm) were deposited using a thermal evaporator (306 Vaccum Coater, Edwards), followed by a standard lift-off procedure (sonicating in a glass container with acetone). Depending on the future use of IDTs, the electrodes could be insulated using a 200 nm thick silicon dioxide ( $\text{SiO}_2$ ) layer deposited by physical vapor deposition (PVD, Kurt J. Lesker). The work in Chapter 4 required an insulating layer while the rest of the thesis work did not. The  $\text{LiNbO}_3$  wafer was then cut to size (DAD 323, Disco) using R07 blade at 30,000 RPM, a 2 mm/s feed speed, and a 200  $\mu\text{m}$  cutting depth versus the manufacturer recommendation of a Z09 blade at 35,000 RPM, a 7 mm/s feed speed, and a 300  $\mu\text{m}$  cutting depth due to safety restrictions in place on this equipment.

### **2.3.2 Microfluidic Channel Fabrication**

PDMS microfluidic channels were then fabricated by standard soft-lithography and replica-molding techniques. The author used various SU-8 2000 series photoresists to make different depths of microfluidic channels, from 5 to 200  $\mu\text{m}$  thick. The depth of microfluidic channels of each work will be reported later with the experimental results. First, a 100 mm x 100 mm x 1.5-mm thick chromium-coated photomask blank (Telic Co.) was used to create microfluidic channel patterns in the laser writer using optimized parameters, followed by development using AZ 400 K. The chromium was etched away using chromium etchant. Again, observation of feature resolution was used to control the development process. Then a desired thickness layer of SU-8 2000 series (MicroChem) was spin-coated on a single side polished silicon wafer, followed by a standard pre-bake process. The microfluidic channel pattern was transferred via a conventional UV contact printer/mask aligner (KLOE UV-KUB3 or Karl Suss MJB3). An increase in exposure time approximately 30-40% was required to reach the necessary exposure dose. A hard bake was needed to anneal surface cracks in SU-8 molds, which yielded

better quality PDMS channels. The mold was treated with silane vapor (1H, 1H, 2H, 2H-perfluorooctyl-trichlorosilane, Sigma-Aldrich, USA) under vacuum overnight to aid in channel release. PDMS replicas (Sylgard 184, 10:1 base:cross linker, Dow) were cured at room temperature on a leveled air table for 48 hours for most cases, or alternatively in an oven at 65 °C. Cured PDMS channels were cut to final dimensions, and 1 mm diameter inlet and outlet holes were added using a biopsy punch.

The glass channels for cell population trapping devices were created via isotropic wet etching of 100 mm x 100 mm x 1.5-mm chromium-based photomask blanks (Telic Co.). The blanks comprised a 110 nm-thick layer of vacuum deposited chromium and a 530 nm layer of positive photoresist. First, the microfluidic channel pattern was made via a similar procedure as previously described. Then the exposed mask blank was etched in a concentrated mixture of glass etchant [2:1:6 (volume), hydrofluoric acid (HF, aq. 48%) : nitric acid (a1., 69%): deionized (DI) water] till the final desired channel height was reached. Inlet and outlet holes were manually drilled into the channels, and the blank was diced to desired dimensions.

The fabrication process of thin layer glass channels for single cell trapping is more complex than that used for the thick glass devices for trapping populations of cells. First, thick metal layers (Cr/Au, 20 nm/400 nm) were deposited on both sides of 40 mm x 20 mm x 0.17 mm coverslips (VWR Micro Cover Glasses) using a thermal evaporator (306 Vacuum Coater, Edwards) to avoid uneven surfaces after the subsequent wet etching processes (of gold, chromium, and glass). Then a thick layer of AZP4620 (at 2000 rpm) was spin-coated on the backside (either side) of coverslips and post-baked at 120 °C for 30 minutes. The front side of the coverslip needed to be spin-coated with desired photoresist, which should be thick enough for

protection but thin enough for sufficient accuracy. A coverslip was moved to the mask aligner and patterned using a prepared photomask. After developing in photoresist developer, the coverslip was etched to a desired depth using gold etchant, chromium etchant, and mixed HF solution described in the last paragraph. Special care needed to be taken to avoid breaking or cracking the thin coverslip. The remaining metal layers were removed in gold etchant and chromium etchant at last, before cutting into pieces using the dicing saw.

# **Chapter 3: Thermal Considerations for Surface Acoustic Wave (SAW) Devices**

This chapter is a reproduction of the paper ‘Thermal considerations for microswimmer trap-and-release using standing surface acoustic waves’, published in Lab on a Chip in 2021.<sup>87</sup>

Controlled trapping of cells and microorganisms using substrate acoustic waves (SAWs; conventionally termed surface acoustic waves) has proven useful in numerous biological and biomedical applications owing to the label- and contact-free nature of acoustic confinement. However, excessive heating due to vibration damping and other system losses potentially compromises the biocompatibility of the SAW technique. Herein, we investigate the thermal biocompatibility of polydimethylsiloxane (PDMS)-based SAW and glass-based SAW [that supports a bulk acoustic wave (BAW) in the fluid domain] devices operating at different frequencies and applied voltages. First, we use infrared thermography to produce heat maps of regions of interest (ROI) within the aperture of the SAW transducers for PDMS- and glass-based devices. Motile *Chlamydomonas reinhardtii* algae cells are then used to test the trapping performance and biocompatibility of these devices. At low input power, the PDMS-based SAW system cannot generate a large enough acoustic trapping force to hold swimming *C. reinhardtii* cells. At high input power, the temperature of this device rises rapidly, damaging (and possibly killing) the cells. The glass-based BAW/SAW hybrid system, on the other hand, can not only trap swimming *C. reinhardtii* at low input power, but also exhibits better thermal biocompatibility than the PDMS-based SAW system at high input power. Thus, a glass-based BAW/SAW device creates strong acoustic trapping forces in a biocompatible environment,

providing a new solution to safely trap active microswimmers for research involving motile cells and microorganisms.

### 3.1 Introduction

Microfluidic separation, sorting, and trapping are prevalent in the fields of genetic analysis, molecular and cellular biology, biotechnology, and pharmaceuticals.<sup>4, 5, 96-98</sup> Methods that exploit microfluidics provide improved performance while reducing cost through increased flexibility, decreased sample volume and operating time, and opportunities for process automation.

Technologies are classified based on their underlying physics, and optical,<sup>16, 17</sup> hydrodynamic,<sup>6, 8, 9, 22</sup> dielectrophoretic,<sup>10-12, 99</sup> magnetic,<sup>13-15, 30</sup> and acoustic<sup>18, 20, 100</sup> manipulation of cells and particles are well-established. Among these approaches, acoustic microfluidics permits label-free cell manipulation without direct contact, which minimizes undesirable surface interactions and limits physical stress on sensitive biological samples. These attributes have driven the adoption of acoustofluidic devices as research tools for single-cell and multi-cell population-based analyses.<sup>61, 101-103</sup>

In conventional acoustophoresis, a standing wave is generated inside a microfluidic channel, and the acoustic radiation force arises due to scattering of the acoustic wave on suspended particles. Neglecting interparticle and particle-wall interactions, particle motion is dictated by the balance of fluidic drag and the acoustic radiation force, which is a function of particle size and the acoustophysical properties of the particle (i.e., particle density and compressibility relative to the suspension medium).<sup>40-43</sup> Commonly, a standing bulk acoustic wave (BAW) forms when a piezoelectric element actuates a rigid microfluidic channel (e.g., silicon/glass) at one of its resonant frequencies.<sup>89, 104, 105</sup> Alternatively, interdigital transducers (IDTs) can be used to generate a substrate acoustic wave (SAW) on a piezoelectric element, with

the wave leaking into the fluid at the location of the microchannel.<sup>106-108</sup> Here, we apply the conventional abbreviation SAW to include any substrate waves excited using IDTs, e.g., Rayleigh surface acoustic waves, as well as Lamb waves that arise due to the use of thin piezoelectric substrates. Typical 500- $\mu\text{m}$  thick lithium niobate ( $\text{LiNbO}_3$ ) substrates limit production of true Rayleigh SAW to frequencies above 40 MHz, though many researchers label such devices as SAW (meaning Rayleigh SAW) when operating in the 10-30 MHz range.<sup>56</sup> In the present work, cell trapping resulting from Lamb wave actuation should be indistinguishable from that due to Rayleigh SAW; however, Lamb wave reflection from the backside of the substrate represents an additional energy loss mechanism.

Both BAW and SAW are widely employed for particle and cell manipulation, and in most cases, the particles and cells are inactive (i.e., non-swimming).<sup>57, 104, 108</sup> Demonstrations include separation of circulating tumor cells (CTCs) from white blood cells (WBCs),<sup>61</sup> single cell per well patterning of individual human lymphocytes and red blood cells,<sup>62</sup> platelet enrichment from whole blood,<sup>63</sup> removal of adherent cells from culture plates,<sup>109</sup> assembly of cell aggregates for drug screening and tissue engineering applications,<sup>110, 111</sup> manipulation of nanomaterials on microparticle reaction substrates,<sup>59, 60</sup> and even atomization of biomolecule and cell suspensions.<sup>112-114</sup>

Fewer studies report acoustic trapping and analysis of active matter, like swimming cells. Particles with their own intrinsic motors generate an additional propulsive force that the acoustic radiation force must overcome to hold the particle (cell or organism) in place. Further, the motility of microswimmers can also affect the rheological properties of the suspension medium, evidencing the complex interplay of fluidic and particle behaviors in such systems.<sup>115</sup> Although sample safety and biocompatibility are commonly listed as advantages of acoustofluidic

manipulation, the higher input power needed to achieve sufficient trapping forces may lead to device heating that can affect biological samples. Nonetheless, thermal analyses are often incomplete or absent. Ding et al.<sup>19</sup> used a dynamic SAW field for precise positioning of a swimming *Caenorhabditis elegans*, which is known to respond to thermal stimuli (e.g., entering a state of protective paralysis at elevated temperatures);<sup>116</sup> however, the reported input power (~0.8 W) needed for the operation exceeded the range over which the operating temperature was evaluated (~0.2 W, ~26°C at 1 min; ~0.32 W, ~30°C at 1 min), so it is unclear if device heating played a role in this result. Miansari et al.<sup>117</sup> extensively characterized use of SAW irradiation to induce traumatic brain injury in *C. elegans*, carefully designing experiments to avoid paralysis observed for high input power SAW excitation of sessile droplets containing the worms. Exposure time was also kept short to reduce the risk of heating effects. Takatori et al.<sup>118</sup> used a focused ultrasound transducer to study the swimming pressure of acoustically confined populations of active Janus particles. In these so-called single-beam acoustic tweezers, device heating can be a concern, particularly for integration with microfluidics where a high-intensity beam is required to penetrate the channel material;<sup>119, 120</sup> however, thermal effects are rarely considered.<sup>121</sup> BAW devices have long been used for manipulation and patterning of passive particles and cells.<sup>57, 122, 123</sup> More recently, Kim et al.<sup>64, 124</sup> applied a BAW-based acoustic trap-and-release method to quantify the swimming capability of motile *Chlamydomonas reinhardtii* and its mutants. Repeat experiments were used to assess the effects of ultrasound exposure with cells confined as loose agglomerates for up to 75 s; however, thermal effects were avoided by conducting experiments on a temperature-controlled stage.

The temperature within an acoustofluidic system is elevated due to induced vibrations and the low thermal conductivity of the channel/substrate materials, among other effects. The

thermal behavior of BAW devices has been studied extensively, leading researchers to implement a number of temperature control strategies;<sup>102, 104, 122, 123, 125-129</sup> however, the thermal response of SAW devices is less well studied. Kondoh et al.<sup>130</sup> analyzed the temperature variation of droplets in an open SAW system while adjusting the input power and fluid viscosity. The temperature increase during a fixed time period was found to be proportional to the applied power, and also varied with viscosity. Zheng et al.<sup>131</sup> studied the heating mechanism of standing surface acoustic waves (SSAWs) for sessile droplets on a LiNbO<sub>3</sub> substrate, implicating a combination of acoustothermal effects introduced by SSAWs and Joule heating due to the alternating current field. In practice, cell manipulations are more commonly accomplished in closed polydimethylsiloxane (PDMS) channels. In addition to the role of the electric field in device heating, the temperature in such channels increases rapidly due to the high vibration damping ratio and low thermal conductivity of PDMS. Shi et al.<sup>108</sup> used an infrared (IR) thermometer to estimate the temperature in a closed PDMS channel for patterning cells at relatively low input power. Although device heating due to PDMS channels is typically detrimental (indeed researchers have explored alternative channel materials for this reason),<sup>132</sup> controlled heating can be beneficial for certain applications. Ha et al.<sup>133</sup> exploited the rapid temperature rise in higher-power SAW-driven PDMS microfluidic channels to regulate the temperature during a two-step continuous flow polymerase chain reaction (CFPCR) for DNA amplification. Their results provide the most complete description of acoustothermal effects in PDMS microchannels to date; however, rigorous thermal analysis of closed channel SAW systems suitable for trapping biological active matter remains to be done.

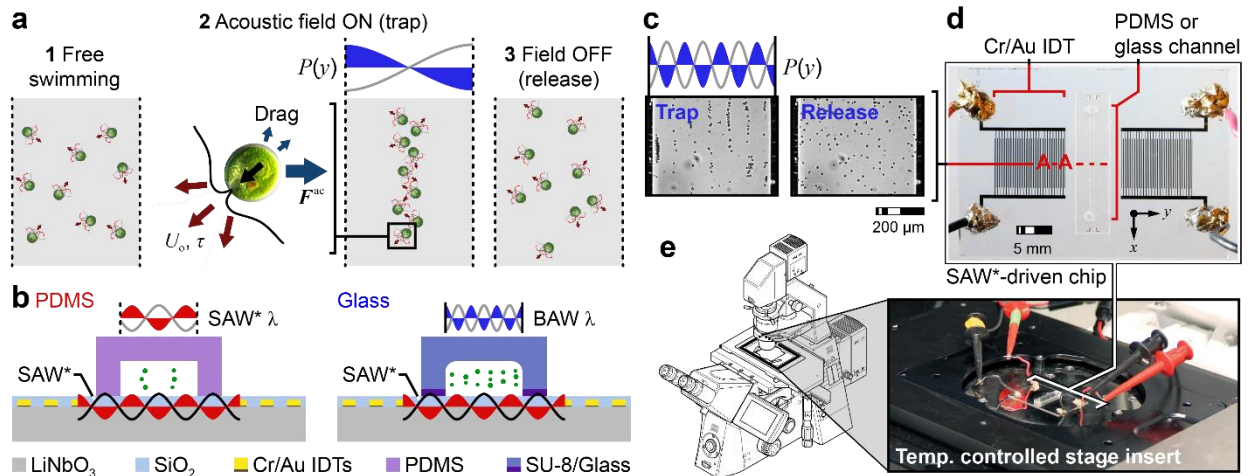


**Figure 3.1.** Trap-and-release illustration and mechanisms of PDMS-based and glass-based SAW device operation.

(a) A standing acoustic field first traps (acoustic field on) and then releases (field off) *C. reinhardtii* cells. When trapped, the acoustic radiation force  $F^{ac}$  balances the swimming capability of the cells (characterized by a swimming velocity  $U_o$  and reorientation time  $\tau$ ). (b) PDMS-based SAW device mechanism: standing substrate acoustic waves (SSAWs) leak into the fluid channel and generate standing waves; glass-based SAW device mechanism: SSAWs leak into the fluid chamber and generate standing bulk acoustic waves (SBAWs). (c) Acoustic trap-and-release experiment in a glass-based SAW device. (d) Top-view of a glass-based SAW device. (e) Device mounted on a temperature-controlled stage insert. Note that temperature control is not used during the current trap-and-release experiments to assess the effect of temperature rise on cell viability.

Here, we first use an infrared (IR) camera to map the temperature of SAW devices incorporating either PDMS (PDMS-based SAW) or glass (glass-based SAW) microchannels. We then introduce *C. reinhardtii* cells into the channels to perform trap-and-release experiments and to assess the biocompatibility of the devices operating at different frequencies and input powers (see Figure 3.1). We found it impossible to trap swimming *C. reinhardtii* cells in a PDMS microchannel without a loss of function or possibly cell death. The input power required to effectively trap the cells led to acoustothermal heating at the channel location to above the thermotolerance threshold of the *C. reinhardtii* cells (i.e., the temperature above which *C.*

*reinhardtii* cells experience heat shock that triggers a metabolic response characterized by motility loss or cell death;  $\sim 37^\circ\text{C}$ ).<sup>134, 135</sup> Conversely, a glass-based SAW device generated sufficient trapping force without fatal heating for a time duration relevant to single-cell and population-based analyses. Thus, these results show that glass-based SAW devices can generate the high acoustic radiation force needed to manipulate swimming cells while maintaining a biocompatible environment. Although this finding is most relevant to applications involving acoustic confinement of active matter, our study highlights the importance of thermal characterization in biological applications of acoustofluidic devices.

## 3.2 Methods

### 3.2.1 Device Fabrication

The general fabrication method followed the procedure described in previous chapter, and previous publications. The SSAW devices consisted of a 500- $\mu\text{m}$  thick,  $128^\circ$  Y-cut, X-propagating  $\text{LiNbO}_3$  substrate patterned with a pair of IDTs, and a microfluidic channel of PDMS or glass (Fig. 1). The IDTs were oriented perpendicular to the  $x$ -axis of the  $\text{LiNbO}_3$ . Metal layers (Cr/Au, 10 nm/80 nm) were deposited using thermal evaporation (306 Vacuum Coater, Edwards) followed by a standard lift-off process. All IDTs had 25 pairs of straight electrodes. Different devices were designed for operation at  $\sim 10$  MHz (400  $\mu\text{m}$  wavelength) and  $\sim 24$  MHz (160  $\mu\text{m}$ ). Although the relatively thin electrodes raised concerns regarding ohmic heating at the IDTs, the impedance was consistently measured to be  $\sim 60 \Omega$  and  $\sim 76 \Omega$  for  $\sim 10$  MHz and  $\sim 24$  MHz devices, respectively, over the entire range of drive voltage (5–25  $V_{\text{pp}}$  corresponding to input power of  $\sim 0.05$ –1.2 W with slightly lower power for the higher frequency devices, see Experimental Setup). Thus, the impedance was below 100  $\Omega$  at each resonance, limiting heating at the IDTs. The aperture of the IDTs was 7 mm, and the distance between

opposing IDTs was 7.9 mm. Electrodes were insulated using a 220 nm thick silicon dioxide ( $\text{SiO}_2$ ) layer deposited by physical vapor deposition (PVD 75, Kurt J. Lesker). The  $\text{LiNbO}_3$  wafer was cut to size (DAD 323, Disco).

PDMS and glass channels were 15 mm long, 545  $\mu\text{m}$  wide, and 50  $\mu\text{m}$  high. For consistency, all glass and PDMS channel superstrates were 20 mm long, 5 mm wide, and 1.5 mm high.<sup>136</sup> PDMS superstrates were fabricated by standard SU-8 photolithography and replica molding. A 50  $\mu\text{m}$  thick layer of SU-8 2050 photoresist (MicroChem) was patterned using vendor-recommended parameters, and the resulting mold was treated with silane vapor (1H, 1H, 2H, 2H-perfluorooctyl-trichlorosilane, Sigma-Aldrich, USA) under vacuum for 2 hrs to aid in channel release. PDMS replicas (Sylgard 184, 10:1 base:cross linker, Dow) were cured at room temperature on a leveled air table for 48 hours. Cured PDMS channels were cut to final dimensions, and 1 mm diameter inlet and outlet holes were added using a biopsy punch. The glass channels were wet etched into a 1.5 mm thick soda lime glass blank, as described previously.<sup>137</sup> Inlet and outlet holes (1 mm diameter) were manually drilled into the channels, and the blank was diced into 20 mm  $\times$  5 mm pieces (DAD 323, Disco).

The PDMS channels and  $\text{LiNbO}_3$  were treated with oxygen plasma before bonding. 10  $\mu\text{L}$  of 70% ethanol was dropped onto the  $\text{LiNbO}_3$  surface to serve as a lubricant during alignment of markers on the channel superstrate and  $\text{LiNbO}_3$ . After alignment, the ethanol was removed under vacuum, and the assembly was baked in an oven at 65°C overnight. The glass channels were bonded to the  $\text{LiNbO}_3$  substrate by SU-8 2005 (MicroChem) using a stamp-and-stick (SAS) method.<sup>138</sup> Special care was taken to avoid air bubble formation and SU-8 leakage into the channel.

For select samples, an 8  $\mu\text{m}$  thick black paint (Black enamel 1149TT, Testor's) layer was spin-coated onto the  $\text{LiNbO}_3$  to facilitate accurate temperature measurement using an IR camera. For thermal characterization, the SAS method was again used to bond both PDMS and glass channels to the  $\text{LiNbO}_3$  via liquid PDMS and SU-8 2005, respectively.

### 3.2.2 Cell Culture and Preparation

Wild-type (CC-125) *Chlamydomonas reinhardtii* cells were obtained from the Dutcher Lab at Washington University in St. Louis. Cells were cultured on agar plates under constant room lighting at 25°C, following a previously-reported protocol.<sup>86</sup> Three hours prior to an experiment, cells were resuspended in a test tube containing a medium that lacked nitrogen (adapted from Medium I of Sager and Granick<sup>139</sup>) to promote gametogenesis. To maintain cell viability during resuspension, tubes were turned at 10 rpm using a rotator (Rotator Genie SI-2110, Scientific Industries). The tubes were vortexed to obtain a uniform suspension of cells. Typical cell concentrations were  $5\text{--}6 \times 10^6$  cells per mL for trap-and-release experiments. Note that *C. reinhardtii* prefer environments between 20 and 32°C; cell function and/or viability are compromised at temperatures exceeding 37–43°C, depending on cell growth conditions.<sup>134, 140, 141</sup>

### 3.2.3 Experimental Setup

A function generator (33522A, Agilent) and amplifiers (240L for ~10 MHz actuation, ENI; 125A250 for ~24 MHz actuation, Amplifier Research) were used to drive the SAW devices. A PC oscilloscope (PicoScope 5444D, Pico Technology) was used to determine the impedance response by measuring the applied voltage waveform (using a voltage probe at the piezoelectric element), the current waveform (voltage probe across a ground-side current sensing resistor), and phase (relationship between the two waveforms) over the relevant frequency range of interest. The nominal operating frequency was determined from the reflection coefficient.<sup>142, 143</sup> C.

*reinhardtii* cells were then loaded into PDMS or glass channels, and the frequency corresponding to maximum nodal confinement of the cells was identified as the optimal resonant frequency (9.62 MHz for the ~10 MHz device and 24.05 MHz for the ~24 MHz device). The input voltage range for the study was  $V = 5\text{--}25 V_{pp}$ , in increments of  $5 V_{pp}$  (corresponding to input powers of 0.05–1.2 W and 0.04–1.1 W for the ~10 MHz and ~24 MHz devices, respectively). Each experiment was repeated three times.

### **3.2.4 Video Microscopy**

The trap-and-release of *C. reinhardtii* cells was visualized on the stage of an inverted microscope (Axio Observer z.1, Zeiss) using a 10× objective (EC Plan-Neofluar 10×/0.30 M27, Zeiss) (Fig. 3.1e). Videos were recorded at 38 frames per second (fps) at  $1932 \times 1460$ -pixel resolution ( $0.454 \mu\text{m} \times 0.454 \mu\text{m}$  per pixel), using a 3-Megapixel camera and imaging software (AxioCam 503; ZEN software, Zeiss). To reduce the adhesion of cells to the channel walls, microfluidic channels were pretreated with 0.5% (w/v) bovine serum albumin (BSA) (Sigma-Aldrich) in phosphate-buffered saline (PBS) for 15 min. The microfluidic channels were flushed with DI water after each experiment to ensure that no cells remained to contaminate subsequent experiments. In addition, the time interval between each experiment was at least ten minutes, long enough to ensure that the microfluidic channels fully cooled to room temperature. A custom Python program was used to precisely control experimental inputs.

### **3.2.5 Infrared Imaging and Analysis**

Thermal characterization experiments were performed using a custom infrared (IR) thermography setup. Devices were mounted in a laser-cut acrylic holder above a gold mirror that directed light to an IR camera (3–5.4  $\mu\text{m}$ ; Fast M3K, TEL-5358, Telops) with a 1× objective (TEL-5329, Telops) (Figure 3.2). The black paint increased the emissivity of the substrate-

channel interface to greater than 0.98 to improve temperature measurement accuracy at the location of interest.<sup>144-148</sup> Videos were recorded at 20 fps and  $320 \times 256$ -pixel resolution ( $30 \mu\text{m} \times 30 \mu\text{m}$  per pixel), using the IR camera and Reveal IR imaging software (Telops). The IR camera measurement was calibrated using a resistance temperature detector (PT 100, Omega) to account for the deviation from black body emission of the black paint and transmission losses in the  $\text{LiNbO}_3$  substrate.<sup>147, 148</sup> The recorded videos and associated data were post-processed in MATLAB using the calibration. Room temperature remained at  $23^\circ\text{C}$  throughout. Note that the device temperatures were measured at the substrate-channel and substrate-PDMS/glass interfaces.

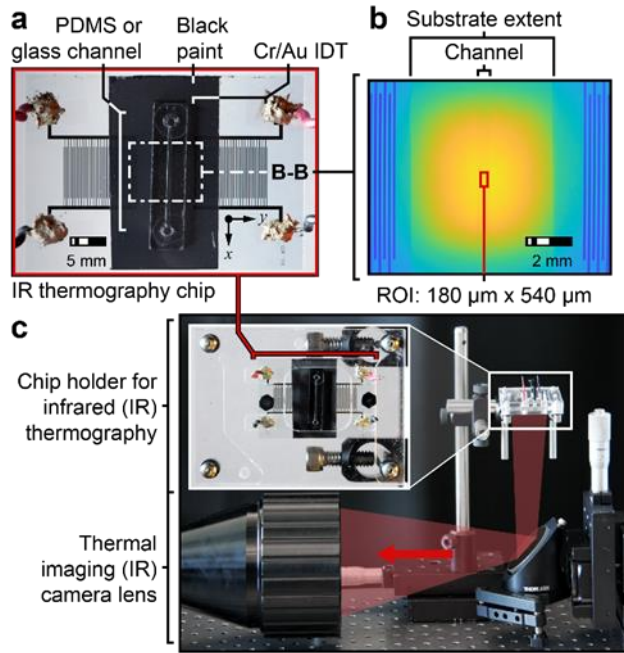


**Figure 3.2.** Infrared (IR) thermography experimental setup. (a) Top view of a glass-based SAW device with black paint (BP). (b) A bottom-view IR image of a PDMS-based channel during actuation. The region of interest (ROI) inside the channel is  $180 \mu\text{m} \times 540 \mu\text{m}$ . (c) The custom assembly used for temperature measurements.

The thermal responses of devices with and without black paint were compared to determine whether black paint (BP) was needed to obtain accurate measurements. Channels were

loaded with cell medium and the average temperature of the region of interest ( $180\ \mu\text{m} \times 540\ \mu\text{m}$  rectangular area in the channel near the middle of the IDT aperture, labeled  $T_{\text{ROI}}$  in Figure 3.2 b) was monitored over a 120 s heating/recovery cycle (30 s actuation at  $25\ \text{V}_{\text{pp}}$ , 90 s recovery).

Trend lines (exponential rise/decay) were fitted to three repeats of each experimental condition (PDMS, no BP; PDMS, BP; glass, no BP; glass, BP). Thermal response plots include exponential rise/decay fits with 95% confidence bands. PDMS-based SAW devices without black paint had similar responses as those with paint showing a maximum temperature difference of  $2\text{--}3^\circ\text{C}$  for the  $\sim 24\ \text{MHz}$  device (Figure 3.3 a). In contrast, the temperature of the glass-based SAW devices without black paint was much higher than for those with paint (Figure 3.3 b). For the  $\sim 10\ \text{MHz}$  device, the maximum measured temperature was  $20^\circ\text{C}$  lower for the device with black paint, while the difference in measured temperature was  $7^\circ\text{C}$  for the  $\sim 24\ \text{MHz}$  device. These results confirmed that black paint was needed for the reported experiments as PDMS is nearly opaque to IR radiation, while glass is not (note that  $\text{LiNbO}_3$  is largely transparent in the near- and mid-IR range up to a wavelength of  $\sim 5\ \mu\text{m}$ ).

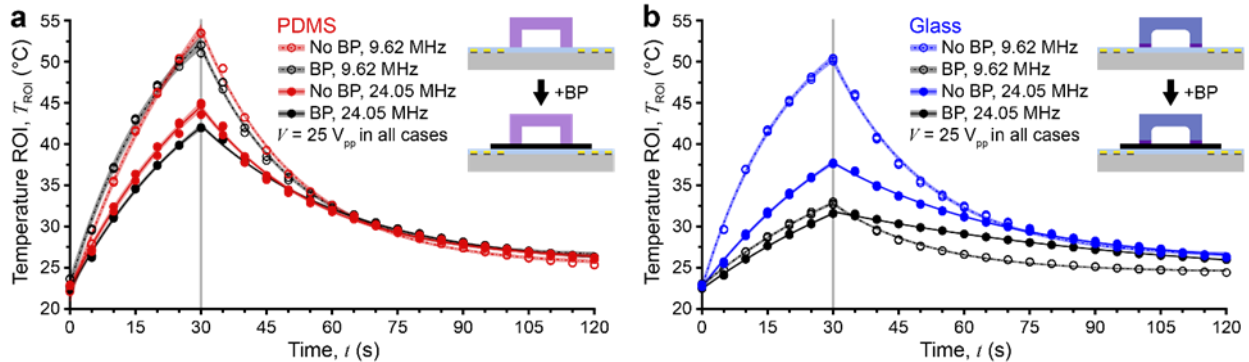


**Figure 3.3.** Comparison of the thermal response within the ROI for uncoated devices and devices with BP when the channel is loaded with cell medium. (a) PDMS-based SAW device comparison. (b) Glass-based SAW device comparison. Experimental duration is 120 s, 30 s with the signal on and 90 s off.

### 3.4 Results and Discussion

Heating of acoustofluidic devices presents problems in biological and biomedical applications. Although thermal analyses have been conducted on open SAW systems (e.g., for droplets on the surface of SAW devices),<sup>130, 131</sup> few studies have examined heating in closed-channel systems due to the difficulty of obtaining in-channel temperature measurements. Use of temperature-dependent fluorescent dyes is well-established in microfluidics, but this approach yields only the temperature of the fluid domain.<sup>149</sup> Applicability is also dependent upon dye-channel compatibility and sophisticated acquisition equipment.<sup>150</sup> Researchers have also incorporated surface micromachined resistance temperature detectors (RTDs) for in situ measurements; however, each RTD is only a single point measurement probe so circuit layouts can be complex if many RTDs are needed.<sup>151</sup> Thermoresistive elements have been glued to the piezoelectric transducer of BAW devices to monitor global temperature transients, but again, this method provides the temperature at a single location relatively far from the microfluidic channel.<sup>104</sup>

In the present study, we first used IR thermography to generate heat maps of PDMS- and glass-based SAW devices driven for 30 s at voltages from 5 to 25 V<sub>pp</sub> in 5 V<sub>pp</sub> increments. Measurements continued for 90 s during recovery to room temperature for a total experimental time of 120 s (30 s on, 90 s off). IR thermography was selected to provide temperature information from both the microchannel and the interface between the LiNbO<sub>3</sub> substrate and channel superstrate adjacent to the microchannel. After completing the abiotic thermal characterization of both channel materials, we correlated the temperature information to the observed behaviors of swimming *C. reinhardtii* cells under the same conditions. Experiments were duplicated for ~10 MHz and ~24 MHz devices.

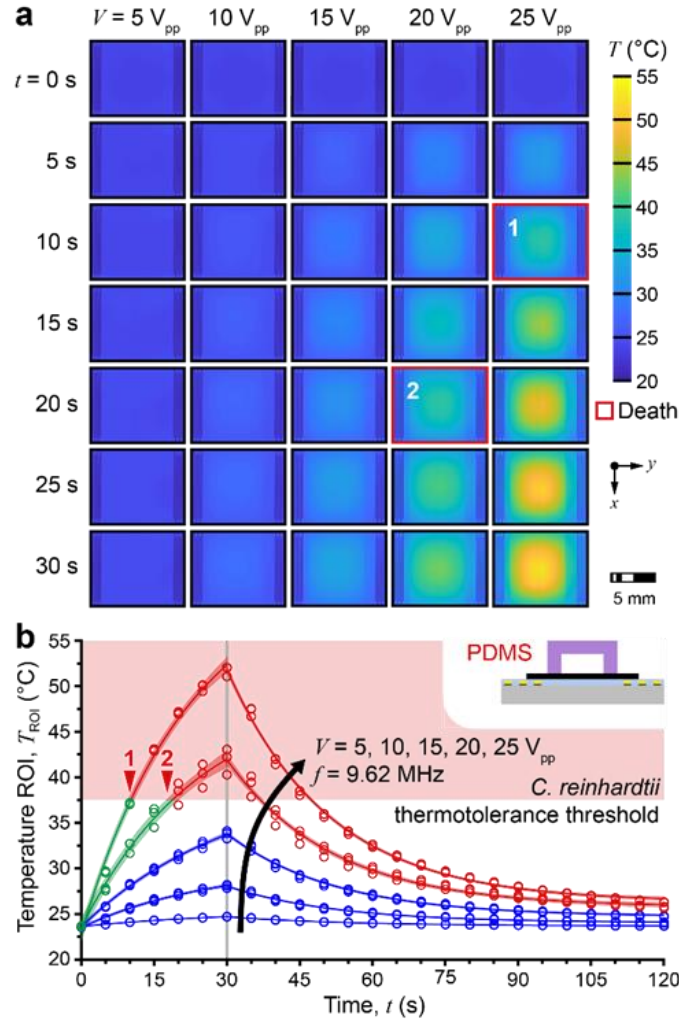
### 3.3.1 Thermal Response of 10 MHz Devices

Figure 3.4 details the thermal response of a PDMS-based device operated at  $f = 9.62$  MHz. In the signal-on period, the system temperature increased gradually over time for all drive voltages with significant heating ( $>10^\circ\text{C}$  increase in  $T_{\text{ROI}}$  at 30 s) observed for  $V = 20$  V<sub>pp</sub> and 25 V<sub>pp</sub>. At 5 V<sub>pp</sub> and 10 V<sub>pp</sub>, the  $T_{\text{ROI}}$  changed less than  $5^\circ\text{C}$ . An input voltage of 15 V<sub>pp</sub> appears to represent the maximum allowable voltage for biocompatibility with *C. reinhardtii* as  $T_{\text{ROI}}$  reached  $33^\circ\text{C}$  at 30 s, just under the thermotolerance threshold of the cells (Figure 3.4 b). At 20 V<sub>pp</sub> and 25 V<sub>pp</sub>, the  $T_{\text{ROI}}$  exceeded  $37^\circ\text{C}$  at 20 s and 10 s, respectively, with a maximum  $T_{\text{ROI}}$  of  $53^\circ\text{C}$  achieved at the end of the 25 V<sub>pp</sub> actuation period.

Heat maps also indicate that the ‘hot spot’ extends along most of the microchannel length within the aperture of the IDTs, and well into the PDMS superstrate bounding the channel in this region. Here, the interface between the LiNbO<sub>3</sub> substrate and PDMS channel heats quickly. The PDMS superstrate outside the aperture is cooler due to a lower amplitude of the SSAW outside the aperture and potentially because heat conduction within the PDMS is poor. In addition, the LiNbO<sub>3</sub> outside of the PDMS superstrate remains relatively cool regardless the applied voltage, as there is little attenuation of the travelling SAW before it reaches the PDMS layer.

The glass-based device and a SAW device without a bonded channel were also tested at the same frequencies and applied voltages as the PDMS-based device. The rise and fall of  $T_{\text{ROI}}$  for the three different devices driven at 25 V<sub>pp</sub> are shown in Figure 3.5 a. The  $T_{\text{ROI}}$  of the glass-based SAW device stays below the thermotolerance threshold of the *C. reinhardtii* cells, and the  $T_{\text{ROI}}$  of the no-channel SAW device barely increases. The glass channel superstrate is less attenuating than the PDMS. In addition, PDMS has a significantly lower thermal conductivity

than glass (0.15 W/m-K vs. 1.3–1.5 W/m-K). Thus, heat generated at the interface of the LiNbO<sub>3</sub> and channel superstrate was dissipated more easily in glass than in PDMS-based devices.



**Figure 3.4.** Heat maps of a 10 MHz PDMS-based SAW device (experimental actuation frequency  $f = 9.62 \text{ MHz}$ ).

(a) The thermal response of the region between the IDTs for different drive voltages ( $V = 5\text{--}25 \text{ V}_{pp}$ ). Cases highlighted in red indicate possible cell death due to heat stress. (b) Progression of the ROI temperature  $T_{ROI}$  for different drive voltages. The *C. reinhardtii* thermotolerance threshold ( $T \approx 37 \text{ }^{\circ}\text{C}$ ) is shown for reference.

Based on the thermal response of the 10 MHz PDMS-based SAW device, we conclude that it is difficult to maintain a thermally biocompatible environment for *C. reinhardtii* at high input voltage without an active cooling system. If possible, acoustic trapping of *C. reinhardtii*

cells would have to occur at a drive voltage of less than  $15 V_{pp}$  in a PDMS-based device. No such restriction exists for the 10 MHz glass-based device.

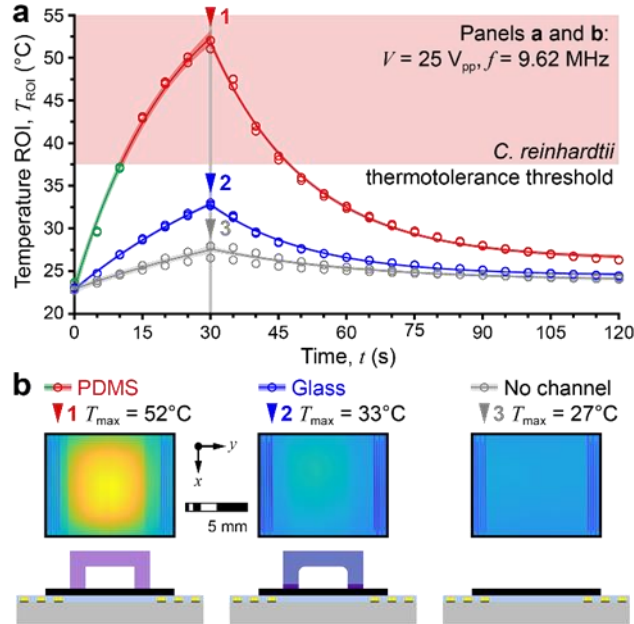


**Figure 3.5.** Progression of  $T_{ROI}$  for PDMS-based SAW, glass-based SAW, and no-channel SAW devices. (a) The  $T_{ROI}$  of glass-based SAW and no-channel SAW are under the *C. reinhardtii* thermotolerance threshold throughout the experiment. (b) Heat maps at 30 s, the time of maximum device temperature.

### 3.3.2 *C. reinhardtii* Trap-and-Release in 10 MHz Devices

To confirm the range of biocompatibility predicted by the IR thermography, we conducted a series of acoustic trap-and-release experiments for the  $\sim 10$  MHz devices loaded with *C. reinhardtii* cells. For the PDMS-based device operated at  $f = 9.62$  MHz,  $V = 5\text{--}15 V_{pp}$ , the acoustic radiation force was not large enough to overcome the intrinsic swimming capability of the cells, and cells did not become confined to nodal lines of the acoustic field. At  $20 V_{pp}$ , *C. reinhardtii* cell alignment was observed after approximately 20 s of actuation; however, it was clear that cell trapping was due to a loss of motility (or cell death) and not to acoustic confinement against the swimming force. Cells were not only held in nodal bands distributed in

the  $y$ -direction across the channel, but they also ceased swimming in the  $x$ -direction along the channel length. Similar behavior was seen at an operating voltage of  $25 V_{pp}$ , with cells quickly focusing to the nodes in 10–12 s (Figure 3.6 a, please refer to online video). Referring to Figure 3.4, the elapsed time to motility loss closely corresponded to the time required for  $T_{ROI}$  to reach  $37^\circ\text{C}$ , the *C. reinhardtii* thermotolerance threshold. For both the  $20 V_{pp}$  and  $25 V_{pp}$  cases, the cells remained at nodes after the signal was turned off, further confirming the loss of viability (see ‘Release’ in Figure 3.6 a, please refer to online video). The power required to generate a sufficient acoustic radiation force to trap the swimming cells resulted in device overheating that damaged the cells and effectively turned them into passive tracer particles. Thus, we conclude that the PDMS-based device is not able to trap live *C. reinhardtii* cells.

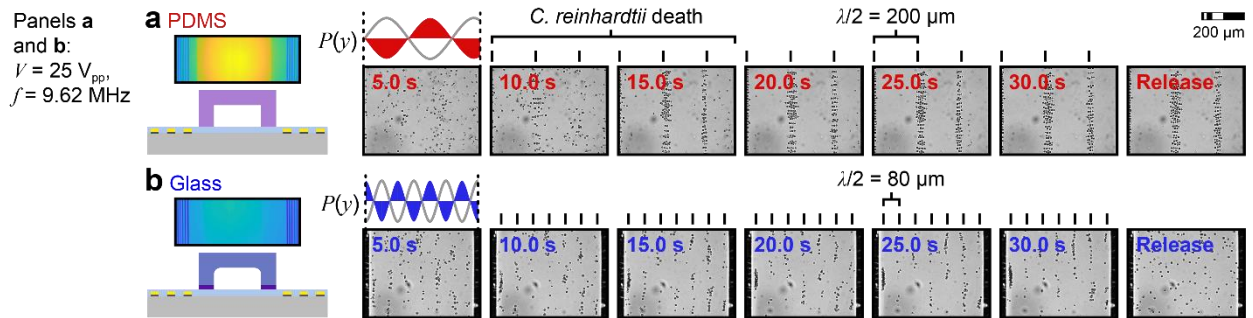


**Figure 3.6.** Trap-and-release at 9.62 MHz and 25 Vpp. (a) The PDMS-based device is not able to trap swimming *C. reinhardtii* but focuses immotile cells. Immotile *C. reinhardtii* cells do not redistribute after the signal is turned off. (b) The glass-based device successfully traps live *C. reinhardtii* at SBAW nodal positions. The motile *C. reinhardtii* cells redistribute evenly throughout the channel after the signal is removed.

We then repeated the trap-and-release experiments using a glass-based SAW device. At  $5 V_{pp}$  and  $10 V_{pp}$ , no cell lines formed, suggesting that the acoustic radiation force was still too weak to overcome the swimming force. When the applied voltage was increased to  $15 V_{pp}$ , the cells congregated at nodal lines corresponding to the acoustic half-wavelength of a standing bulk

acoustic wave. At 20  $V_{pp}$  and 25  $V_{pp}$ , the *C. reinhardtii* cells were trapped tightly within the nodes of the standing BAW field, but cells readily dispersed after the signal was turned off (Figure 3.6 b, please refer to online video). These results prove that the glass-based SAW device is able to trap-and-release cells without damaging them. The glass-based device provides similar functionality to our earlier BAW trap-and-release motility assessment platform,<sup>64</sup> combined with the notable advantages of SAW, including higher attainable drive frequencies and a planar actuator design.<sup>152, 153</sup>

### **3.3.3 Thermal Response and *C. reinhardtii* Trap-and-Release in 25 MHz Devices**

To determine the applicability of our results to higher operating frequencies, we also tested PDMS- and glass-based SAW devices at a frequency of 24.05 MHz, using the same drive voltages as for the 10 MHz devices. For higher-frequency operation, the thermal environment in the PDMS channel did not exceed the *C. reinhardtii* thermotolerance threshold until the applied voltage was 25  $V_{pp}$  (Figure. 3.7 a). In this case, the temperature within the ROI increased to 37°C at 20 s, predicting that cell death would begin near this exposure time. In contrast, the temperature within the glass channel stayed below 32°C, even for the highest applied voltage of 25  $V_{pp}$ .

We again confirmed our abiotic results using *C. reinhardtii* cell trap-and-release to assess the biocompatibility of both devices. In the 24MHz PDMS-based device, cells were not trapped within nodal lines at drive voltages from 5–20  $V_{pp}$ , likely due to the insufficient acoustic radiation force. At 25  $V_{pp}$ , the cells began to lose motility at around 20 s as expected (Figure 3.7 b, please refer to online video). Further, higher magnification images of treated cells suggested that some cells disintegrated, and intact cells exhibited extensive blebbing and other signs of

damage (see Figure 3.8). By contrast, in the 24 MHz glass-based device cell confinement began at 15  $V_{pp}$ , with tighter trapping observed at 20  $V_{pp}$  and 25  $V_{pp}$ . As with the lower frequency actuation at 25  $V_{pp}$ , the cells were trapped and then released without damage for operation at 24.05 MHz (Figure 3.7 c, please refer to online video). Unlike at the lower operating frequency, many cells are seen ‘hopping’ back and forth between adjacent nodal positions, which may indicate that the acoustic radiation force cannot overcome the maximum swimming force when cells are oriented perpendicular to the nodal lines, or that the trapping becomes less effective as the half wavelength approaches the size of the cells. It is also possible that for the glass-based SAW device, the BAW is not well-matched to the drive frequency of the SAW.

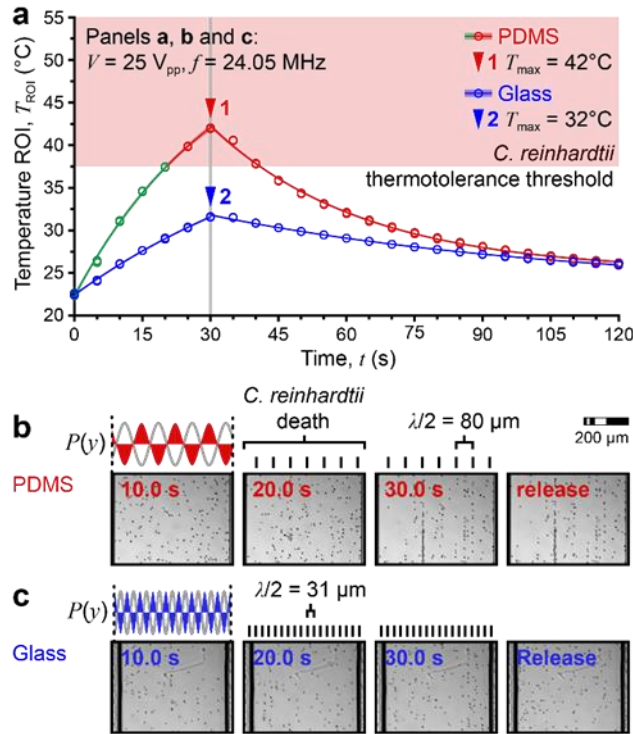


**Figure 3.7.** Thermal response and trap-and-release are correlated for the 24 MHz device operated at 24.05 MHz and 25  $V_{pp}$ . (a) The  $T_{ROI}$  progression of PDMS-based and glass-based SAW devices. (b) The PDMS-based device is not able to trap swimming *C. reinhardtii*, which become immotile at ~20 s. (c) The glass-based device is able to trap-and-release live cells.

Interestingly, in the PDMS-based device, alignment of immotile or dead cells was observed at both nodes and what appear to be antinodes, where they remained after the removal of the applied voltage (Figure 3.7 b, please refer to online video). We first thought that dead cells might focus at both nodal and antinodal locations due to the three-dimensional (3D) nature of the acoustic wave field (some lines of cells are blurry suggesting that they are positioned at different focal  $z$ -depths); however, a control experiment using 10  $\mu\text{m}$  poly(methyl methacrylate) (PMMA) beads verified the nodal locations at the half-wavelength of the SAW (Figure 3.7 b,  $\lambda/2 = 80 \mu\text{m}$ ). Thus, it is not entirely clear why dead cells focus to both nodes and antinodes. Further investigation is needed to determine whether the dead *C. reinhardtii* cell population may have different acoustophysical properties (i.e., density and compressibility) than the live cells or if indeed the 3D wave field affects cells differently than PMMA beads (e.g., if beads settle prior to focusing unlike swimming cells that initially fill the 3D channel).

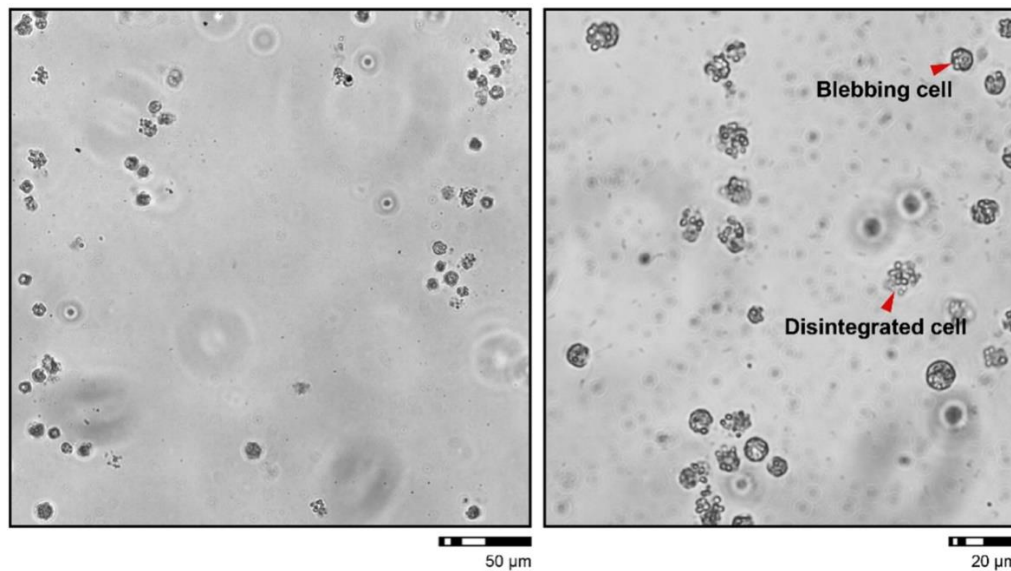


**Figure 3.8.** Brightfield microscopy images of heat-induced damage to *C. reinhardtii* cells after trap-and-release in the PDMS-based microchannel driven at 24.05 MHz and 25  $V_{pp}$ .

In summary, the 24 MHz PDMS-based SAW device was also not able to trap live *C. reinhardtii* cells due to a too-weak acoustic radiation force and/or lethal heating at higher input power. Dead cells were trapped in the nodal/anti-nodal lines of the SAW and remained there even after the signal was turned off. The 24 MHz glass-based SAW device successfully trapped live cells; cell confinement occurred at standing BAW nodes formed by the leaky SAW reflected between the glass walls of the fluid microchannel. The acoustic radiation force was strong enough to trap the cells prior to release, though cells were able to hop between trapping sites as the acoustic half wavelength ( $\sim 30 \mu\text{m}$ ) became comparable to the cell-plus-cilia diameter of  $\sim 20 \mu\text{m}$ .

### 3.4 Conclusions

Understanding the thermal transport characteristics of acoustofluidic devices is critical to their implementation, whether the goal is to control a temperature-sensitive process like PCR amplification of DNA or to mitigate potential damage to cells and biomolecules. Even for relatively low input powers where cell viability is less of a concern, biophysical and biochemical processes are affected by slight variations in temperature. For example, the swimming velocity of wild-type *C. reinhardtii* (strain CC-125) grown at 25°C has been reported to vary from 42  $\mu\text{m/s}$  to 123  $\mu\text{m/s}$  in the range from 10°C to 30°C.<sup>154</sup> In our laboratory, we have observed an increase in *C. reinhardtii* cell beat frequency from  $\sim 55 \text{ Hz}$  to  $\sim 75 \text{ Hz}$  over the smaller 15°C to 25°C range (unpublished data).

Aside from potential adverse effects on cells and biomolecules, separation and trapping performance can suffer when the operating temperature deviates significantly from the design conditions (typically room temperature). The electromechanical and acoustophysical properties of the piezoelectric substrate, channel superstrate, and liquid sample are strongly dependent on

temperature. Even so, thermal effects are often neglected or considered as less important aspects of system operation. Biological studies involving manipulation of cells using SAW-based devices rarely include appropriate controls or temperature calibration protocols.

In this work, we quantify the temperature field in PDMS- and glass-based SAW devices using an IR camera, incorporating a thin black paint layer to ensure accurate temperature measurement at the microchannel-substrate interface. Heat maps for both devices indicate that significant device heating is concentrated at the microchannel near the midpoint of the IDT aperture. These abiotic measurements are correlated with biological outcomes by performing acoustic trap-and-release of *C. reinhardtii* cells. We observe a loss of viability (and likely cell death) in PDMS-based SAW devices, suggesting that in those devices it is not possible to generate a force sufficient to trap swimming cells without excessive heating due to a high input power, vibration damping characteristics, and the poor thermal transport properties of PDMS. Glass-based devices support bulk acoustic waves driven at resonance by SAW to trap *C. reinhardtii* cells at lower input power, while effectively removing generated heat to maintain a thermally biocompatible environment. Thus, glass-based SAW devices can enable investigation of cell motility, cilia function, and the cellular response to mechanical and chemical stimuli with higher precision than comparable silicon/glass BAW devices driven by bulk transducers. We reiterate that it is the device heating that damages cells in PDMS-based SAW devices and not the strength of the acoustic field, as cells cease swimming before they are focused; the glass-based devices achieve a stronger field strength to confine cells without damage as demonstrated by the free-swimming cells after removal of the field. Our results highlight the importance of rigorous thermal analysis of SAW-based devices and promote glass-based hybrid BAW/SAW as a

compelling technology when high-frequency, short-wavelength ultrasonic standing waves are needed.

# Chapter 4: Cilia Dynamics Probing

## 4.1 Introduction

In Chapter 3, the thermal considerations of PDMS-based SAW and glass-based SAW were discussed. Thermal aspects of a one-dimensional PDMS-based SAW were summarized thoroughly, which has long been omitted and never carefully and thoroughly addressed in acoustofluidics. At the same time, a glass-based SAW device was also proven to generate a higher acoustic radiation force on particles for the same input powers relative to the PDMS-based SAW. In addition, the pressure nodal distances in the glass-based SAW device indicated that the standing waves in the microfluidic channel were actually BAWs. Importantly, this efficient one-dimensional glass-based SAW device can be modified to use for two-dimensional trapping of individual *C. reinhardtii* cells, which will be introduced in this chapter.

Though the motion of eukaryotic cilia and flagella is critical to microswimmer propulsion and directed movement of physiological fluids, the mechanisms responsible for this motion remain a mystery. In humans, coordinated beating of motile cilia contributes to fluid flow and/or clearance of foreign material in airways and cerebral ventricles, among other tissue cavities and lumens. Dysfunction of these slender organelles is implicated in a range of ciliopathies that includes primary ciliary dyskinesia (PCD), chronic otitis media, chronic obstructive pulmonary disease (COPD), and infertility.<sup>67, 70, 155-158</sup> The cytoskeletal structure of cilia (i.e., the 9 + 2 axoneme comprising nine outer microtubule doublets and two central singlets) is known, but the relationship between its form and function is not fully understood.<sup>83, 159</sup> Mammalian cilia are difficult to characterize efficiently, complicating studies with ex vivo tissue samples. Instead, the unicellular alga *Chlamydomonas reinhardtii* (*C. reinhardtii*), which shares a common axonemal

structure with human cilia, has been developed as a model organism for investigation of ciliary kinetics.<sup>160, 161</sup>

Biciliate wild-type *C. reinhardtii* cells swim with a characteristic breaststroke, achieving forward movement via synchronized power and recovery strokes at beat repetition frequencies of 50–80 Hz.<sup>162, 163</sup> In addition, a slight non-planarity of the asymmetric beat pattern results in slow rotation (at ~2 Hz) about the major body axis. The resultant motion is complex, and its full description requires imaging the rhythmically beating cilia with high temporal and spatial resolution. A micropipette is commonly used to hold the *C. reinhardtii* cell body during prolonged observation of the nearly planar ciliary beating; however, physical contact constrains rotational degrees of freedom, precluding characterization of the helical navigation that is critical to cell sensing of environmental gradients.<sup>164-166</sup> In addition to such analytical limitations, micropipette-based capture is tedious as *C. reinhardtii* cells swim approximately ten body lengths per second (~100  $\mu\text{m/s}$ ). High-throughput studies that use such physical confinement are also impractical due to the complexity associated with multiplexing of trap sites.

Noncontact trapping enables three-dimensional (3D) object manipulation without applying a torque that constrains cell body rotation. While optical tweezers are commonly used to manipulate passive nano-/microparticles,<sup>33</sup> applications with active matter are less well established. Long-term trapping and analysis of single motile *Escherichia coli* bacteria cells have been reported.<sup>167, 168</sup> Calibrated optical trapping has also been used for direct characterization of *C. reinhardtii* force dynamics;<sup>169</sup> however, minor discrepancies were found between measurements and previously reported ranges of swimming parameters. This suggests that optical trapping may affect swimming behavior, for example by perturbing the cilia motion and/or via localized heating.<sup>170</sup> A variety of other noncontact approaches are used to trap and

manipulate passive bioparticles, but most have proven ineffective for applications involving microswimmers due to insufficient trapping forces, thermal effects, and/or other practical limitations.<sup>171, 172</sup> Active methods may exploit electrical charge or polarizability (electrophoretic and dielectrophoretic trapping),<sup>173, 174</sup> or magnetic susceptibility (magnetic tweezers)<sup>175-177</sup> to distinguish and hold target particles within the suspension medium. If particles do not respond directly to the externally applied field, field-sensitive labels (e.g., immunospecific magnetic particles) are needed,<sup>29, 178</sup> which can affect cell physiology or viability. In this context, acoustic tweezers have emerged as a compelling alternative that offer non-contact, label-free trapping with high biocompatibility.<sup>108, 179, 180</sup>

Acoustic tweezers are considered gentle, as ultrasound exposure is found to have a negligible impact on cell viability and phenotype.<sup>62, 179</sup> Non-contact manipulation also avoids physical stress related to undesirable surface interactions for sensitive bioparticles. Acoustic trapping performance depends on intrinsic acoustophysical properties of the cells (size, density, and compressibility) through the acoustic contrast factor relative to the suspension medium. Thus, no labelling or modification of the cells or medium is typically needed. Acoustic tweezers for bioparticles employ either bulk acoustic (BAW) or surface acoustic waves (SAW) depending on application-specific requirements for spatial resolution and efficiency, among other practical considerations like fabrication complexity and suitability for integration. Applications of acoustofluidic manipulations in biology and biomedicine have grown exponentially, but there are few reports on trapping of active matter or motile microorganisms.<sup>19, 64, 87, 118, 124</sup> A higher acoustic radiation force is needed to overcome the propulsive force of the microswimmers, and the corresponding increase in input power often leads to excessive heating that can damage

biological cells. To our knowledge, use of acoustic tweezers for single-cell-level manipulation of microswimmers has not been demonstrated.

In this work, we report a novel hybrid acoustic tweezers that use standing surface acoustic waves (SSAW) to drive formation of a standing bulk acoustic wave (SBAW) field for multiplexed trapping and analysis of swimming *C. reinhardtii* cells. The approach breaks the frequency limitation of traditional BAW (< ~10 MHz) to provide the efficiency of BAW with the resolution of SAW. We achieve *C. reinhardtii* trapping at high throughput and a single-cell level, with sufficient temporal and spatial resolution to study ciliary kinetics without altering the biomechanical functioning of the cells or cilia. Cilia motion is quantified using an approach previously applied to uniciliate mutants that rotate in place without confinement; however, acoustic trapping enables study of wild-type biciliates. We first describe acoustic field-microswimmer interactions in our devices, using populations of *C. reinhardtii* cells to map the BAW field for various microfluidic chamber geometries and operating conditions. We confirm that temperature-controlled ultrasound exposure does not affect ciliary beat patterns. The method is applied to investigate synchronization of *cis* and *trans* cilia in environments with varying medium viscosity. We further establish the utility of non-contact trapping to assess 3D helical swimming of wild-type *C. reinhardtii*. Finally, we demonstrate for the first time use of acoustic positioning (e.g., nodal shifting via frequency switching) to study how cilia respond to mechanical perturbation.

## **4.2 Trapping and Patterning Cell Populations**

In Chapter 3, one dimensional trapping of populated cells was demonstrated. It was shown that bulk acoustic waves could be driven by surface acoustic waves efficiently. It is thought that BAWs were driven by SAWs as the ‘leaky waves’ entered the microfluidic chamber from the

substrate forming BAW due to the acoustic impedance mismatch between side glass channel walls and the fluid. The SAW alone was not strong enough to affect positions of *C. reinhardtii* as BAW dominated the pressure field in the chamber. This observation led to the idea that 2D BAW might be driven by a single pair of IDTs (1D SAW) utilizing wave deflections inside of glass chamber. Thus, square devices with varying different IDTs were designed, fabricated, and loaded with *C. reinhardtii* to test this hypothesis.

#### **4.2.1 Cell Patterning in Square/Diamond Chambers**

Two kinds of square chambers were designed: a square chamber with side lengths parallel to the fingers of the IDTs and a diamond chamber with sides oriented at 45° to the fingers of the IDTs. All the side lengths of the chambers were carefully designed and fabricated to match the drive frequency to the geometry of the glass BAW microfluidic chamber. The side lengths of 10 MHz and 20 MHz devices were designed to be 545 μm and 270 μm, which matched three and one half bulk acoustic wavelengths at these operating frequencies. Both glass channels were wet-etched to ~30 μm deep, to reduce acoustic streaming effects and confine z-direction movement of swimming *C. reinhardtii*. Special care was taken in HF wet etching and bonding of glass channels to maintain accurate channel dimensions.

##### **Square Chamber Cell Patterning**

Prior to loading cells into the square glass microfluidic chamber, the channel was flushed with isopropyl alcohol to avoid air bubbles and then pretreated with 3% (w/V) bovine serum albumin (BSA) in phosphate buffered saline (PBS) solution to avoid cell attachment to the channel walls. Wild-type *C. reinhardtii* cells were loaded into the microfluidic chamber. The same trap-and-release experiment was performed as described previously. The power used here was lower than previously described but was still strong enough to trap the microswimmers. Two different

devices targeting operation at  $\sim 10$  and  $\sim 20$  MHz were made; however, no adjustment of the operating frequencies and power achieved a well-structured  $7 \times 7$  matrix pattern as desired (see Figure 4.1). For example, acoustic waves propagating in the  $x$ -direction dominated the observed behavior of 20 MHz devices. Here, one dimensional trapping nodal lines were formed inside of the fluidic chamber. The 7 nodal lines show that the standing waves in lateral direction are not strong enough to interact with the longitudinal standing bulk acoustic waves preventing formation of a grid pattern. In contrast, for 10 MHz devices, neither straight nodal lines nor the desired matrix of trapping locations was observed.

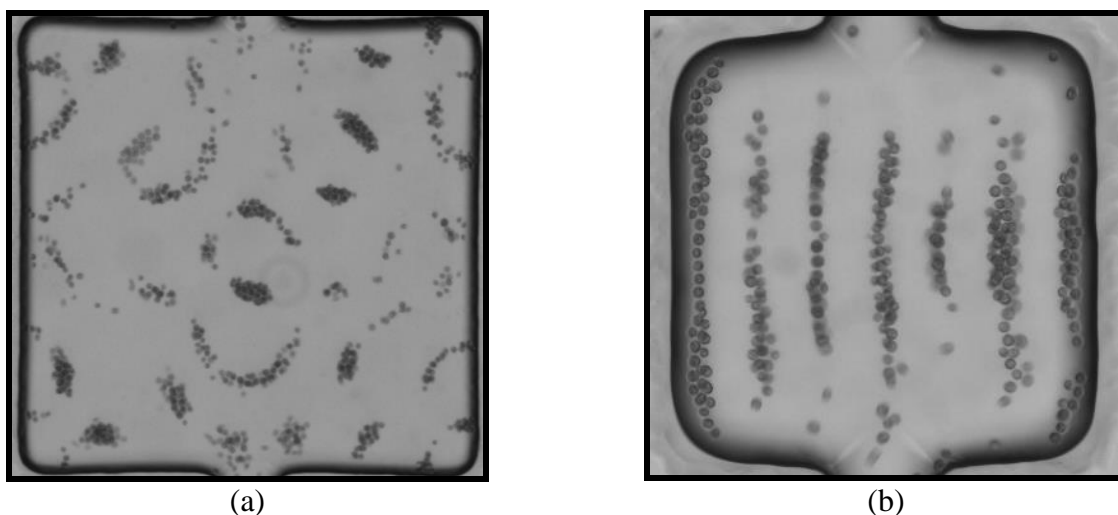


**Figure 4.1.** Square chamber cell trapping for BAW driven by SAW device. (a) A random pattern formed by *C. reinhardtii* at  $\sim 10$  MHz; the side length of the microfluidic chamber is  $545 \mu\text{m}$ . (b) One dimensional cell pattern formed in  $\sim 20$  MHz devices; the side length of the microfluidic chamber is  $270 \mu\text{m}$ .

In summary, for all fabricated square chamber devices, the desired 2D matrix pattern could not be formed regardless the input parameters. This work suggested that the square chamber is not ideal for patterning cells in two dimensions, which is needed for single cell trapping as well. Based on the one-dimensional cell sorting at 20 MHz, however, it was thought that the waves could be diffracted and also reflected by changing the angle between the square

chamber and IDT fingers. To distinguish from the ‘square chamber’, the tilted angle chamber was termed ‘diamond chamber’, which will be discussed in the following section.

### **Diamond Chamber Cell Patterning**

The ‘diamond’ chamber is a square chamber that is tilted at 45 degrees relative to the IDTs.

Three devices were made for operation at 6.6 MHz, 8.1 MHz and 9.6 MHz (corresponding to 600  $\mu\text{m}$ , 480  $\mu\text{m}$ , and 400  $\mu\text{m}$  SAW wavelength). The side lengths of the three diamond chambers were kept the same at 545  $\mu\text{m}$ , which were expected to form 5 x 5, 6 x 6, and 7 x 7 matrices. A 20 MHz device with a side length of 270  $\mu\text{m}$  was also designed and fabricated, which was expected to form a 7 x 7 matrix. By adjusting the frequency and power, the 6.6 MHz and 8.1 MHz devices formed almost perfect 5 x 5 and 6 x 6 matrices, respectively, as shown in Figure 4.2. The 9.6 MHz device did not form a perfect 7 x 7 matrix, but it was able to trap cells strongly in an array of pressure nodal positions. The 20 MHz device also formed a ‘pseudo’ 7 x 7 matrix, but the nodes formed by the diamond channel were not perfect due to the increased effects of glass isotropic etching for the smaller chamber size; especially high accuracy was needed to achieve dimensions matching the higher frequency actuation. In addition, the power needed to trap the microswimmers was quite low, with drive voltages ranging from 5–15  $V_{pp}$  (recall the range of voltages for earlier trap-and-release experiments of up to 25  $V_{pp}$ ), which demonstrates the efficiency of the BAW driven by SAW system. Finally, the cells could be released after trapping without use of cooling strategies, showing the great biocompatibility of this technique. The 9.6 MHz device was chosen as the device for single cell trapping due to its high throughput in the limited microscope field of view, which will be introduced later.

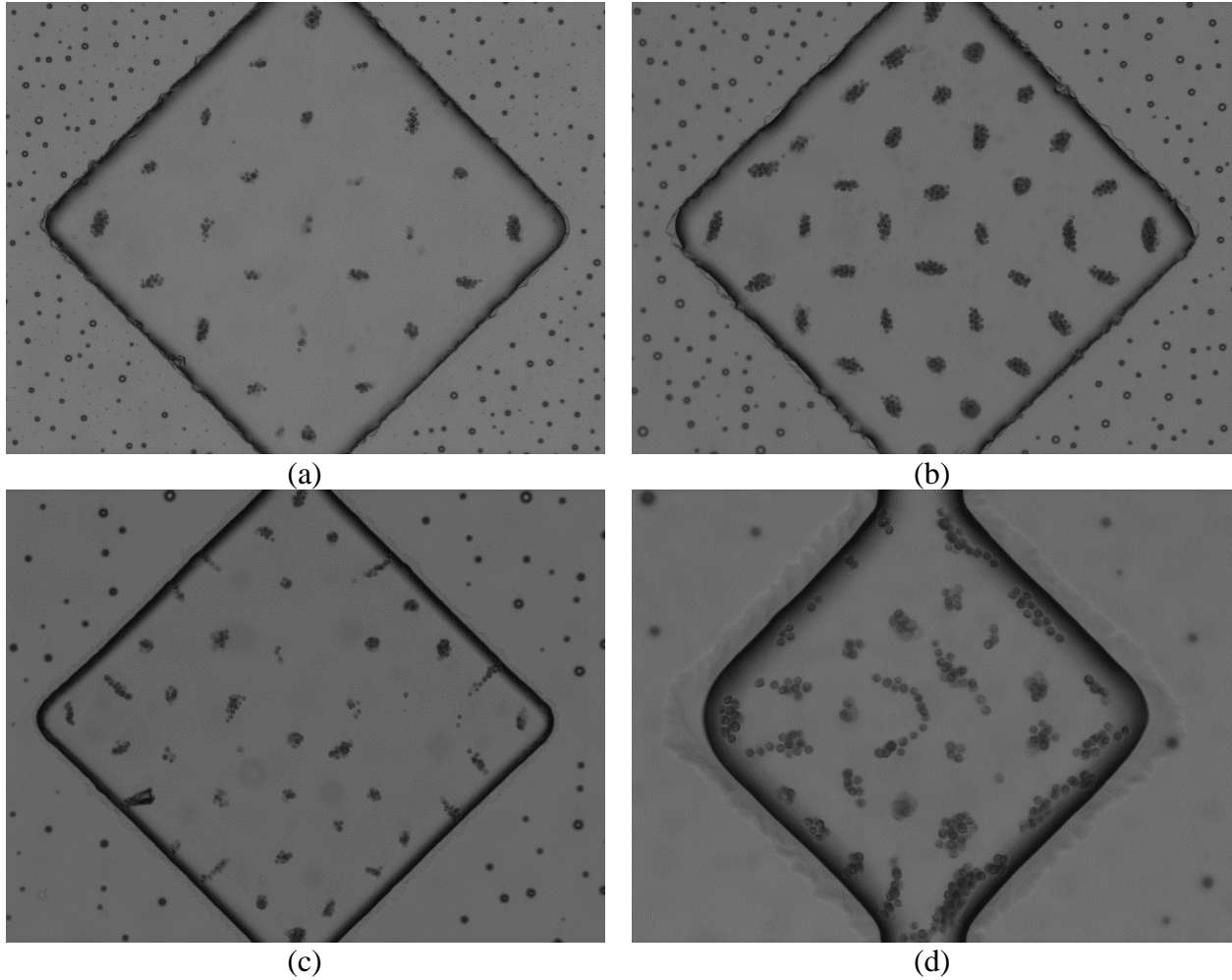


**Figure 4.2.** Cell patterning matrices. (a) 5 x 5 nodal positions for a 6.6 MHz device, (b) 6 x 6 for a 8.1 MHz device, (c) 7 x 7 for a 9.6 MHz device, and (d) 7 x 7 for a ~20 MHz device. Chambers for (a)-(c) have a side length of 545  $\mu\text{m}$ , while the chamber for (d) has a side length of 270  $\mu\text{m}$ .

The acoustic patterns formed by *C. reinhardtii* proved that 2D standing BAWs can be formed using one dimensional SAWs. Again, it appears that the surface acoustic waves formed on the  $\text{LiNbO}_3$  leaked into the microfluidic channel with less attenuation due to the use of a glass microfluidic channel.<sup>132</sup> The waves diffracted and reflected after leaking into the glass diamond channel, and finally formed bulk acoustic waves because of the large acoustic impedance mismatch between glass and the fluid. The bulk acoustic waves dominated over the one-dimensional surface acoustic waves dictating the predominant pressure field structure. Thus, the

diamond chamber appears to distribute leaky waves in two dimensions equally. Although the basic theory is simple, a deeper understanding of this technique could be gained from a transient acoustics model; however, the computational cost of an accurate 3D model might be high. Such model development is recommended for future work.

#### 4.2.2 Cell Patterning in Circular Chambers

To further establish the concept of the standing BAWs formed by the standing SAWs, circular chamber devices at ~10 MHz and 20 MHz were designed and fabricated, with the corresponding side lengths of 545  $\mu\text{m}$  and 270  $\mu\text{m}$ , respectively. The acoustic patterns were expected to form three concentric rings with a single point (node) at the center of the chambers. After pretreating the channel and loading *C. reinhardtii*, the expected acoustic patterns were found in both devices by adjusting the frequency and power (see Figure 4.3).

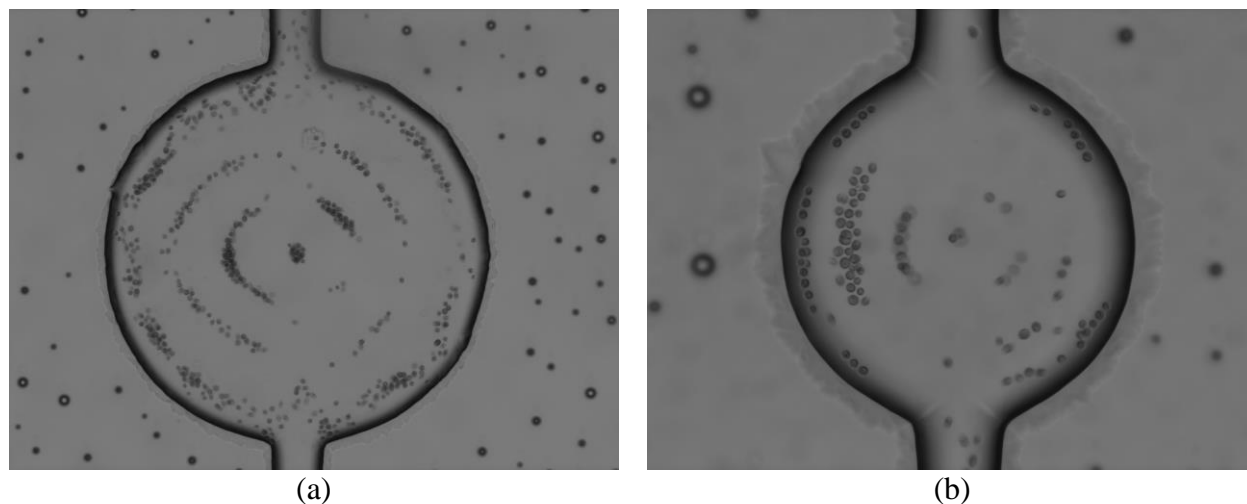


**Figure 4.3.** Cells patterned in concentric ring shapes at ~10 MHz and ~20 MHz. (a) The circular chamber resonant shape of a ~10 MHz device. (b) ~20 MHz device resonance imaged using swimming *C. reinhardtii*. The circular chamber in (a) has a diameter of 545  $\mu\text{m}$ , while the chamber in (b) has a diameter of 270  $\mu\text{m}$ .

The ring pattern was formed by swimming *C. reinhardtii*, which proved that the standing BAWs formed inside of microfluidic chamber were generated by standing SAWs. In addition,

this method utilizing a circular chamber is potentially useful for transient chemical exposure investigations with continuous flow conditions at the singular point (pressure node) in the middle of the circular chamber where the strongest trapping occurs. The biocompatibility of the circular chamber was confirmed by performing the following experiment: the microswimmers were loaded in the microfluidic chamber and trapped for 10 min without Peltier cooling stage; after turning off the power, the microswimmers were released successfully and redistributed quickly throughout the chamber. Again, this further showed that the presented approach is both an efficient and biocompatible method.

### **4.3 Single Cell Trapping**

Here, the focus is probing of cilia dynamics for *C. reinhardtii* cells in acoustic traps. The glass materials used in previous microfluidic devices were 1.5 mm thick, which allows for imaging at the micrometer level using a 100x dry objective; however, the diameter of *C. reinhardtii* cilia is only ~200 nm, requiring a high magnification oil-immersion objective (60–100x) to provide adequate imaging resolution. Such an objective works only with microscope slides no thicker than 0.12–0.2 mm as the working distance for oil-immersion microscopy is in the range of 0.17–0.21 mm. Thus, the previous glass-based SAW devices were too thick to be used with an oil-immersion objective, so that new microfluidic channels wet-etched into a microscope slide were designed and fabricated. These thinner channels were then bonded to the one-dimensional IDTs as before. The detailed fabrication process can be found in Chapter 2. The new device provided unprecedented images of ciliary motion for acoustically confined *C. reinhardtii* cells, as shown in Figure 4.4. This class of devices were used for all subsequent cilia dynamics probing described here.

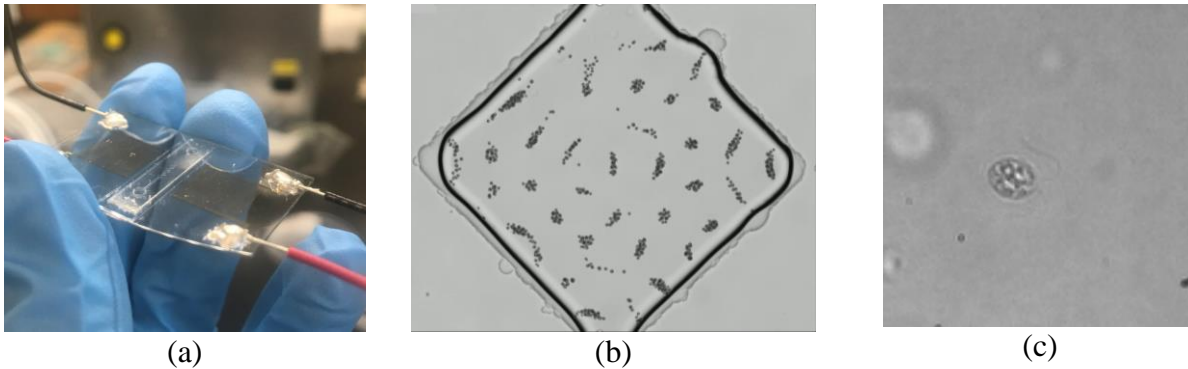


**Figure 4.4.** Device for use with an oil-immersion microscope objective and images of its trapping performance. (a) Assembled device, (b) trapping of a cell population at 9.60 MHz and 5 V<sub>pp</sub> imaged with a 10x microscope objective. (c) Trapping of a single cell imaged using a 60 x oil-immersion objective at the same frequency and an input voltage 10 V<sub>pp</sub>.

### 4.3.1 Cilia Waveform Probing

Although the main structures of the axoneme have been studied extensively, the mechanisms that produce the propulsive and oscillatory waveforms of cilia are still not completely understood. As a unicellular alga, *C. reinhardtii* is an ideal model for studying ciliary mechanisms. Using its two cilia, wild-type *C. reinhardtii* has a typical swimming speed of 100 μm/s. Researchers commonly have used a micropipette to hold the cell in position for study, which is complex in operation and time consuming.<sup>165, 181</sup> The *uni1* mutant has only one cilium, which rotates the cell body around an axis in a plane perpendicular to the beating plane. This unciliated cell has a ciliary waveform very similar to that of biciliated wild-type cells, although not completely so.<sup>182, 183</sup> Thus, studying the cilia dynamics of biciliated cells is still necessary.

Using the developed acoustofluidic device, which is easy to operate and provides non-contact manipulation, biciliated wild-type *C. reinhardtii* and its mutants can be trapped. The cilia dynamics of various mutants are not discussed here as their behavior is beyond the scope of this thesis. Using the new acoustofluidic method, the primary objective of the thesis work was to

study the frequency, waveform, curvature, and amplitude of the ciliary movements of wild-type biciliated cells and uniciliated cells. The work to date is described in the following sections.

### **Method and data overview**

To trap single cells using the device, the previous cell sample was diluted with cell medium in a ratio of 1:10. Although the diluted cell suspension could not ensure that every node was occupied by a cell, it enabled a number of individual cells to be trapped for further analysis. In this work, 30 videos each of beating cilia for both biciliated and uniciliated cells were analyzed. All videos of beating cilia were recorded three hours subsequent to the onset of gametogenesis, so that the analyzed cells had fully matured. The lengths of the cilia varied from 8–12  $\mu\text{m}$ . The oil-immersion microscopic images yielded clear images in almost all cases, and the ciliary movements were recorded at 2000 frames per second (FPS) using a high speed camera (Photron FASTCAM Mini AX 200, 32GB) with a resolution of 0.194  $\mu\text{m}/\text{pixel}$ . For the waveform analysis, 200 frames were extracted of a swimming trapped cell. Extracted frames were of high

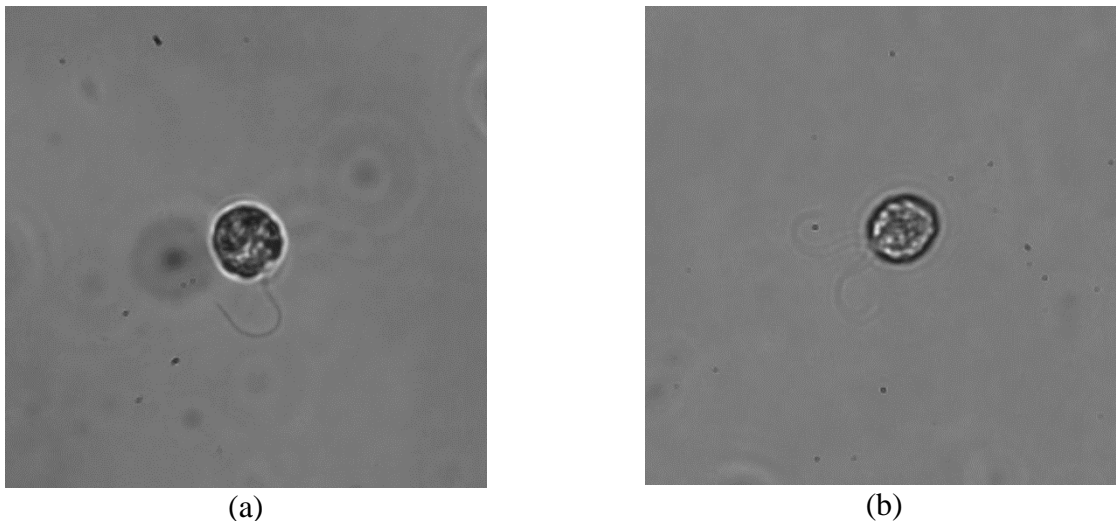


**Figure 4.5.** Acoustic trapping of individual uniciliated and biciliated wild-type *C. reinhardtii* cells. (a) Uniciliated cell (*uni1*) in an acoustic trap. (b) Biciliated cell (CC125) in an acoustic trap.

enough quality to analyze waveform for biciliated cells as previously described.<sup>184</sup> Examples of acoustically trapped uniciliated and biciliated wild-type cells are shown in Figure 4.5.

### Periodicity of beating from analysis of cilia motion

As shown in Figure 4.6, the normalized autocovariance of the cilia angle was used to analyze the periodicity of beating. At each spatial location,  $s$ , along the cilium, the MATLAB function  $xcov$  was used to estimate an autocovariance function  $a(s, \tau)$  from the waveform angle  $\theta(s, t)$ . An average autocovariance function for the cilium,  $a_c(\tau)$ , was also computed by averaging  $a(s, \tau)$  over the spatial dimension  $s$ . The average peak of the autocovariance at nonzero lag ( $\hat{a}_c$ ) was used both as a marker of periodicity and to find the period of ciliary beating. Theoretically, an  $\hat{a}_c$  value of 1.0 represents perfect periodicity, with each covariance trace perfectly superimposed. In a previous publication, our group reported that uniciliated cells, *uni1*, with cilia lengths longer than 4  $\mu\text{m}$ , had typical peaks of  $\sim 0.8$ .<sup>77</sup> However, if there was no peak detected, or if the peak value was very small (i.e., less than 0.15), then the cilium was considered nonperiodic.<sup>77</sup>

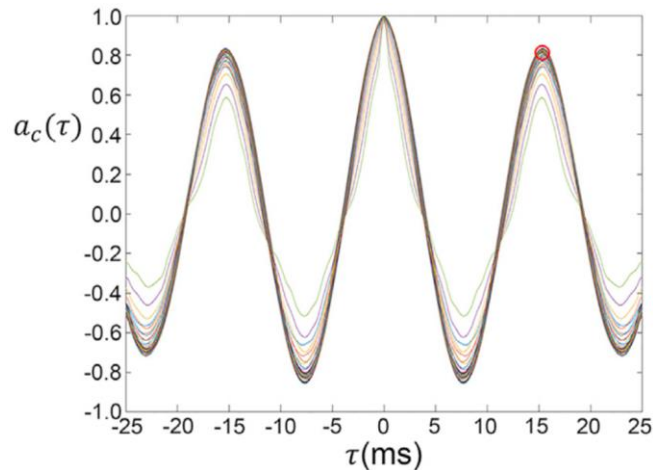


**Figure 4.6.** Quantification of periodicity of ciliary beating. Example plot of the normalized autocovariance of the cilium tangent angle  $a_c(\tau)$ , plotted versus the time lag,  $\tau$ . The period of beating is defined by the first peak with a magnitude greater than a specified threshold (0.15) at a nonzero lag (red circle).

For biciliated cells, the *cis*-cilium, identified either by its proximity to the eye spot or by its more regular beating, had a peak of  $\sim 0.8$ , as expected. However, the value of the peak normalized autocovariance  $\hat{a}_c$  of the *trans*-cilium was  $\sim 0.65$ , less periodic than the *cis*-cilium. This difference was also expected as there is a ‘slip’ in the beating of the *trans*-cilium, which shows a faster beat frequency than the *cis*-cilium: during 2-3 normal beats of the *cis*-cilium, the *trans*-cilium typically performs 3 or 4 beats.<sup>185, 186</sup>

The autocovariance analysis determined the periodicities of the *cis* and *trans* cilia of biciliated cells, and the single cilium of uniciliated cells. The peak normalized autocovariance of the *cis*-cilium of a biciliated cell was similar to that of the cilium of a uniciliated cell, which was  $\sim 0.8$ . However, the peak value of the *trans*-cilium of a biciliated cell had a smaller value of  $\sim 0.65$ , which indicated less regular beating, the ‘slip’ mentioned above. It should be noted that the autocovariance could only be determined for the extracted 200 frames or  $\sim 0.1$  second. Therefore, this implementation would not be applicable for a long beating cycle (e.g., 1 second) of the *cis* and *trans* cilia of biciliated cells because the *trans*-cilium of biciliated cells does not always exhibit a slip motion. However, in that case, the *trans*-cilium could be identified once a slip motion was observed.

### **Waveform analysis during periodic beating**

All the waveform parameters were computed over the length of the cilium and the duration of the beat. From the mathematical description, the polynomial coefficients of the average waveforms for both *cis* and *trans* cilia were obtained. Dimensionless waveform examples for each cilia group are shown in Figure 4.7. These plots represent the shape of the waveform at regular intervals corresponding to 1/10 of a cycle to illustrate qualitative differences in waveform shape.

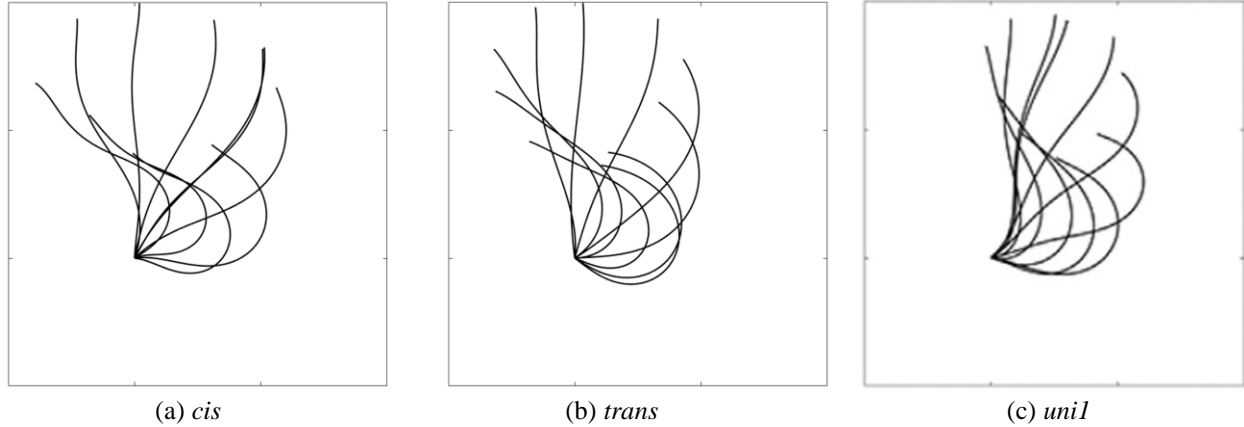


**Figure 4.7.** Dimensionless waveforms of each cilia group. (a) Representative dimensionless waveform of the *cis*-cilium of CC125. (b) Representative dimensionless waveform of the *trans*-cilium of CC125. (c) Representative dimensionless waveform of the *uni1* unciliated mutant.

In addition, by extracting waveforms of cilia, differences in physical curvature, bend amplitude, and oscillatory amplitude of all these three types of cilia are observed. More detailed comparison of each cilium group is provided in the following section.

### **Beat frequency and waveform shape**

The 9.6 MHz device was chosen as the device for single cell trapping and cilia waveform probing for its high throughput (large number of trap sites) and demonstrated negligible effect on cilia beating. The temperature of the cooling stage was set at 20°C. The wild-type biciliated and unciliated *C. reinhardtii* were trapped acoustically in a 25  $\mu\text{m}$  deep wet-etched coverslip glass (~170  $\mu\text{m}$  total thickness) chamber, and swimming was recorded using phase-contrast microscopy with an oil-immersion objective (2000 frames per second). A sequence of 202 frames (~0.1 s) was extracted from each recording for the approximately planar cilia beating analysis for both kinds of cells. Again, detailed device fabrication processes can be found in Chapter 2, and steps for analysis of ciliary waveform have been reported previously.<sup>76, 77, 187</sup>

Beat frequency was calculated using the inverse of time lag corresponding to the peak auto-covariance in cilia angle, which is used for periodicity detection. Fifteen biciliated wild-type cells that exhibited regular synchronous beating were recorded and analyzed. We also tracked 30 unciliated wild-type cells for comparison. For the biciliated cells, the cilia had a beat frequency around 60 Hz (mean  $\pm$  SD,  $60.77 \pm 8.68$  Hz). However, the cilium of unciliated cells had a slightly higher beat frequency of around 67 Hz (mean  $\pm$  SD,  $67.24 \pm 10.62$  Hz). The bend amplitude ( $\theta^{\text{SD}} = \text{std}(\theta)$ ) for cilia of biciliated cells was 0.90 rad ( $0.90 \pm 0.04$  rad), slightly higher than the value for cilia of unciliated cells, which was 0.81 rad ( $0.81 \pm 0.04$  rad). In addition, the average curvature  $\kappa^-$  (averaged over the length of cilium and the full cycle of beating) for biciliated cells was  $-0.18$  rad/ $\mu\text{m}$  ( $-0.18 \pm 0.04$  rad/ $\mu\text{m}$ ), which was lower than that for cilia of unciliated cells, which was  $-0.20$  rad/ $\mu\text{m}$  ( $-0.20 \pm 0.03$  rad/ $\mu\text{m}$ ). For periodic beating of wild-type biciliated cells and unciliated cells, the beat frequency and waveform shape could be observed and measured.

In some cells the synchronous beating was interrupted by an asynchrony, which is also known as a ‘slip’ motion. During the ‘slip’ motion, the *trans*-cilium (the one farther away from the eyespot) of biciliated cells showed a faster average beat frequency by about 30%, while the *cis*-cilium of biciliated cells retained the original beat frequency and waveform.<sup>188</sup> In our study, twelve synchronously beating cells that was interrupted by an asynchrony were recorded and analyzed. During the asynchronous beating, the mean beat frequency of the *trans*-cilium of biciliated cells had a value of 77 Hz ( $77.25 \pm 5.88$  Hz), though the mean is not fully representative of what is an inherently transient process, as shown in Figure 4.8. This value is ~30% higher than that of the *cis*-cilium. In addition, the maximum beat frequency for a single beating cycle in each asynchrony was ~50% higher than that for synchronous beating. The

average amplitude of the *trans*-cilium was only 0.81 rad ( $0.81 \pm 0.03$  rad), about 10% lower than that for the *cis*-cilium ( $0.90 \pm 0.03$  rad). The mean curvature of the *trans*-cilium ( $-0.20 \pm 0.03$  rad/ $\mu\text{m}$ ) was also higher than that of the *cis*-cilium ( $-0.18 \pm 0.03$  rad/ $\mu\text{m}$ ). The low amplitude and high curvature of the *trans*-cilium indicates a compressed waveform shape during the asynchrony. However, the amplitude and curvature of the *trans*-cilium of biciliated cells and the cilium of unciliated cells have comparable values.

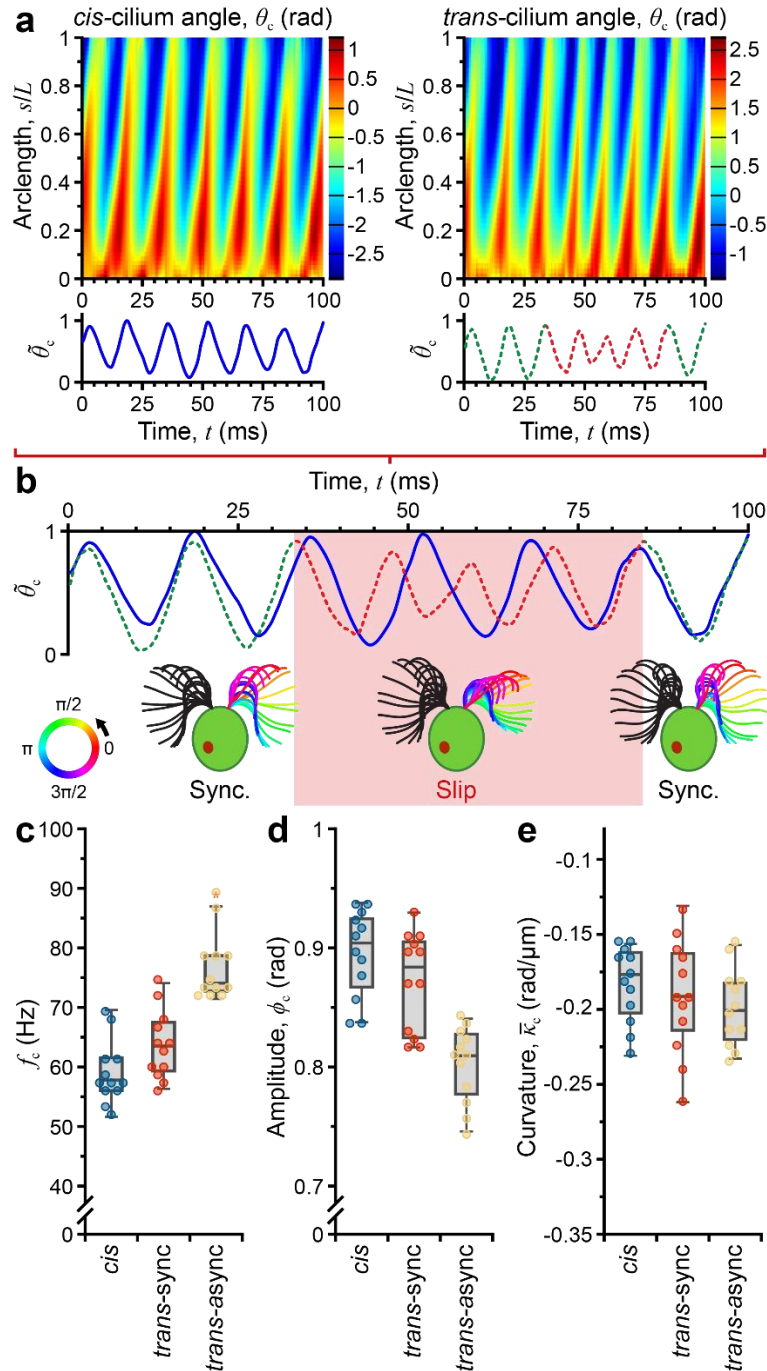


**Figure 4.8.** A detailed comparison of key waveform parameters between the *cis*-cilium and *trans*-cilium during a ‘slip’ motion. (a) Amplitude comparison of the *cis*-cilium and *trans*-cilium. The *cis*-cilium has periodic beating during asynchrony, however, the *trans*-cilium beats faster during asynchrony, which is highlighted by the red dashed line. (b) Waveform comparison of the *cis*-cilium and *trans*-cilium during asynchrony. (c) Mean beat frequency, waveform shape comparison ((d) amplitude and (e) curvature) during ‘slip’ motion.

In general, for periodic (synchronous) beating of biciliates and uniciliates, the cilia of each have different beat frequencies and waveform shapes. During asynchronous beating, the *trans*-cilium of biciliated cells has a compressed waveform compared to the *cis*-cilium, but has a similar waveform shape to the uniciliate cilium. The beat frequency of *trans*-cilia during asynchrony elevated by ~30% in average, where the highest rise went up by ~50%. The effect of ultrasound exposure on cilia beating was also investigated, and there was no detectable change in waveform shape (amplitude and curvature), which is discussed in section 4.3.5 below. The beat frequency was slightly higher in the acoustic trap due to a small temperature elevation. The temperature elevation was only about 1–2°C after a full study of the temperature effect on cilia beating during acoustic trapping, which is also explored in section 4.3.6. In summary, the innovative BAW/SAW acoustic tweezers provide an ideal tool to investigate cilia beating dynamics for all types of *C. reinhardtii* cells due to a strong trapping force, an outstanding biocompatible environment, the highest resolution optical imaging, high-throughput capability, and long observation imaging.

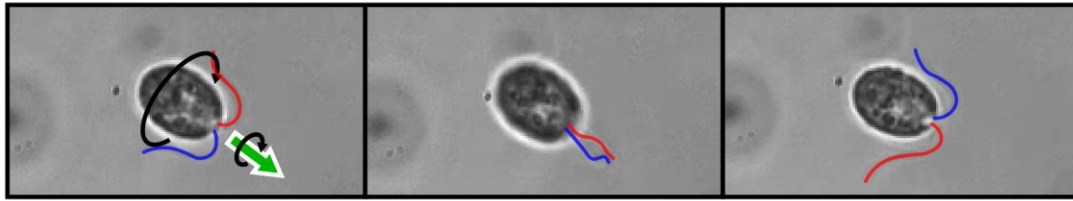
### **4.3.2 Observation of Cell Helical Motion in Biciliate *C. reinhardtii***

Motile organisms swim in bulk fluids to explore the world as a three-dimensional environment in helical trajectories that form a corkscrewing motion around their body axis. The helical motion is a ubiquitous strategy for motile eukaryote cells to steer toward or away from external stimuli (light, gravity, and chemicals). Those motile cells adjust their swimming motion with beating cilia, according to the stimulus obtained by subcellular sensors (eyespot, receptors, etc.) that periodically scan the environment. Such actions can enhance signal perception that is important for their evolutionary progress.

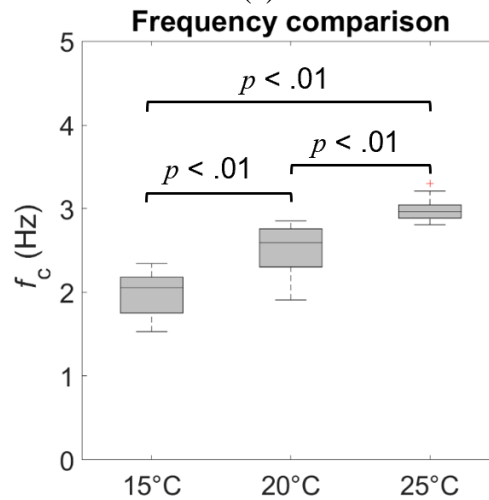
For algae cells, cilia beating is essential to controlling the cell reorientation and navigation to photostimuli. Wild-type *C. reinhardtii* swims along left-handed helices in a breaststroke mode, rotating about the body axis at 2–3 Hz.<sup>163, 166</sup> The eyespot of each cell scans the environment and then adjusts its motion by periodic shading. However, the mechanism of this characteristic helical motion has not been fully understood. A recent study and model showed that the helical motion is caused by a slight non-planarity in biciliate driving forces.<sup>189</sup> In this section, the developed method is used to trap biciliated *C. reinhardtii* and to study its helical motion.

First, frequency of rotation is quantified by acoustic trapping of the biciliated cells (see Figure 4.9 (a)). The frequency was calculated from the inverse of time for 12 flips (6 complete rotations) in total. At 20 °C, the frequency of rotation is about 2.5 Hz (mean  $\pm$  SD,  $2.50 \pm 0.34$  Hz), with a sample size of ten (see Figure 4.9). This rotation frequency is in the range of estimation by other research groups. The rotation frequency of biciliated cells was also determined at 15 °C and 25 °C using the same method and with the same sample size. At 15 °C, the frequency of rotation was about 2.0 Hz (mean  $\pm$  SD,  $1.99 \pm 0.28$  Hz), while the frequency of rotation was  $\sim$ 3.0 Hz (mean  $\pm$  SD,  $2.99 \pm 0.18$  Hz) at 25 °C. There is about a 0.5 Hz difference in frequency for every 5 °C difference in temperature. It is thought that the previously observed dependence of cilia beating frequency on temperature causes the observed difference in rotational motion. The higher the environmental temperature, the higher the cilia beat frequency, and thus, the higher the asymmetric driving forces that cause the cell to rotate about its axis increasing the rate of rotation. A full comparison is illustrated in Figure 4.9 (b).

### Biciliate w.t. CC-125 3D helical navigation



(a)



(b)

**Figure 4.9.** Rotation frequency comparison for biciliated *C. reinhardtii* cells in an acoustic trap at different temperatures ranging from 15 °C to 25 °C.

Though the present work is not the first observation and characterization of helical swimming, the complex 3D swimming of *C. reinhardtii* remains an underexplored aspect of their behavior. The acoustic trapping method provides an excellent tool to study this motion with high spatial and temporal resolution and without placing a torque on the cell during confinement. Although only rotation frequency and temperature effects were investigated here, this represents a promising future research direction.

### 4.3.3 Analysis of Cilia Synchronization in Biciliate *C. reinhardtii*

In cilia dynamics research, mechanical loading can be varied by increasing the viscosity of the cell medium, which allows investigation of mechanical feedback in coordination of dynein activity. Quantitative waveform analysis paves the way to investigate such motor activity.<sup>190</sup>

Previous studies have shown that quantitative changes in waveform may indicate differences in dynein activity.<sup>78, 191, 192</sup> Although researchers have used this technique to study dynein activity, the cilia motion of wild-type *C. reinhardtii* under wide variations in viscosity has never been fully studied. Here, the new acoustic microfluidic technology is used to investigate the effect of the viscosity on cilia motion of biciliated wild-type *C. reinhardtii* cells. The cilia beat frequency, amplitude, and curvature were investigated in the *cis*-cilium and *trans*-cilium separately.

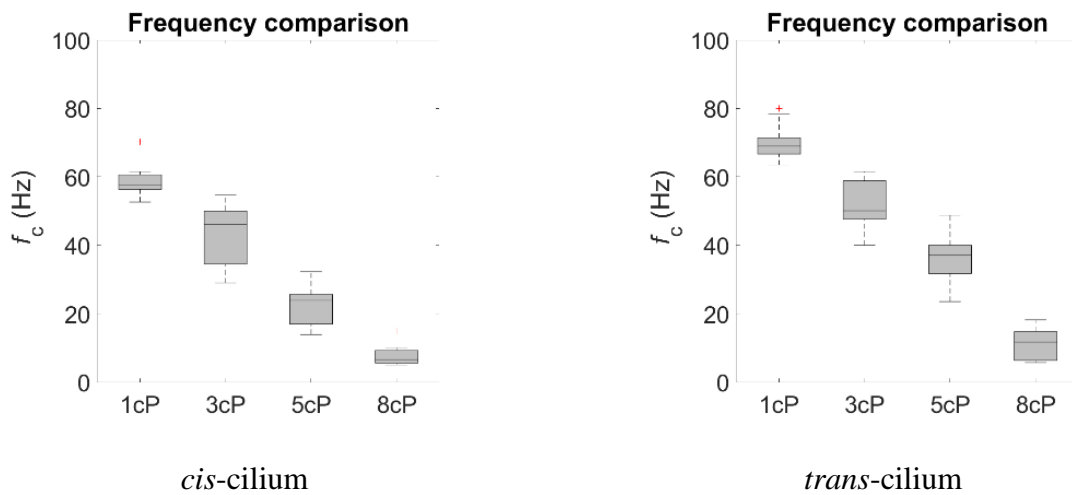


**Figure 4.10.** Frequency comparison of the *cis*-cilium and *trans*-cilium groups. For both groups, the frequency decreases with increasing viscosity.

The beat frequency of both cilia decreased with increasing viscosity, although to different degrees, as shown in Figure 4.10. Most importantly, the ratio of beat frequency of the *trans*-cilium over the beat frequency of the *cis*-cilium increased as the viscosity increased. This is because the ‘slip motion’ became more pronounced at high viscosity. Where a single ‘slip’ was observed at 1cP, up to four ‘slips’ were seen at 8 cP. Increase in occurrence of slip motion a big ‘slip motion’ can be explained by the large force difference in these two near-identical cilia at high viscosity, as the hydrodynamic force is proportional to viscosity. Out-of-plane beating was

also more obvious at high viscosity than at lower viscosity. However, the whether dynein activity changes inside of the cells contribute to these phenomena is unknown.

For the *cis*-cilium, a general decrease in amplitude was observed with increasing viscosity, as shown in Figure 4.11 (a). However, at 8 cP, the *cis*-cilium beating amplitude ranged from 0.3 to 0.9, likely due to the more pronounced ‘slip motion’. For the *trans*-cilium, although a general decrease in amplitude was seen as the viscosity increased from 1cP to 5 cP, a small increase in amplitude was observed at 8 cP (see Figure 4.11 (b)). This result is consistent with a previous report using *uni1* cell.<sup>190</sup> A slight increase in amplitude was observed as the viscosity increased beyond 5 cP. It is thought that the cell might react actively at this high viscosity.

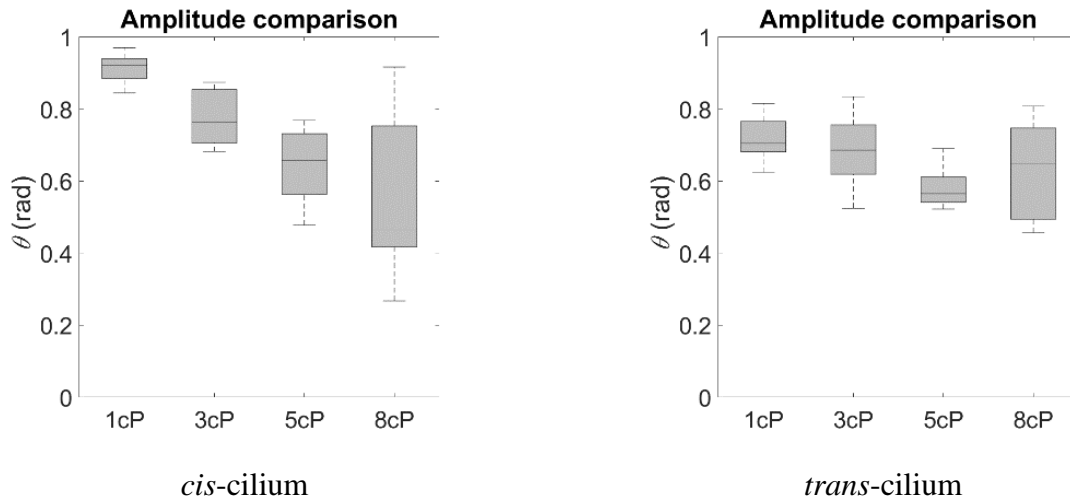


**Figure 4.11.** Amplitude comparison of the *cis*-cilium and *trans*-cilium groups. (a) *cis*-cilium and (b) *trans*-cilium.

The general trend of cilia curvature showed a decrease as the viscosity increased (see Figure 4.12). However, a slight increase in curvature was observed at 8cP for the *trans*-cilium. The curvature value here was not calculated by absolute value, which might explain why the result is different from previously reported results using *uni1*.<sup>190</sup>

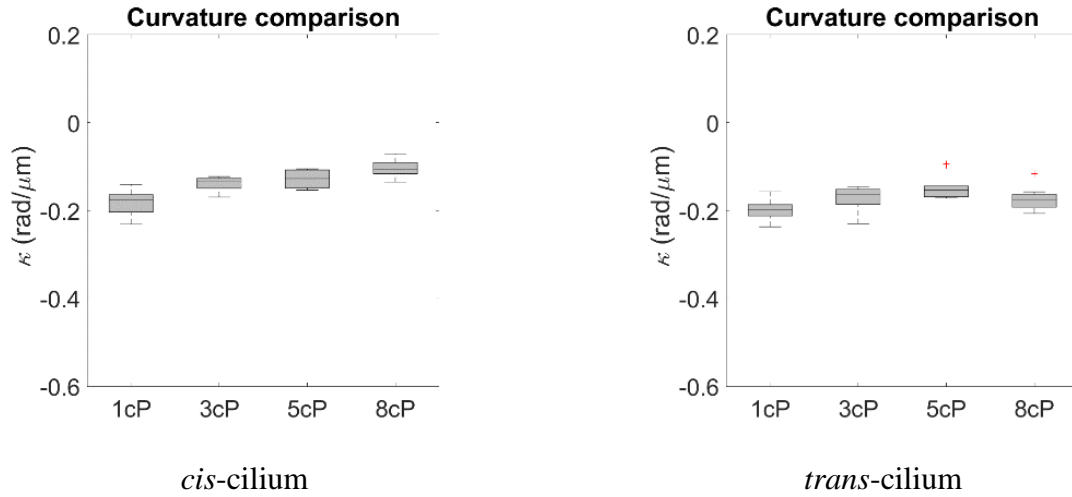


**Figure 4.12.** Curvature comparison of the *cis*-cilium and *trans*-cilium groups. (a) *cis*-cilium and (b) *trans*-cilium.

For different viscosities, the *trans*-cilium always has a higher beat frequency than the *cis*-cilium. However, the ratio of beat frequency of the *trans*-cilium over *cis*-cilium is increasing as the viscosity increases. This behavior is illustrated by the histogram plots in Figure 4.13. The asynchronization was more commonly seen and the ‘slip motion’ was more pronounced. Compare ‘one slip’ at the 1 cP case with up to ‘four slips’ maximum at 8 cP, which means that there were four beats in the *trans*-cilium when there was only one beat in the *cis*-cilium. It is likely that the high viscosity resulted in the increased difference between asymmetric forces generated by the *cis*- and *trans*- cilia. Beating patterns at such a high viscosities were less planar than at low viscosity conditions, which may also be due to the increased viscosity as the drag force on the cilium was increasing. For both types of cilia, the beating was also less periodic as the frequency increased.

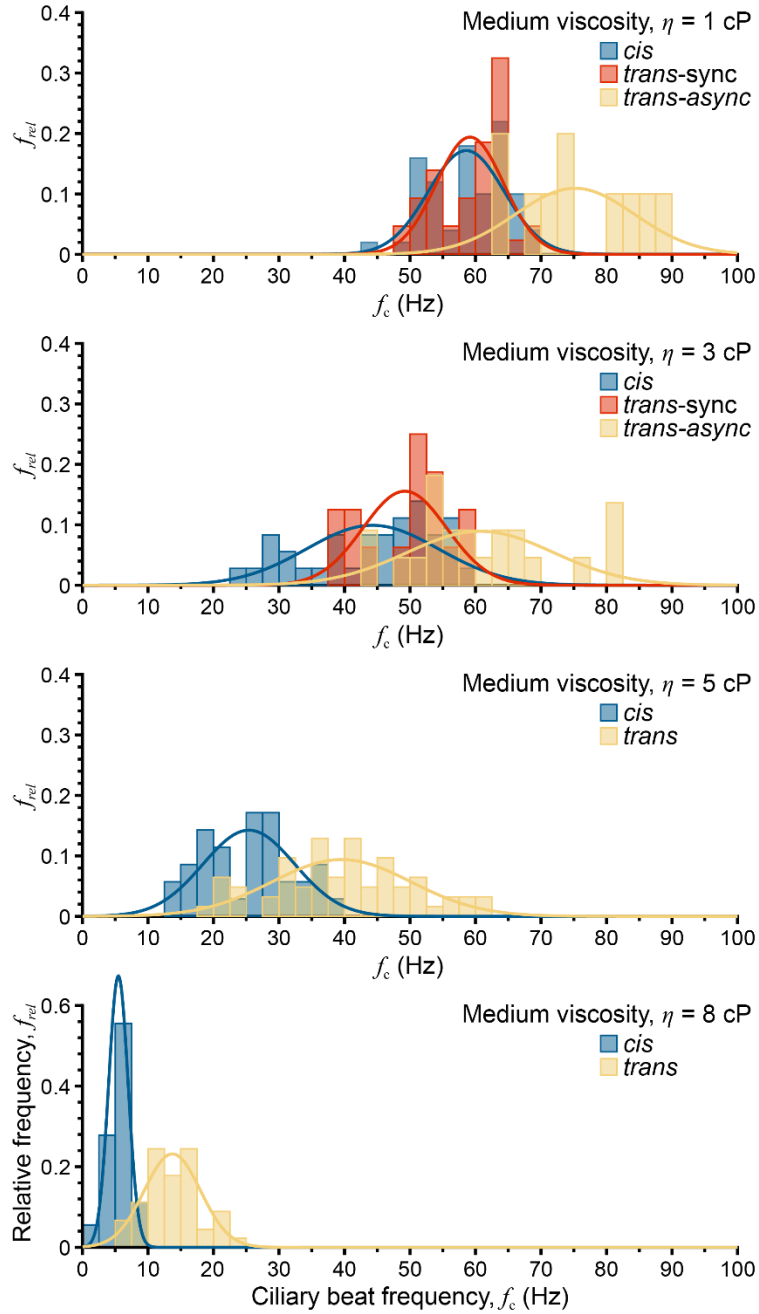


**Figure 4.13.** Histograms of response of cilia to varied fluid viscosity. The asynchronization appears to increase as viscosity increased. The trending of asynchrony to a high beat frequency ratio ( $f_{cis}/f_{trans}$ ) is clearly shown as viscosity increases.

In summary, *C. reinhardtii* cilia exhibit a reduced frequency, amplitude, and curvature as increased viscosity. However, *C. reinhardtii* behave differently at the highest viscosity tested in this study, which was also observed in our previous studies. It is thought that *C. reinhardtii* cells might adjust their waveform to reduce viscous loading, and revert to the slip motion in response to the mechanical stimulus. A more comprehensive study is needed regarding both engineering and biological aspects of these observations.

#### **4.3.4 Perturbation of Cilia Motion in Uniciliate *C. reinhardtii***

We further investigated the cilia response to changing mechanical stimuli. Here, uniciliated *uni1* cells were used. Diluted cell suspensions were first loaded into the fluidic chamber. The signal was turned on for 0.1 second using a customized code after the fluid movement stabilized. Due to the acoustic radiation force, cells were actively moved toward pressure nodes. Six cells with high translation speed (200–400  $\mu\text{m/s}$ ) were selected and analyzed here. During acoustically induced translation, three cells rotated faster, while the other three rotated slower than the rotation rate established before the translational movement. Examples of both cases are shown in Figure 4.14.

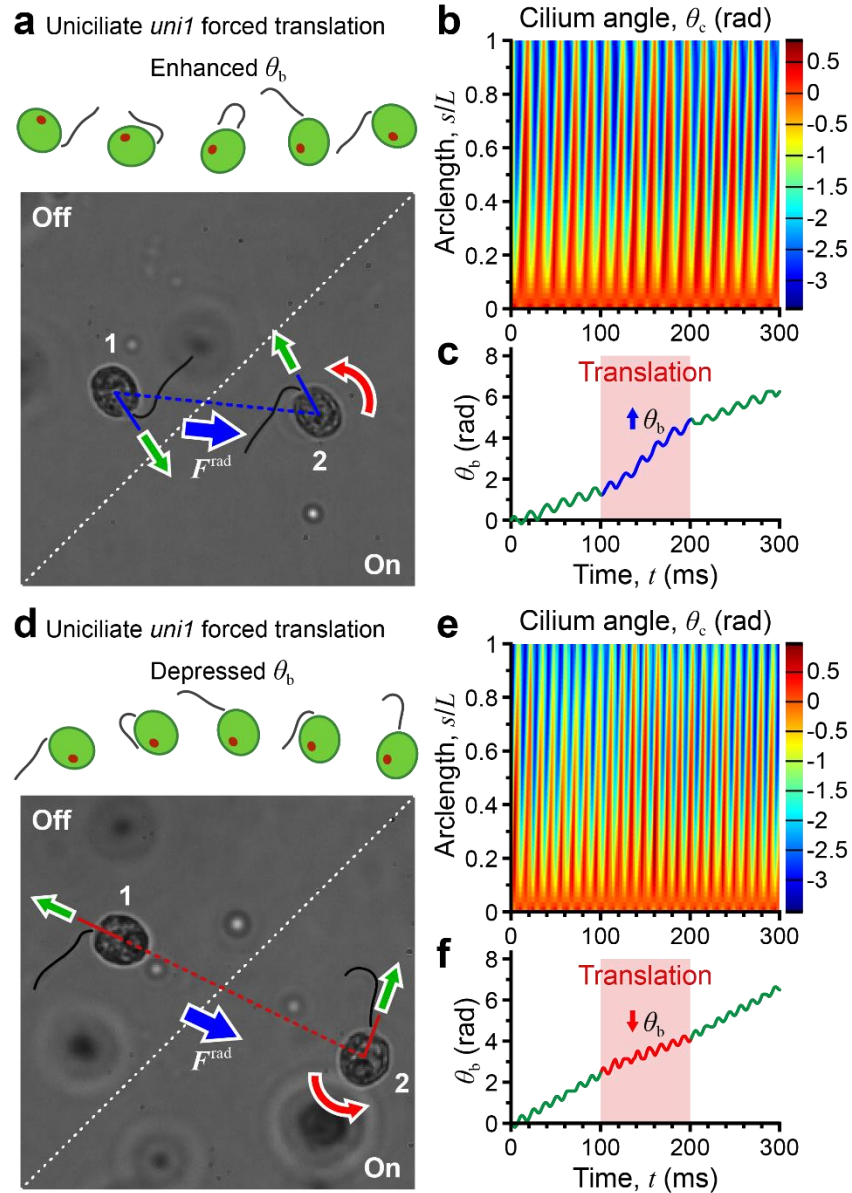


**Figure 4.14.** Examples of cell body rotation speed increasing with acoustically induced translation (a)-(c) and decreasing (d)-(f), respectively.

We first analyzed how the cell body rotation changes due to the perturbation. The rotation speed of four cells increased during the translational movement, while the other three decreased. Qualitative analysis revealed that the rotation speed change was related to the angle

change  $\theta_b$ , defined as the angle of cell moving direction at the proximal end to the cell body center. If the  $\theta_b$  tended to decrease during the translational movement, the rotation speed of the cells decreased because the cilia beating was compressed by hydrodynamic forces during the movement. However, the rotation speed of the cells increased as  $\theta_b$  increased during the movement. The trends of angle  $\theta_b$  indicated whether the cilium was assisted or inhibited by the translational movement. For all cases, the rotation speed recovered to the pre-perturbation state almost immediately after the translational movement, which indicates that the acoustics has no permanent effect on cell or cilia dynamics.

The torque estimated from cell body motion, which is proportional to angular rotation speed, increased as the cell rotation speed increased. A contrary situation happened for cells with decreasing rotation speed under acoustic perturbation: a general decrease of the torque on the cell body was expected. After the 0.1 second perturbation, the torque almost recovered to that of the pre-perturbation state. However, the torque values estimated from cilium motion, which is based on resistive theory, differed from the torque values estimated from cell body motion. Four out of six cells had higher values during perturbation compared to the ‘static’ state (pre- and post-translation), while the other two had no detectable change. This may be due to small errors in the assumed resistive force coefficients, which were estimated from a previous study.<sup>187</sup>

Although the torque on the cell body varied as the rotation speed varied, changes in frequency and waveform shape were negligible from the data analysis. However, detectable transitional changes in cilia bend angle were found from the cilium bend angle heat maps, shown in Figure 4.14. The hydrodynamic forces during the movement alter the cilia bending. Bend amplitude and curvature provide a limited description of cilium bending as the cilium basal angle is neglected.

In general, acoustically induced perturbations affect the cilia beating (cell body rotation, torque, and cilia bend angle) during the translational movement. The frequency and curvature changes were not negligible, but changes in the amplitude were not noticeable. After the perturbation, both the cilia and cell body movement recovered to the pre-perturbation state, indicating that the acoustically induced translation has no permanent effects on *C. reinhardtii*.

#### **4.3.5 Acoustic Effects on Cilia Beating**

In previous studies, we assumed that ultrasound exposure had no effect on cilia dynamics. We compared our results with previous studies of biciliated wild-type cells, finding very consistent and reasonable results.<sup>162</sup> However, it was still necessary to implement a method to compare the cilia dynamics of groups of cells with and without acoustic actuation.

The uniciliated *uni1* cells have been used for studying cilia dynamics because its rotational motion around the cell body enables long-term imaging and analysis. The ciliary waveform of uniciliated cells is similar to that of cilia of biciliated cells, although there are slightly variations between them.<sup>162, 191</sup> In addition, the biciliated cells are more difficult to study as they swim out of the high-magnification field of view without use of acoustic or other trapping approaches, which makes difficult comparison of the same group of cells with and without acoustic actuation. Thus, the uniciliated cells are ideal for investigation of acoustic effects on the same group of cells. Figure 4.15 shows an example of the same cell swimming without and with acoustics on.

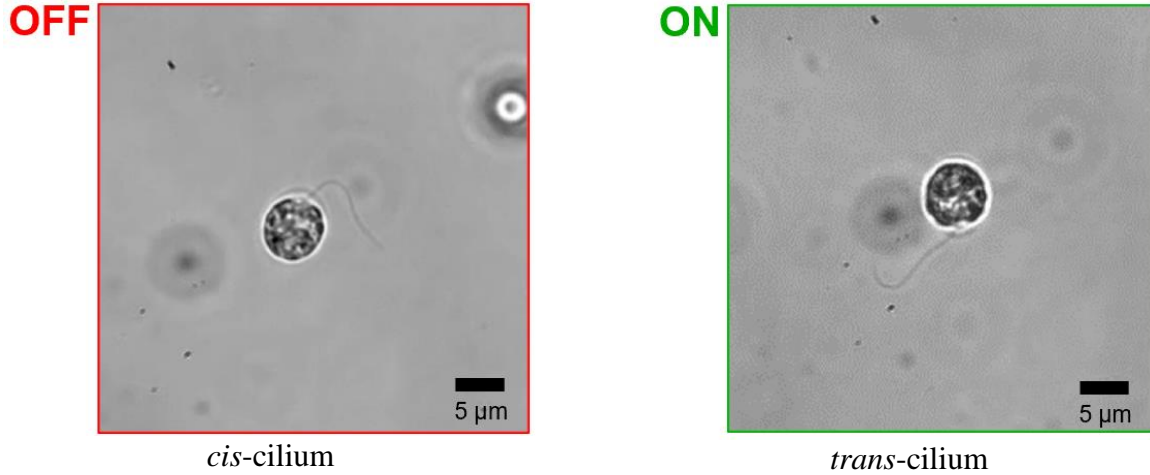


**Figure 4.15.** A uniciliated cell (*uni1*) that is rotating around its cell body (a) out of and (b) in an acoustic field.

To keep the experimental condition consistent for the single cell trapping study, the actuation frequency and power were kept the same as for the biciliated cell trapping work. A cell was first imaged in the condition without acoustics. Then the same cell was then imaged after movement to a pressure node with the acoustics on. The interval between the initiation of acoustics and imaging was 5–10 seconds. The cells ( $n=30$ ) were then analyzed using the methods developed throughout this thesis. The results are shown below in Figure 4.16.

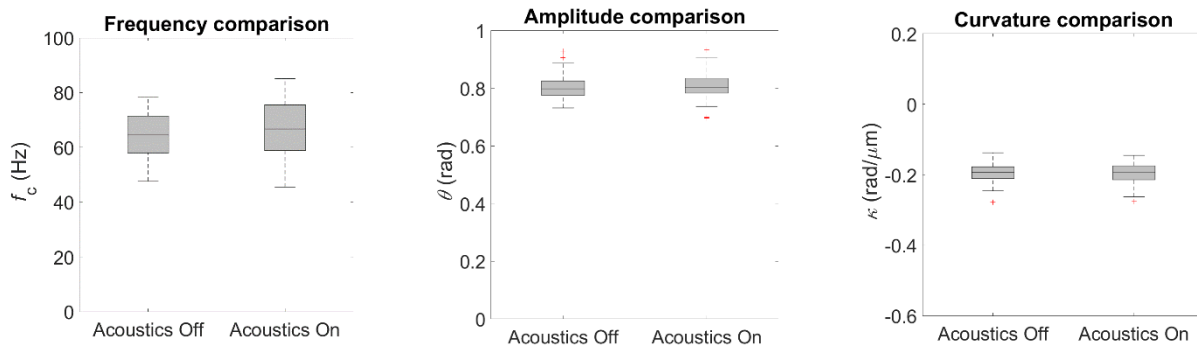


**Figure 4.16.** A uniciliated cell (*uni1*) that is rotating around its cell body (a) frequency comparison (b) amplitude comparison (c) curvature comparison.

Without the acoustic actuation, the uniciliated cells had a beat frequency around 64 Hz (mean  $\pm$  SD:  $64.00 \pm 9.14$  Hz). However, while in an acoustic field, the beat frequency increased

to 67 Hz (mean  $\pm$  SD:  $67.24 \pm 10.62$  Hz), which is slightly high. There is a significant difference between these two frequencies ( $p < 0.001$ ), showing that the acoustics appears to accelerate the beat frequency by  $\sim 4.7\%$ . The bend amplitude of unciliated cell cilia without and with acoustics had similar values, which were 0.82 rad (mean  $\pm$  SD:  $0.82 \pm 0.64$  rad) and 0.81 rad (mean  $\pm$  SD:  $0.81 \pm 0.72$  rad), respectively. In addition, the value of curvature changed little when cells were exposed to acoustics; the curvature under acoustics was  $-0.196$  rad/ $\mu\text{m}$  (mean  $\pm$  SD:  $-0.196 \pm 0.030$  rad/ $\mu\text{m}$ ) and without acoustics was  $-0.196$  rad/ $\mu\text{m}$  (mean  $\pm$  SD:  $-0.196 \pm 0.029$  rad/ $\mu\text{m}$ ). There was no significant difference with acoustics in either amplitude or curvature.

We assumed that the acoustics has a negligible effect on cilia beating because of the small length scale of the cilia ( $\sim 200$  nm comparing to hundreds of micron wavelength) and longer time scale (beat frequency 50–60 Hz comparing to MHz acoustic actuation). This study supported our hypothesis, especially regarding waveform shape (bend amplitude and curvature). There was only a small elevation in cilia beat frequency, and we believe that this increase was caused by the slight temperature rise due to heating induced by acoustic losses, which is discussed in next section.

#### **4.3.6 Temperature Effects on Cilia Beating**

In last section, we concluded that the cilia waveform is not affected by acoustic actuation, however, the cilia beat frequency increased about 5% at 20°C. The temperature effects on biological systems have been widely studied, and the thermal response of the physiological and biological traits have been summarized in the literature.<sup>193</sup>

Although several studies have shown and explained the thermal effects on the kinematics of microswimmers,<sup>154, 194-196</sup> the dynamic changes at the microscale level (e.g., cilia beat

frequency, bend amplitude, and curvature) on *C. reinhardtii* have not been investigated. Here, the novel acoustic tweezers were used to perform a detailed investigation of how temperature affects the cilia beating of *C. reinhardtii*. The selected method also gives insight into how the cilia dynamics change when *C. reinhardtii* are exposed to higher and lower temperatures for a period of 60 seconds. Three different temperatures were used, 15°C, 20°C, and 25°C, by setting the temperature control stage at the corresponding temperatures. The unciliated cells ( $n=6$ ) were placed in the microfluidic channel and exposed to acoustics for 60 seconds. Cilia dynamics were extracted and analyzed using the earlier-described method.

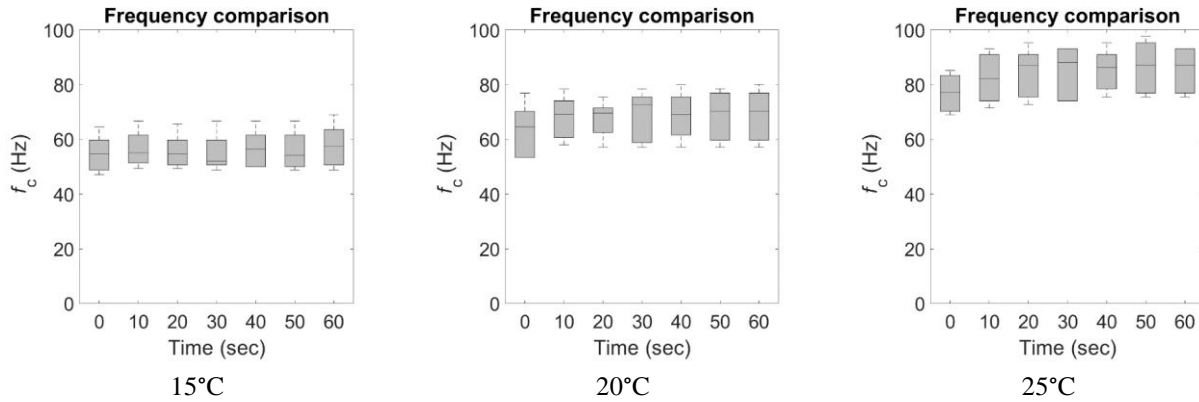


**Figure 4.17.** Unciliated cells (*uni1*) exposed to an acoustic field for 60 seconds at various setpoint temperatures. Median and interquartile ranges of frequency in the whole actuation period is shown.

Figure 4.17 shows the trend of the beat frequency of the unciliated cells over time with varying temperature. The initial condition indicates the cilia beating dynamics without acoustics. At 0 seconds (no acoustics) in 15°C case, the cilia had a beat frequency of about 55 Hz (mean  $\pm$  SD:  $54.92 \pm 7.04$  Hz). However, at 0 seconds (no acoustics) in the 20°C and 25°C cases, the cilia beat frequency is higher at 64 Hz (mean  $\pm$  SD:  $63.82 \pm 9.40$  Hz) and 77 Hz (mean  $\pm$  SD:  $76.94 \pm 6.85$  Hz), respectively, which shows the significant variation in beat frequency with temperature.

For the 15°C case, the beat frequency slightly varies over 60 seconds. At 60 seconds, the cilia had a slightly higher beat frequency of 57.79 Hz (mean  $\pm$  SD: 57.79  $\pm$  8.05 Hz). In the 20°C and 25°C cases, the cilia beat frequency again increased and stabilized within the first 5 seconds and 10 seconds, respectively, which indicates a temperature increase induced by the acoustics in these cases.

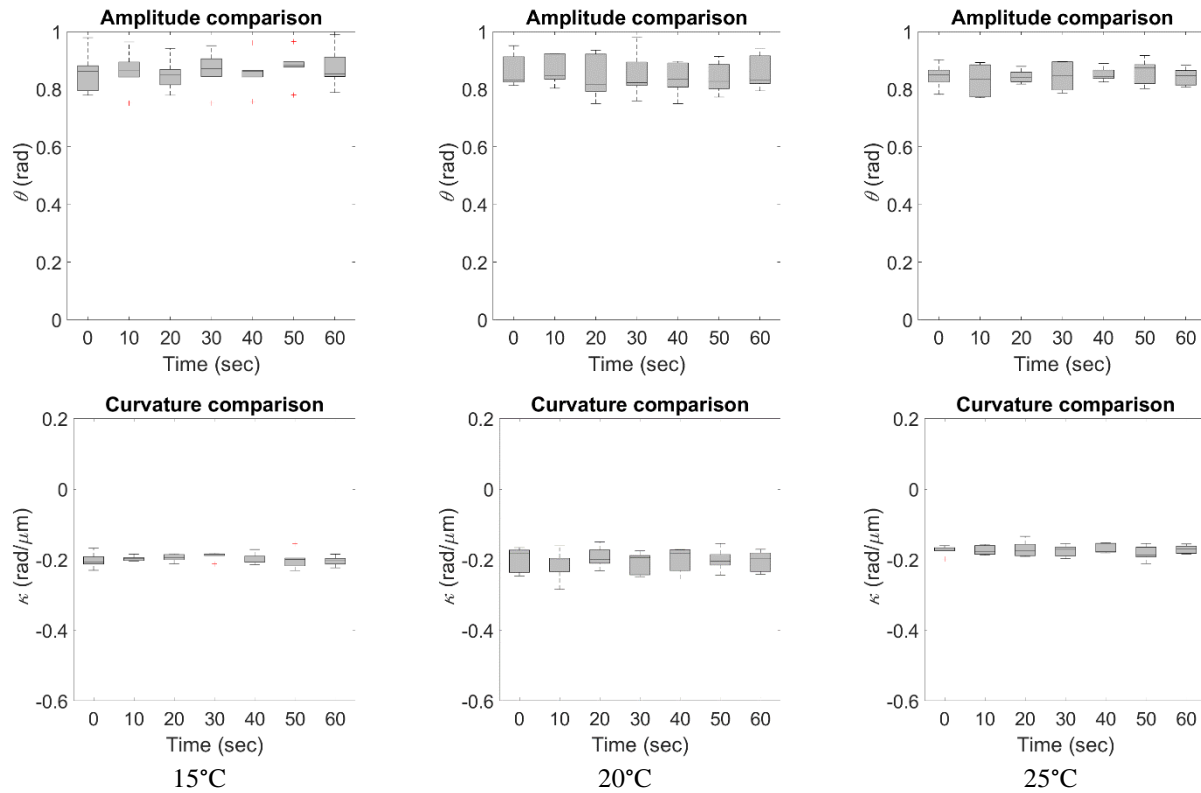


**Figure 4.18.** Waveform shape comparison (amplitude and curvature) for unciliated cells (*uni1*) exposed to an acoustic field for 60 seconds at various setpoint temperatures.

We then compared the waveform shape (bend amplitude and curvature) for all cases. For both parameters in all three cases, we chose 0 and 60 second studies as representative results to summarize, as they best illustrate the differences between the initial condition and that after prolonged exposure (0 seconds – no acoustics; 60 seconds – acoustic effects over a long time). For both bend amplitude and curvature at 15°C, 20°C, and 25°C cases, there is no significant

difference between 0 seconds and 60 seconds. A summary of parameters is shown in Table 4.1. This further supports our assertion that the acoustics has no effect on waveform shape. There is no significant difference in the waveform at 15°C and 20°C. However, at 25°C, the curvature has a relatively lower value of -0.17 rad/ $\mu\text{m}$  compared to -0.20 rad/ $\mu\text{m}$  for other cases. The reason might be that the beat frequency is high at up 85 Hz, which is out of the usually observed beat frequency range (50-80 Hz) of *C. reinhardtii* cells.

Table 4.1. Waveform shape parameters for different temperature cases

	Bend amplitude (mean $\pm$ SD rad)		Curvature (mean $\pm$ SD rad/ $\mu\text{m}$ )	
	0 second	60 second	0 second	60 second
15°C	0.86 $\pm$ 0.07	0.87 $\pm$ 0.07	-0.203 $\pm$ 0.021	-0.203 $\pm$ 0.014
20°C	0.86 $\pm$ 0.06	0.86 $\pm$ 0.06	-0.197 $\pm$ 0.035	-0.203 $\pm$ 0.029
25°C	0.85 $\pm$ 0.04	0.84 $\pm$ 0.03	-0.173 $\pm$ 0.014	-0.170 $\pm$ 0.012

This study is the first to extensively analyze the response of cilia dynamics to temperature only; the beat frequency of *C. reinhardtii* cilia increases with temperature. However, the waveform shape remains roughly the same, especially at temperatures lower than 25°C. The frequency increase when cells are exposed to acoustics in previous studies is attributed to a small temperature elevation due to acoustic losses, which is confirmed by this research.

### 4.3.7 Hybrid Acoustofluidic Systems for Manipulating Other Particles and Cells

The BAW/SAW systems are not only able trap microswimmers like *C. reinhardtii* but also passive particles as shown in Figure 4.19. Passive particles with positive acoustic contrast factor, such as deciliated *C. reinhardtii* cells, polystyrene beads, and SW620 tumor cells, are pushed to the pressure nodes where they can be confined. Thus, this novel acoustic technique is a

universal ‘acoustic tweezers’ that can be used to manipulate almost any type of particle or cell with negligible effects on physiological and biological aspects.

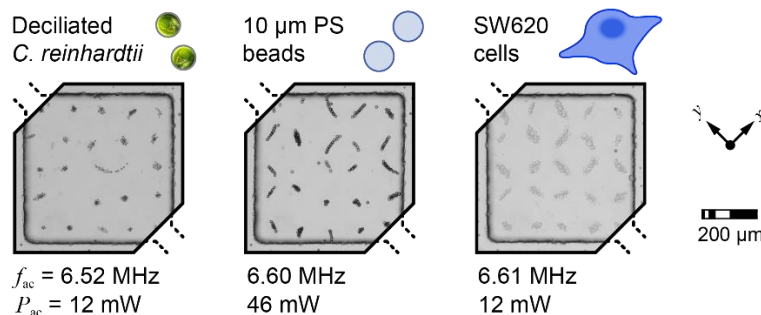


**Figure 4.19.** Passive particles trapping using BAW/SAW system at ~6.6 MHz

## 4.4 Conclusion

In summary, we have demonstrated a novel hybrid standing SAW\BAW acoustic tweezers that can manipulate microswimmers with high temporal and spatial resolution. These innovative acoustic tweezers have significant advantages in generating strong trapping forces while maintaining biocompatibility. The BAW\SAW system breaks the low frequency limitation of traditional BAW systems which are actuated by bulk piezoelectric ceramics and the typically low acoustic radiation forces of traditional SAW systems that manipulate particles in PDMS channels. The novel acoustic tweezers allow trapping multiple particles and biological samples, including microswimmers such as *C. reinhardtii* that require higher trapping forces without excessive heating. Further modification of the acoustic tweezers allows high-throughput, high temporal, and high spatial resolution observation of the dynamics of nanometer scale organelles, such as the cilia studied in this work. Applying this non-contact, robust acoustic tweezers to *C. reinhardtii* cells initiated new research into cilia dynamics, such as quantitative study of 3D helical motion and cilia dynamics in response to mechanical perturbation in our work. This method can also be modified to fulfill other potential applications in cilia research, such as

transient observation of the chemical response of cilia and cilia regrowth. Due to their universality, our acoustic tweezers have other potential applications in biology, biomedical engineering, and physics. The SW620 cell trapping work implies that our acoustic tweezers can be used to assemble organoids/spheroids. The deciliated cell trapping work shows the potential of this technology for *in vitro* observation of cilia growth.

# **Chapter 5: Optimization and Pressure Mapping of BAW/SAW devices**

In the last chapter, a full study of cell and cilia motion was performed with assistance of the BAW/SAW hybrid systems. The hybrid glass-based BAW/SAW devices enabled imaging and study of cilia dynamics in both periodic and non-periodic beating. In addition, helical motion was quantified using this technique. Finally, the cilia response to viscosity change and acoustic-induced translation were fully investigated.

Although the BAW/SAW devices have been proven as a robust acoustofluidic method, the characterization of the pressure field has not yet been completed. In addition, the rounded side walls created using isotropic glass wet etching were found to disturb the acoustic pressure field inside of the microfluidic channels. To address these two problems, here the BAW/SAW device geometry is optimized by replacing glass with silicon, and pressure mapping of BAW/SAW devices is performed using established methods.<sup>124, 197</sup>

## **5.1 Introduction**

The BAW/SAW devices have been proven as a robust and efficient acoustofluidic method that allows single microswimmer-per-well trapping and high-resolution imaging of cilia motion. However, the performance of glass-based SAW devices at high frequencies is not ideal because of the isotropic etching effect on wet-etched glass. The rounded edges of the glass channel wall affect the acoustic field formed inside of microfluidic channels (see Figure 4.2-c and d), which hinders the diamond channels from forming the desired 7x7 matrix. The device efficiency is also reduced compared to silicon microfluidic devices as reported by Evander et al.<sup>128</sup> We propose a novel device that addresses the numerous shortcomings mentioned above.

This new BAW/SAW device has vertical silicon side walls and a thin glass (~175  $\mu\text{m}$ ) cover, yielding a uniform pattern of pressure nodes for trapping populations of cells or for single cell-per-well trapping when dilute cell suspensions are used.

The translation of acoustofluidics to clinical and industrial use has been hindered due to inconsistency and poor reproducibility. Computational modeling shows great advantages for predicting device performance (e.g., acoustic pressure, energy density, etc.).<sup>198</sup> However, even state-of-the-art models are not able to account for inconsistencies in material properties, geometric tolerances, and ill-defined component interfaces. Tracing the motion of passive particles is a common way to determine the acoustic pressure amplitude in experimental work, and various experimental methods to characterize acoustofluidic devices have been developed.<sup>104, 199-205</sup> However, these approaches are typically limited to simple geometries or require complex experimental setups and equipment. In addition, the existing methods are time-consuming because a series of load-and-replace experiments is needed to quantify system performance. Finally, it is impossible to monitor the acoustofluidic device performance continuously because the passive particles cannot redistribute after moving to pressure minima (or maxima) in each experiment. Our group has established a new method that uses an active measurement probe the *C. reinhardtii* algae, which addresses the multiple shortcomings mentioned above.<sup>124</sup> Here this method is used to characterize the glass based BAW/SAW devices introduced in Section 4.3.

## **5.2 Optimization of BAW/SAW Devices**

In order to create uniform cell patterns while accommodating high-resolution cilia imaging using transmitted light microscopy, the side walls of the acoustofluidic channel/chamber should be

made of silicon, with the top sealing surface being made of thin glass. The fabrication process for such a device is illustrated in Figure 5.1.

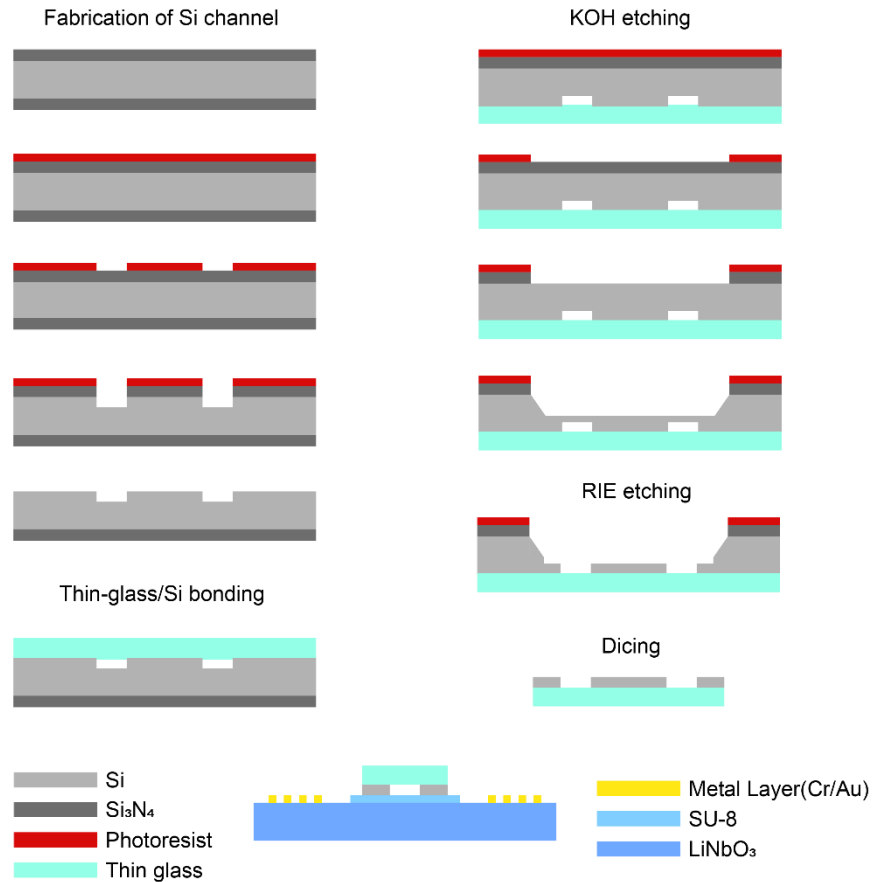


**Figure 5.1.** Fabrication process of thin glass/Si BAW/SAW devices. An Si wafer with  $\text{Si}_3\text{N}_4$  on both sides was used to fabricate acoustofluidic channels. After etching the microfluidic channels using DRIE,  $\text{Si}_3\text{N}_4$  was removed from one side using RIE, and the Si wafer was anodically bonded with thin glass (~175  $\mu\text{m}$  thick). The other side of the Si wafer was first wet etched to a depth that was near to the designed channel height. Then, the bottoms of the Si channels were etched through by RIE. The thin-Si/glass channels were then bonded to the SAW substrate using the previously described method from Chapter 2.

A silicon wafer (~500  $\mu\text{m}$ ) with silicon nitride ( $\text{Si}_3\text{N}_4$ ) on both sides was used to fabricate the microfluidic channels. A layer of photoresist was spin-coated on one side of wafer, followed by standard laser writing and development processes. DRIE was used to etch the channel pattern

to a depth of  $\sim 30\ \mu\text{m}$ , which is slightly deeper than the desired final channel depth of  $\sim 25\ \mu\text{m}$ . After removing the  $\text{Si}_3\text{N}_4$  on the side where the microfluidic channels were etched, the Si wafer was anodically bonded to a thin glass wafer. The other side of the wafer was wet etched in KOH instead of using DRIE directly after removal of  $\text{Si}_3\text{N}_4$ , because the KOH etch yields a smoother surface than RIE etching. This KOH etch depth was roughly  $400\ \mu\text{m}$ . Then, the wafer was diced and mounted to a carrier wafer to avoid breaking the thin sample. Next, the silicon over the microchannels was etched through carefully, yielding a channel depth of  $25\ \mu\text{m}$ . After bonding the channels to the  $\text{LiNbO}_3$  substrate with IDTs using SU-8 as an adhesive layer, the devices were ready to be tested (see Figure 5.2).

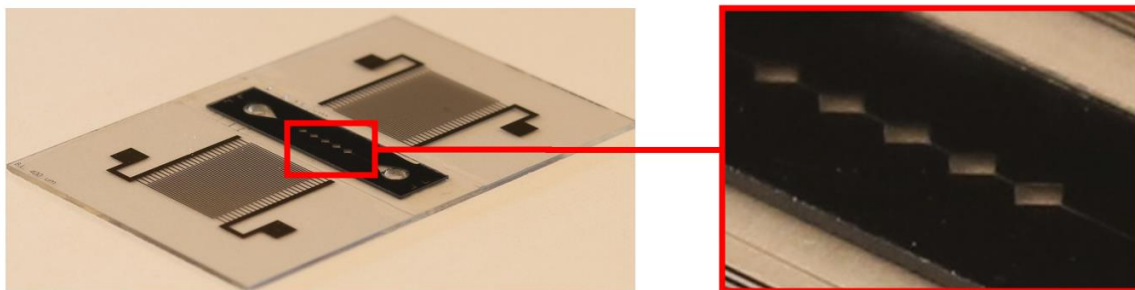


**Figure 5.2.** The thin-Si/glass diamond channel on  $\text{LiNbO}_3$  with IDTs. The channel walls are made of silicon that is  $25\ \mu\text{m}$  thick. The channel top is sealed by thin glass ( $\sim 175\ \mu\text{m}$ ), which allows for oil-immersion microscopy.

The channel was flushed with isopropyl alcohol to avoid air bubbles and then pretreated with 3% (w/V) BSA in PBS for ten minutes to avoid cell attachment before loading wild-type *C. reinhardtii* into the microfluidic chamber. Two devices for operating at  $\sim 10\ \text{MHz}$  and  $\sim 20\ \text{MHz}$  (corresponding to  $200\ \mu\text{m}$  and  $400\ \mu\text{m}$  SAW wavelengths, respectively) were tested. The side lengths of the two diamond chambers were  $545\ \mu\text{m}$  and  $270\ \mu\text{m}$  respectively, which were expected to form  $7 \times 7$  matrices. By adjusting the frequency and power, the  $10\ \text{MHz}$  device and  $20\ \text{MHz}$  device formed uniform  $8 \times 8$  matrices, as shown in Figure 5.3. Both devices did not form a  $7 \times 7$  matrix as expected, but that might have been due to the resonance mismatch

between BAWs and SAWs. However, the input power needed to pattern the cells was small compared to the glass-based devices described earlier, only 47 mW and 65 mW, respectively. In addition, the thin-Si/glass devices showed more uniform patterns compared to thin-glass BAW/SAW devices.

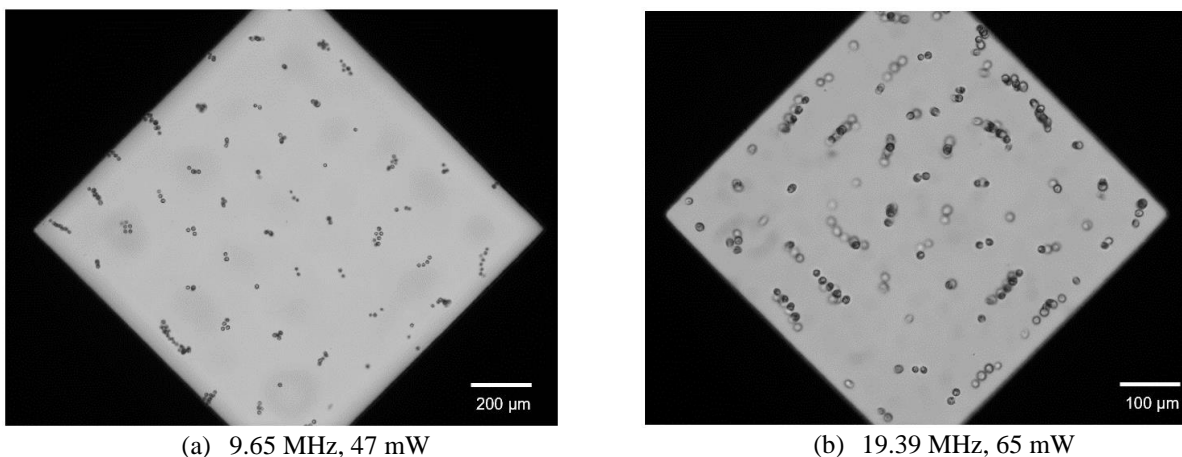


**Figure 5.3.** The acoustic cell patterning to form 8 x 8 matrices in (a) 10 MHz and (b) 20 MHz thin Si/glass BAW/SAW devices. The input power that drives the IDTs was lower compared to that needed for the previously described thin-glass BAW/SAW devices. In addition, the patterns are more uniform.

This presented fabrication technique allows user-controlled channel depths for very thin silicon layers, as the thinnest commercially available Si wafers are  $\sim 50 \mu\text{m}$  thick. In addition, the two-dimensional BAW pressure field formed by the one-dimensional SAW is more uniform because the silicon microfluidic channel walls are precisely fabricated using the deep reactive ion etching process. The device efficiency is improved due to the precisely fabricated channel side walls. Finally, our initial results using Si/glass devices to characterize ciliary waveform suggest that the newly fabricated channels have no effect on cilia dynamics. These advantages make this new device type a promising tool for future acoustofluidics research.

### 5.3 Pressure Mapping of Glass-Based SAW Devices

The pressure mapping work described here was performed using a previously described method established by our lab.<sup>124</sup> Here, only initial results are provided for a 6 MHz glass-based SAW device (corresponding to 600  $\mu\text{m}$  SAW wavelength) with a straight fluidic channel. The channel had a depth of 50  $\mu\text{m}$  and a width of 545  $\mu\text{m}$ . Five nodal lines were expected within this channel size when driven at the resonance of the IDTs.

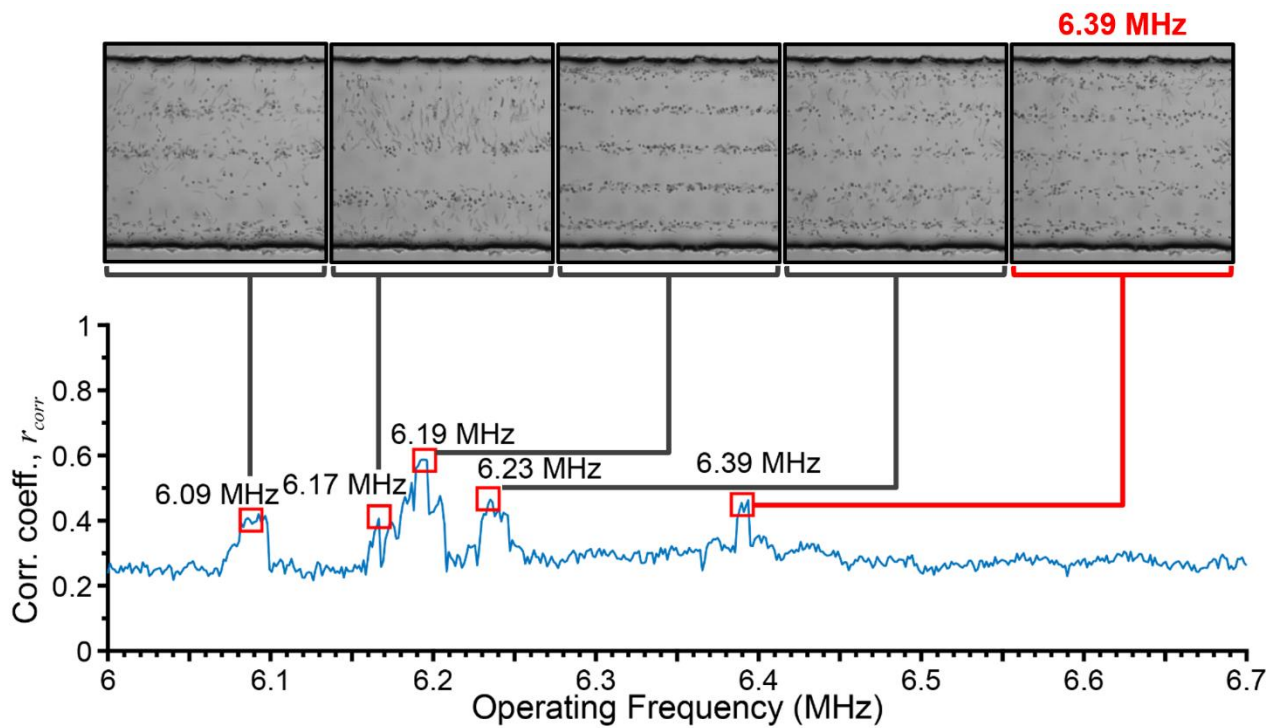


**Figure 5.4.** Resonance identification for glass-based SAW device with a straight fluidic channel. The five images at the top show cell distributions at peaks of the correlation coefficient, which can be easily identified as resonant frequencies.

Automatic identification of device resonant frequencies was done by sweeping the frequency from 6 MHz to 6.7 MHz. The actuation time for each frequency was held for 1.5 s with output power held constant by adjusting the waveform generator input voltage via Python. For the pressure amplitude mapping, the frequency was held constant while increase the voltage

at a  $\sim 2.3 V_{pp}$  increment. Actuation was held for 5 s at each voltage step with a 5 s signal off interval. The correlation coefficient of successive images (*corr2* function in MATLAB) was used to identify the resonances of a device. A high correlation coefficient represents high similarity of two images. The cells were confined to pressure minima at resonance so the cell distribution was relatively unchanged, and thus, the correlation coefficient was high. The experiments for each study were repeated five times. Here, one case is used to demonstrate the principle of this work.

After loading the cells into the channel, frequency was swept from 6 MHz to 6.7 MHz with an increment of 10 kHz. The output power was fixed at 200 mW throughout. The correlation coefficient is plotted in Figure 5.4. Resonant frequencies were identified as peaks of correlation coefficient at 6.07 MHz, 6.17 MHz, 6.19 MHz, 6.23 MHz, and 6.39 MHz. Between these resonant frequencies, the *C. reinhardtii* cells were evenly distributed in the channel. The peak at 6.19 MHz was the highest, which suggested that the tightest nodal lines were found at this frequency. However, the nodal lines at this frequency were not quite symmetric about the centerline of the microfluidic channel. The top nodal line was closer to the channel wall than the bottom one. In addition, the impedance was measured to be  $\sim 90 \Omega$ , which means that the efficiency of the SAW was lower than those frequencies with an impedance of  $50 \Omega$ . Finally, the input power was about three times higher than that at the other four operating frequencies. The 6.07 MHz, 6.17 MHz, and 6.23 MHz patterns did not show a uniform distribution of cells. Thus, the 6.39 MHz frequency was identified as the optimal resonance of the BAW/SAW device because of its uniform cell distribution, desired impedance, and high transmission efficiency of the SAW. This demonstrates that the image correlation coefficient can be used to determine the optimal operating frequencies for the glass-based SAW devices.

The pressure field amplitude was characterized using a voltage sweep at the fifth half-wavelength resonance of the straight channel at 6.39 MHz. The voltage was linearly increased from 0 V<sub>pp</sub> to 11.3 V<sub>pp</sub> with an increment of ~2.25 V<sub>pp</sub>. Figure 5.5 shows the analyzed results of normalized acoustic potential  $\tilde{U}(y)$ , brightfield images, heat maps reflecting the cell distribution density, and line plots of summed cell distribution density  $\bar{\Lambda}(y)$ .

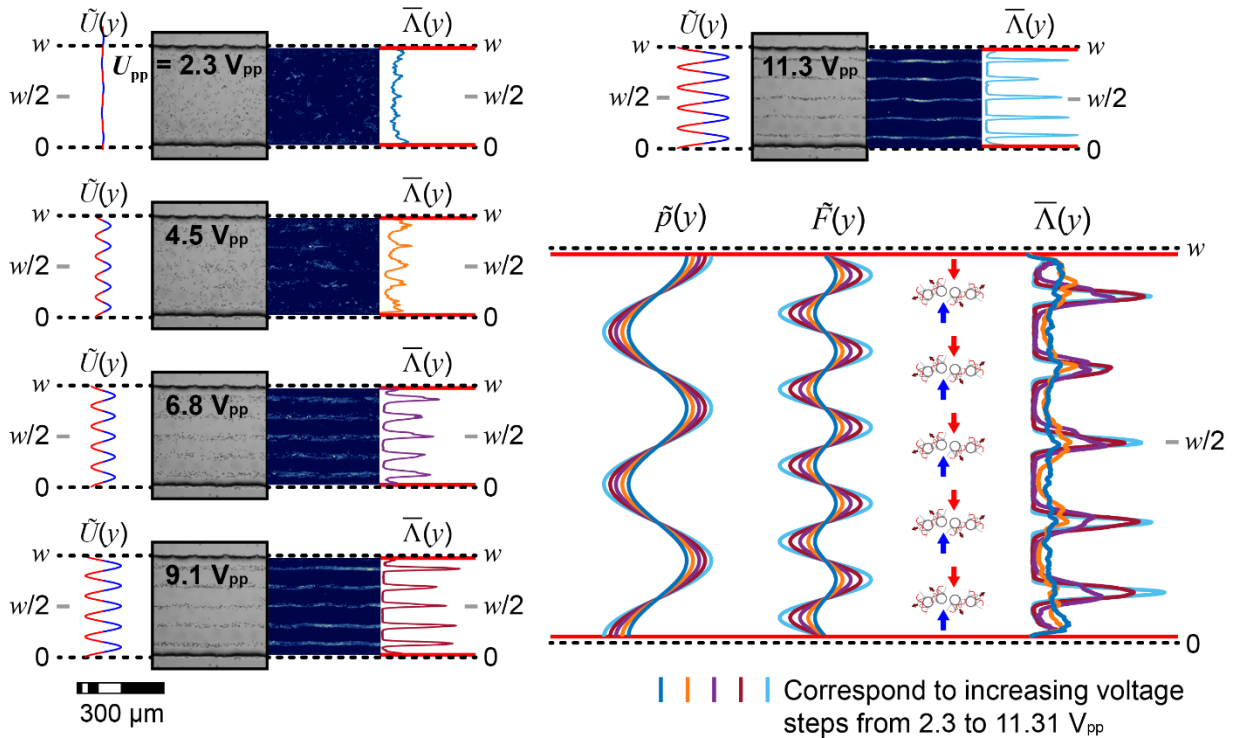


**Figure 5.5.** Qualitative mapping of the acoustic field amplitude for the fifth half-wavelength resonance of the glass-based SAW device with a straight channel. Acoustic potential, brightfield images, heat maps of the cell distribution density, and line plots of cell distribution density summed along the channel length with increasing voltage. The pressure, the acoustic radiation force, and normalized cell distribution density are shown on the bottom-right.

At lower voltages, cells were freely swimming in the microfluidic channel because of the relatively lower trapping force. After exceeding a threshold voltage of ~4.5 V<sub>pp</sub>, the cells became confined to five horizontal nodal lines. As the voltage further increased, cells more tightly aggregated to the pressure nodal lines, while the cell distribution density formed tighter and

higher peaks. From the voltage sweep, we can see that cell confinement is a function of voltage amplitude. In addition, the acoustic radiation force was zero at pressure nodal lines, and the cells could not swim strongly enough to overcome the acoustic trap that bounded by a threshold radiation force when the applied voltage goes high. The image correlation coefficient can be used to identify the resonances of glass-based SAW devices. Further, cell confinement is voltage dependent.

## **5.4 Summary**

The glass-based BAW/SAW devices have been established as a promising tool in multiple applications. To improve the performance of this new technology, we developed a fabrication process that enables thin-Si/glass microchannel construction. This channel has vertical channel side walls with precisely prescribed geometry. The thin glass layer that encloses the silicon channel also allows visual access and transmitted light microscopy (including oil-immersion microscopy) for high resolution imaging of trapped cells and cilia motion.

In addition, using our established method, the resonances of a glass-based BAW/SAW device were automatically assessed, including qualitative mapping of the acoustic field amplitude variation with drive voltage. A one-dimensional geometry (a straight channel) was used as an example in this work; however, the method can easily be extended to two dimensional geometries (e.g., a circular chamber).

## **Chapter 6: Conclusion**

Here, I summarize contributions of my PhD project carried out using a novel acoustic trapping technique to exhaustively study *C. reinhardtii* cells and their cilia motion. I also provide some limitations of this work, including the technique itself, post-processing tools, and practical considerations for solving biological and biomedical problems. Future directions and potential improvements are also discussed. Lastly, I briefly offer my thoughts on the entirety of my PhD work, including contributions outside of the primary PhD project.

### **6.1 Summary of Work**

There are two primary disparate fields of work presented in this thesis: The entirety of the development of an acoustic tweezers comprising two-dimensional bulk acoustic waves driven by one-dimensional surface acoustic waves, and analyzing swimming *C. reinhardtii* and cilia motion while cells are trapped in the acoustic field enabled by our novel acoustofluidic technique.

BAW and SAW seem like two unrelated techniques, and each has its advantages and disadvantages. This thesis work connected these two ‘distinct’ acoustofluidic techniques and developed a robust experimental tool in the process. This acoustofluidic technique can generate strong trapping forces, while allowing high-resolution imaging with high biocompatibility. It also potentially allows transient observation under continuous flow conditions. By modifying and implementing this technique in cilia motion research of *C. reinhardtii*, waveform analysis was done, followed by analysis of 3D helical swimming, cilia motion response to a changing mechanical environment, and perturbation induced by acoustics. Most of these studies cannot be

done using traditional micropipette-based trapping techniques as they require hard contact and suffer from low-throughput.

The presented work lays the foundation for cilia motion research using this novel acoustofluidic technique. Cilia motion research can be greatly expanded using this method, especially regarding the topics of 3D helical motion and transient response to external stimuli, which have not been fully addressed or fully understood. This technique has great potential, but there is significant room for future improvement.

## **6.2 Limitations, and Future Directions**

In this section, I discuss the limitations of our novel acoustic tweezers, post-processing techniques, and practical aspects of research in biomedicine and biology. Then, I discuss potential improvements and future directions of the thesis-related research. I conclude with my final thoughts on my PhD career.

The BAW/SAW system that I developed is not yet able to control object manipulation as precisely as PDMS-based SAW, which can move passive particles to desired positions. The technique also requires researchers to have access to good fabrication facilities including a cleanroom and associated microfabrication tools. I believe that high-frequency BAW/SAW devices will push acoustofluidic manipulation to micron scale precision. However, I was unable to investigate this possibility due to facility limitations to be addressed in the future.

Cilia motion research should be accelerated by use of our acoustofluidic technique, but the technique is not easily implemented in a cilia research lab, especially without collaboration with an acoustofluidics lab. The waveform analysis (2D) is extracted from in-plane motion of acoustically trapped *C. reinhardtii* cells. Since the cilia motion is slightly out-of-plane, the in-

plane motion analysis provides only an estimate of parameters. Of course, this is also an advantage as the acoustofluidic technique enables characterization of the 3D helical motion due to the asymmetry of forces generated by the two nearly identical cilia. The ability to analyze helical motion is important for studying this ubiquitous movement modality used by motile cells for environmental sensing. Regardless, a better imaging system or strategy may be needed to push these studies forward. For the viscosity dependence study, the solution we added (Ficoll) to increase viscosity also increased the density of the fluid, and thus, the acoustic properties changed, making it difficult to identify an optimal focusing frequency at 8 cP. The acoustic perturbation experiment was also difficult, as the cilia can be out of plane so that only cases with cilia that were in-plane could be used. The cilium cannot be treated as a single beam and solved as a traditional beam mechanics problem. This also shows that the field of biomechanics/mechanobiology has many unanswered or unexplored questions. However, to address this, future work can focus on manipulation of mutant cells, from which specific proteins have been removed. This would allow us to look at one specific impact of all possible assumptions discussed before (calcium concentration, hydrodynamic interaction, etc.). Moreover, although the streaming effects were considered negligible, if higher power is needed for future studies, streaming might start to effect the cell motion.

I began working on cilia motion analysis one year ago, and I remain fascinated by these small strong swimmers. Later in my PhD program, I was given the opportunity to work on additional projects that related to biomedical engineering: acoustic assembly of spheroids, tumor-on-a-chip devices, separation of circulating tumor cells from whole blood using longitudinal standing bulk acoustic wave devices, exosome separation and enrichment, and assisting in measurement of viscoelastic properties of 3T3 cells using an acoustic method. I interacted with

many biomedical and clinical collaborators, and I found there exists a substantial gap between engineering and biomedicine or biology. Researchers in these two disparate fields continue to think differently, and sometimes interdisciplinary communication is less effective due to this difference. Hopefully, by taking on both types of research activities and merging the two ways of thinking, I can help move both fields forward at an accelerated rate. This has been my motivation for not only focusing on device engineering but also on learning and gaining experience in biomedicine and biology.

### **6.3 Final Thoughts**

My lifelong aim in academia is to become a person that can bridge the gap between biology and engineering, while solving the most challenging engineering and biomedical issues. Outside of the laboratory, I aim to become an influential figure in academia who promotes equity and collaboration in education, and science and technology nationwide or even worldwide. No matter what fields I work in, I will always try to become one of the best researchers in those fields.

I have been thinking about the meaning of life after the loss of my cousin this summer. I realized that perfect is impossible, especially in research, although perfection is what I pursue. However, if a problem is ‘perfectly’ solved, there is no need to continue researching this problem anymore. I have not found any perfect research in my life through my own work or in studying the work of others, and I hope to give those who read this thesis some advice in their career and in life. Do your best, but do not push yourself too hard. When you think you cannot go further, take a break, and always remember there are good things in life.

Dream big, see further, and work hard – be the best of the best.

## References

1. Whitesides, G.M. The origins and the future of microfluidics. *Nature* **442**, 368-373 (2006).
2. Sackmann, E.K., Fulton, A.L. & Beebe, D.J. The present and future role of microfluidics in biomedical research. *Nature* **507**, 181-189 (2014).
3. Dittrich, P.S. & Manz, A. Lab-on-a-chip: microfluidics in drug discovery. *Nature reviews Drug discovery* **5**, 210-218 (2006).
4. Weiss, M. et al. Sequential bottom-up assembly of mechanically stabilized synthetic cells by microfluidics. *Nat. Mater.* **17**, 89 (2018).
5. Zilionis, R. et al. Single-cell barcoding and sequencing using droplet microfluidics. *Nat. Protoc.* **12**, 44 (2017).
6. Di Carlo, D., Aghdam, N. & Lee, L.P. Single-cell enzyme concentrations, kinetics, and inhibition analysis using high-density hydrodynamic cell isolation arrays. *Anal. Chem.* **78**, 4925-4930 (2006).
7. Di Carlo, D., Irimia, D., Tompkins, R.G. & Toner, M. Continuous inertial focusing, ordering, and separation of particles in microchannels. *Proceedings of the National Academy of Sciences* **104**, 18892-18897 (2007).
8. Chung, K., Rivet, C.A., Kemp, M.L. & Lu, H. Imaging single-cell signaling dynamics with a deterministic high-density single-cell trap array. *Anal. Chem.* **83**, 7044-7052 (2011).
9. Hou, H.W. et al. Isolation and retrieval of circulating tumor cells using centrifugal forces. *Sci. Rep.* **3**, 1259 (2013).
10. Freer, E.M., Grachev, O., Duan, X., Martin, S. & Stumbo, D.P. High-yield self-limiting single-nanowire assembly with dielectrophoresis. *Nat. Nanotechnol.* **5**, 525 (2010).
11. Vahey, M.D. & Voldman, J. An equilibrium method for continuous-flow cell sorting using dielectrophoresis. *Anal. Chem.* **80**, 3135-3143 (2008).
12. Song, H. et al. Continuous-flow sorting of stem cells and differentiation products based on dielectrophoresis. *Lab Chip* **15**, 1320-1328 (2015).
13. Lim, B. et al. Magnetophoretic circuits for digital control of single particles and cells. *Nat. Commun.* **5**, 3846 (2014).
14. Pamme, N. & Wilhelm, C. Continuous sorting of magnetic cells via on-chip free-flow magnetophoresis. *Lab Chip* **6**, 974-980 (2006).
15. Kim, S. et al. Circulating tumor cell microseparator based on lateral magnetophoresis and immunomagnetic nanobeads. *Anal. Chem.* **85**, 2779-2786 (2013).
16. MacDonald, M.P., Spalding, G.C. & Dholakia, K. Microfluidic sorting in an optical lattice. *Nature* **426**, 421 (2003).
17. Wang, X. et al. Enhanced cell sorting and manipulation with combined optical tweezer and microfluidic chip technologies. *Lab Chip* **11**, 3656-3662 (2011).
18. Riaud, A., Baudoin, M., Matar, O.B., Becerra, L. & Thomas, J.-L. Selective manipulation of microscopic particles with precursor swirling Rayleigh waves. *Phys. Rev. Appl.* **7**, 024007 (2017).
19. Ding, X. et al. On-chip manipulation of single microparticles, cells, and organisms using surface acoustic waves. *Proc. Natl. Acad. Sci. U. S. A.* **109**, 11105-11109 (2012).

20. Petersson, F., Åberg, L., Swärd-Nilsson, A.-M. & Laurell, T. Free flow acoustophoresis: microfluidic-based mode of particle and cell separation. *Anal. Chem.* **79**, 5117-5123 (2007).
21. Warkiani, M.E. et al. Slanted spiral microfluidics for the ultra-fast, label-free isolation of circulating tumor cells. *Lab on a Chip* **14**, 128-137 (2014).
22. Warkiani, M.E. et al. Ultra-fast, label-free isolation of circulating tumor cells from blood using spiral microfluidics. *Nat. Protoc.* **11**, 134 (2016).
23. Zhang, J. et al. Fundamentals and applications of inertial microfluidics: A review. *Lab on a Chip* **16**, 10-34 (2016).
24. Ahn, K. et al. Dielectrophoretic manipulation of drops for high-speed microfluidic sorting devices. *Applied Physics Letters* **88**, 024104 (2006).
25. Pommer, M.S. et al. Dielectrophoretic separation of platelets from diluted whole blood in microfluidic channels. *Electrophoresis* **29**, 1213-1218 (2008).
26. Voldman, J. Electrical forces for microscale cell manipulation. *Annu. Rev. Biomed. Eng.* **8**, 425-454 (2006).
27. Pethig, R. Dielectrophoresis: Status of the theory, technology, and applications. *Biomicrofluidics* **4**, 022811 (2010).
28. Ouyang, W. & Han, J. Universal amplification-free molecular diagnostics by billion-fold hierarchical nanofluidic concentration. *Proceedings of the National Academy of Sciences* **116**, 16240-16249 (2019).
29. Wan, Y. et al. Rapid magnetic isolation of extracellular vesicles via lipid-based nanoprobe. *Nature biomedical engineering* **1**, 1-11 (2017).
30. Hejazian, M. & Nguyen, N.-T. Negative magnetophoresis in diluted ferrofluid flow. *Lab Chip* **15**, 2998-3005 (2015).
31. Nguyen, N.-T. Micro-magnetofluidics: interactions between magnetism and fluid flow on the microscale. *J Microfluidics & nanofluidics* **12**, 1-16 (2012).
32. Hejazian, M., Li, W. & Nguyen, N.-T. Lab on a chip for continuous-flow magnetic cell separation. *Lab on a Chip* **15**, 959-970 (2015).
33. Ashkin, A., Dziedzic, J.M., Bjorkholm, J.E. & Chu, S. Observation of a single-beam gradient force optical trap for dielectric particles. *Optics letters* **11**, 288-290 (1986).
34. Yao, Z., Kwan, C.C. & Poon, A.W. An optofluidic “tweezer-and-drag” cell stretcher in a microfluidic channel. *Lab on a Chip* **20**, 601-613 (2020).
35. Moffitt, J.R., Chemla, Y.R., Smith, S.B. & Bustamante, C. Recent advances in optical tweezers. *Annu. Rev. Biochem.* **77**, 205-228 (2008).
36. Fan, X. & White, I.M. Optofluidic microsystems for chemical and biological analysis. *Nature photonics* **5**, 591-597 (2011).
37. Psaltis, D., Quake, S.R. & Yang, C. Developing optofluidic technology through the fusion of microfluidics and optics. *Nature* **442**, 381-386 (2006).
38. Friend, J. & Yeo, L.Y. Microscale acoustofluidics: Microfluidics driven via acoustics and ultrasonics. *Reviews of Modern Physics* **83**, 647 (2011).
39. Ozcelik, A. et al. Acoustic tweezers for the life sciences. *Nature methods* **15**, 1021-1028 (2018).
40. Gor'kov, L.P. On the forces acting on a small particle in an acoustical field in an ideal fluid. *Sov. Phys. Dokl.* **6**, 773-775 (1962).
41. Bruus, H. Acoustofluidics 7: The acoustic radiation force on small particles. *Lab Chip* **12**, 1014-1021 (2012).

42. King, L.V. On the acoustic radiation pressure on spheres. *Proc. R. Soc. London, Ser. A* **147**, 212-240 (1934).
43. Yosioka, K. & Kawasima, Y. Acoustic radiation pressure on a compressible sphere. *Acta Acust. Acust.* **5**, 167-173 (1955).
44. Schlichting, H. & Gersten, K. *Boundary-layer theory.* (Springer, 2016).
45. Eckart, C. Vortices and streams caused by sound waves. *Physical review* **73**, 68 (1948).
46. Rayleigh, L. On the circulation of air observed in Kundt's tubes, and on some allied acoustical problems. *Philosophical Transactions of the Royal Society of London* **175**, 1-21 (1884).
47. Wiklund, M., Green, R. & Ohlin, M. Acoustofluidics 14: Applications of acoustic streaming in microfluidic devices. *Lab on a Chip* **12**, 2438-2451 (2012).
48. Sadhal, S. Acoustofluidics 13: Analysis of acoustic streaming by perturbation methods. *Lab on a Chip* **12**, 2292-2300 (2012).
49. Sadhal, S. Acoustofluidics 15: Streaming with sound waves interacting with solid particles. *Lab on a Chip* **12**, 2600-2611 (2012).
50. Sadhal, S. Acoustofluidics 16: acoustics streaming near liquid–gas interfaces: drops and bubbles. *Lab on a Chip* **12**, 2771-2781 (2012).
51. Ahmed, D., Mao, X., Shi, J., Juluri, B.K. & Huang, T.J. A millisecond micromixer via single-bubble-based acoustic streaming. *Lab on a Chip* **9**, 2738-2741 (2009).
52. Schneider, M.F. et al. An acoustically driven microliter flow chamber on a chip ( $\mu$ FCC) for cell–cell and cell–surface interaction studies. *ChemPhysChem* **9**, 641-645 (2008).
53. Franke, T., Abate, A.R., Weitz, D.A. & Wixforth, A. Surface acoustic wave (SAW) directed droplet flow in microfluidics for PDMS devices. *Lab on a Chip* **9**, 2625-2627 (2009).
54. Huang, P.-H. et al. An acoustofluidic micromixer based on oscillating sidewall sharp-edges. *Lab on a Chip* **13**, 3847-3852 (2013).
55. Huang, P.-H. et al. A reliable and programmable acoustofluidic pump powered by oscillating sharp-edge structures. *Lab on a Chip* **14**, 4319-4323 (2014).
56. Connacher, W. et al. Micro/nano acoustofluidics: materials, phenomena, design, devices, and applications. *Lab Chip* **18**, 1952-1996 (2018).
57. Antfolk, M., Antfolk, C., Lilja, H., Laurell, T. & Augustsson, P. A single inlet two-stage acoustophoresis chip enabling tumor cell enrichment from white blood cells. *Lab Chip* **15**, 2102-2109 (2015).
58. Ku, A. et al. A urinary extracellular vesicle microRNA biomarker discovery pipeline; from automated extracellular vesicle enrichment by acoustic trapping to microRNA sequencing. *PloS one* **14**, e0217507 (2019).
59. Binkley, M. et al. Design, modeling, and experimental validation of an acoustofluidic platform for nanoscale molecular synthesis and detection. *Physics of Fluids* **31**, 082007 (2019).
60. Binkley, M.M., Cui, M., Berezin, M.Y. & Meacham, J.M. Antibody conjugate assembly on ultrasound-confined microcarrier particles. *ACS Biomaterials Science Engineering* **6**, 6108-6116 (2020).
61. Wu, M. et al. Circulating Tumor Cell Phenotyping via High - Throughput Acoustic Separation. *Small* **14**, 1801131 (2018).
62. Collins, D.J. et al. Two-dimensional single-cell patterning with one cell per well driven by surface acoustic waves. *Nat. Commun.* **6**, 8686 (2015).

63. Richard, C. et al. Blood platelet enrichment in mass-producible surface acoustic wave (SAW) driven microfluidic chips. *Lab Chip* (2019).
64. Kim, M. et al. Acoustic trap-and-release for rapid assessment of cell motility. *Soft Matter* **15**, 4266-4275 (2019).
65. Takatori, S.C., De Dier, R., Vermant, J. & Brady, J.F. Acoustic trapping of active matter. *Nature communications* **7**, 10694 (2016).
66. Bray, D. Cell movements: from molecules to motility. (Garland Science, 2000).
67. Pazour, G.J., Agrin, N., Walker, B.L. & Witman, G.B. Identification of predicted human outer dynein arm genes: candidates for primary ciliary dyskinesia genes. *Journal of medical genetics* **43**, 62-73 (2006).
68. Fliegauf, M., Benzing, T. & Omran, H. When cilia go bad: cilia defects and ciliopathies. *Nature reviews Molecular cell biology* **8**, 880-893 (2007).
69. Zariwala, M.A., Knowles, M.R. & Omran, H. Genetic defects in ciliary structure and function. *Annu. Rev. Physiol.* **69**, 423-450 (2007).
70. Christensen, S.T., Pedersen, L.B., Schneider, L. & Satir, P. Sensory cilia and integration of signal transduction in human health and disease. *Traffic* **8**, 97-109 (2007).
71. Marshall, W.F. The cell biological basis of ciliary disease. *Journal of Cell Biology* **180**, 17-21 (2008).
72. Antony, D. et al. Mutations in CCDC 39 and CCDC 40 are the major cause of primary ciliary dyskinesia with axonemal disorganization and absent inner dynein arms. *Human mutation* **34**, 462-472 (2013).
73. Hornef, N. et al. DNAH5 mutations are a common cause of primary ciliary dyskinesia with outer dynein arm defects. *American journal of respiratory & critical care medicine* **174**, 120-126 (2006).
74. Pazour, G.J. Comparative genomics: prediction of the ciliary and basal body proteome. *Current Biology* **14**, R575-R577 (2004).
75. Wirschell, M., Hendrickson, T. & Sale, W.S. Keeping an eye on II: II dynein as a model for flagellar dynein assembly and regulation. *Cell motility & the cytoskeleton* **64**, 569-579 (2007).
76. Bayly, P., Lewis, B., Kemp, P., Pless, R. & Dutcher, S. Efficient spatiotemporal analysis of the flagellar waveform of *Chlamydomonas reinhardtii*. *Cytoskeleton* **67**, 56-69 (2010).
77. Bottier, M., Thomas, K.A., Dutcher, S.K. & Bayly, P.V. How does cilium length affect beating? *Biophysical journal* **116**, 1292-1304 (2019).
78. Brokaw, C.J. Computer simulation of flagellar movement: I. Demonstration of stable bend propagation and bend initiation by the sliding filament model. *Biophysical Journal* **12**, 564-586 (1972).
79. Hines, M. & Blum, J. Bend propagation in flagella. I. Derivation of equations of motion and their simulation. *Biophysical Journal* **23**, 41-57 (1978).
80. Lindemann, C.B. & Kanous, K.S. "Geometric clutch" hypothesis of axonemal function: key issues and testable predictions. *Cell motility & the cytoskeleton* **31**, 1-8 (1995).
81. Riedel - Kruse, I.H., Hilfinger, A., Howard, J. & Jülicher, F. How molecular motors shape the flagellar beat. *HFSP journal* **1**, 192-208 (2007).
82. Bayly, P. & Dutcher, S. Steady dynein forces induce flutter instability and propagating waves in mathematical models of flagella. *Journal of The Royal Society Interface* **13**, 20160523 (2016).

83. Nicastro, D. et al. The molecular architecture of axonemes revealed by cryoelectron tomography. *Science* **313**, 944-948 (2006).
84. Pigino, G. et al. Cryoelectron tomography of radial spokes in cilia and flagella. *Journal of Cell Biology* **195**, 673-687 (2011).
85. Bui, K.H., Yagi, T., Yamamoto, R., Kamiya, R. & Ishikawa, T. Polarity and asymmetry in the arrangement of dynein and related structures in the Chlamydomonas axoneme. *Journal of Cell Biology* **198**, 913-925 (2012).
86. Holmes, J.A. & Dutcher, S.K. Cellular asymmetry in Chlamydomonas reinhardtii. *J. Cell Sci.* **94**, 273-285 (1989).
87. Cui, M., Kim, M., Weisensee, P.B. & Meacham, J.M. Thermal considerations for microswimmer trap-and-release using standing surface acoustic waves. *Lab on a Chip* (2021).
88. Silva, G.T. & Bruus, H. Acoustic interaction forces between small particles in an ideal fluid. *Physical Review E* **90**, 063007 (2014).
89. Muller, P.B., Barnkob, R., Jensen, M.J.H. & Bruus, H. A numerical study of microparticle acoustophoresis driven by acoustic radiation forces and streaming-induced drag forces. *Lab Chip* **12**, 4617-4627 (2012).
90. Tabeling, P. Introduction to microfluidics. (OUP Oxford, 2005).
91. Bruus, H. Theoretical microfluidics, Vol. 18. (Oxford university press Oxford, 2008).
92. Blackstock, D.T. (Acoustical Society of America, 2001).
93. Kinsler, L.E., Frey, A.R., Coppers, A.B. & Sanders, J.V. Fundamentals of acoustics. (John Wiley & Sons, 1999).
94. Skov, N.R., Bach, J.S., Winckelmann, B.G. & Bruus, H. 3D modeling of acoustofluidics in a liquid-filled cavity including streaming, viscous boundary layers, surrounding solids, and a piezoelectric transducer. *Aims Mathematics* **4**, 99-111 (2019).
95. Skov, N.R., Sehgal, P., Kirby, B.J. & Bruus, H. Three-dimensional numerical modeling of surface-acoustic-wave devices: Acoustophoresis of micro-and nanoparticles including streaming. *Physical Review Applied* **12**, 044028 (2019).
96. De Wagenaar, B. et al. Towards microfluidic sperm refinement: impedance-based analysis and sorting of sperm cells. *Lab Chip* **16**, 1514-1522 (2016).
97. Frank, T. & Tay, S. Flow-switching allows independently programmable, extremely stable, high-throughput diffusion-based gradients. *Lab Chip* **13**, 1273-1281 (2013).
98. Zeng, Y., Novak, R., Shuga, J., Smith, M.T. & Mathies, R.A. High-performance single cell genetic analysis using microfluidic emulsion generator arrays. *Anal. Chem.* **82**, 3183-3190 (2010).
99. Lee, D.-H., Li, X., Jiang, A. & Lee, A.P. An integrated microfluidic platform for size-selective single-cell trapping of monocytes from blood. *Biomicrofluidics* **12**, 054104 (2018).
100. Shi, J., Mao, X., Ahmed, D., Colletti, A. & Huang, T.J. Focusing microparticles in a microfluidic channel with standing surface acoustic waves (SSAW). *Lab Chip* **8**, 221-223 (2008).
101. Li, P. & Huang, T.J. Applications of Acoustofluidics in Bioanalytical Chemistry. *Anal. Chem.* **91**, 757-767 (2019).
102. Urbansky, A., Olm, F., Scheduling, S., Laurell, T. & Lenshof, A. Label-free separation of leukocyte subpopulations using high throughput multiplex acoustophoresis. *Lab Chip* **19**, 1406-1416 (2019).

103. Shields, C.W., Reyes, C.D. & Lopez, G.P. Microfluidic cell sorting: a review of the advances in the separation of cells from debulking to rare cell isolation. *Lab Chip* **15**, 1230-1249 (2015).
104. Augustsson, P., Barnkob, R., Wereley, S.T., Bruus, H. & Laurell, T. Automated and temperature-controlled micro-PIV measurements enabling long-term-stable microchannel acoustophoresis characterization. *Lab Chip* **11**, 4152-4164 (2011).
105. Leibacher, I., Reichert, P. & Dual, J. Microfluidic droplet handling by bulk acoustic wave (BAW) acoustophoresis. *Lab Chip* **15**, 2896-2905 (2015).
106. Rogers, P.R., Friend, J.R. & Yeo, L.Y. Exploitation of surface acoustic waves to drive size-dependent microparticle concentration within a droplet. *Lab Chip* **10**, 2979-2985 (2010).
107. Destgeer, G. et al. Microchannel anechoic corner for size-selective separation and medium exchange via traveling surface acoustic waves. *Anal. Chem.* **87**, 4627-4632 (2015).
108. Shi, J. et al. Acoustic tweezers: patterning cells and microparticles using standing surface acoustic waves (SSAW). *Lab Chip* **9**, 2890-2895 (2009).
109. Inui, T. et al. Focused surface acoustic wave locally removes cells from culture surface. *Lab Chip* **21**, 1299-1306 (2021).
110. Hu, X. et al. Versatile biomimetic array assembly by phase modulation of coherent acoustic waves. *Lab on a Chip* **20**, 3515-3523 (2020).
111. Hu, X. et al. On-chip hydrogel arrays individually encapsulating acoustic formed multicellular aggregates for high throughput drug testing. *Lab on a Chip* **20**, 2228-2236 (2020).
112. Rajapaksa, A.E. et al. Effective pulmonary delivery of an aerosolized plasmid DNA vaccine via surface acoustic wave nebulization. *Respir. Res.* **15**, 1-12 (2014).
113. Zarnitsyn, V.G. et al. Electrosonic ejector microarray for drug and gene delivery. *Biomed. Microdevices* **10**, 299-308 (2008).
114. Meacham, J.M., Durvasula, K., Degertekin, F.L. & Fedorov, A.G. Enhanced intracellular delivery via coordinated acoustically driven shear mechanoporation and electrophoretic insertion. *Sci. Rep.* **8**, 1-10 (2018).
115. McDonnell, A.G. et al. Motility induced changes in viscosity of suspensions of swimming microbes in extensional flows. *Soft Matter* **11**, 4658-4668 (2015).
116. Stegeman, G.W., Medina, D., Cutter, A.D. & Ryu, W.S. Neuro-genetic plasticity of *Caenorhabditis elegans* behavioral thermal tolerance. *BMC neuroscience* **20**, 1-12 (2019).
117. Miansari, M. et al. Inducing mild traumatic brain injury in *C. Elegans* via cavitation-free surface acoustic wave-driven ultrasonic irradiation. *Sci. Rep.* **9**, 1-11 (2019).
118. Takatori, S.C., De Dier, R., Vermant, J. & Brady, J.F. Acoustic trapping of active matter. *Nat. Commun.* **7**, 10694 (2016).
119. Jeong, J.S. et al. Particle manipulation in a microfluidic channel using acoustic trap. *J Biomedical Microdevices* **13**, 779-788 (2011).
120. Lee, J., Jeong, J.S. & Shung, K.K. Microfluidic acoustic trapping force and stiffness measurement using viscous drag effect. *J Ultrasonics* **53**, 249-254 (2013).
121. Chen, X. et al. An adjustable multi - scale single beam acoustic tweezers based on ultrahigh frequency ultrasonic transducer. *J Biotechnology Bioengineering* **114**, 2637-2647 (2017).

122. Augustsson, P., Magnusson, C., Nordin, M., Lilja, H. & Laurell, T. Microfluidic, label-free enrichment of prostate cancer cells in blood based on acoustophoresis. *Anal. Chem.* **84**, 7954-7962 (2012).
123. Fong, E.J. et al. Acoustic focusing with engineered node locations for high-performance microfluidic particle separation. *Analyst* **139**, 1192-1200 (2014).
124. Kim, M., Bayly, P.V. & Meacham, J.M. Motile cells as probes for characterizing acoustofluidic devices. *Lab Chip* **21**, 521-533 (2021).
125. Adams, J.D. et al. High-throughput, temperature-controlled microchannel acoustophoresis device made with rapid prototyping. *J. Micromech. Microeng.* **22**, 075017 (2012).
126. Wiklund, M. Acoustofluidics 12: Biocompatibility and cell viability in microfluidic acoustic resonators. *Lab Chip* **12**, 2018-2028 (2012).
127. Hawkes, J.J. & Coakley, W.T. Force field particle filter, combining ultrasound standing waves and laminar flow. *Sens. Actuators, B* **75**, 213-222 (2001).
128. Evander, M. et al. Noninvasive acoustic cell trapping in a microfluidic perfusion system for online bioassays. *Anal. Chem.* **79**, 2984-2991 (2007).
129. Johansson, L. et al. Temperature and trapping characterization of an acoustic trap with miniaturized integrated transducers—towards in-trap temperature regulation. *Ultrasonics* **53**, 1020-1032 (2013).
130. Kondoh, J., Shimizu, N., Matsui, Y., Sugimoto, M. & Shiokawa, S. Development of temperature-control system for liquid droplet using surface acoustic wave devices. *Sens. Actuators, A* **149**, 292-297 (2009).
131. Zheng, T., Wang, C., Hu, Q. & Wei, S. The role of electric field in microfluidic heating induced by standing surface acoustic waves. *Appl. Phys. Lett.* **112**, 233702 (2018).
132. Langelier, S.M., Yeo, L.Y. & Friend, J. UV epoxy bonding for enhanced SAW transmission and microscale acoustofluidic integration. *Lab Chip* **12**, 2970-2976 (2012).
133. Ha, B.H. et al. Acoustothermal heating of polydimethylsiloxane microfluidic system. *Sci. Rep.* **5**, 11851 (2015).
134. Schroda, M., Hemme, D. & Muhlhaus, T. The *Chlamydomonas* heat stress response. *Plant J* **82**, 466-480 (2015).
135. Xie, B. et al. *Chlamydomonas reinhardtii* thermal tolerance enhancement mediated by a mutualistic interaction with vitamin B<sub>12</sub>-producing bacteria. *ISME J.* **7**, 1544-1555 (2013).
136. Jo, M.C. & Guldiken, R. Effects of polydimethylsiloxane (PDMS) microchannels on surface acoustic wave-based microfluidic devices. *Microelectron. Eng.* **113**, 98-104 (2014).
137. Cui, M., Binkley, M., Shekhani, H., Berezin, M. & Meacham, J. Augmented longitudinal acoustic trap for scalable microparticle enrichment. *Biomicrofluidics* **12**, 034110 (2018).
138. Satyanarayana, S., Karnik, R.N. & Majumdar, A. Stamp-and-stick room-temperature bonding technique for microdevices. *J. Microelectromech. Syst.* **14**, 392-399 (2005).
139. Sager, R. & Granick, S. Nutritional studies with *Chlamydomonas reinhardtii*. *Ann. N. Y. Acad. Sci.* **56**, 831-838 (1953).
140. Kobayashi, Y. et al. Algae sense exact temperatures: small heat shock proteins are expressed at the survival threshold temperature in *Cyanidioschyzon merolae* and *Chlamydomonas reinhardtii*. *Genome Biol. Evol.* **6**, 2731-2740 (2014).

141. Tanaka, Y., Nishiyama, Y. & Murata, N. Acclimation of the photosynthetic machinery to high temperature in *Chlamydomonas reinhardtii* requires synthesis de novo of proteins encoded by the nuclear and chloroplast genomes. *Plant Physiol.* **124**, 441-450 (2000).
142. Winkler, A., Brünig, R., Faust, C., Weser, R. & Schmidt, H. Towards efficient surface acoustic wave (SAW)-based microfluidic actuators. *Sens. Actuators, A* **247**, 259-268 (2016).
143. Ng, J.W., Devendran, C. & Neild, A. Acoustic tweezing of particles using decaying opposing travelling surface acoustic waves (DOTSAW). *Lab Chip* **17**, 3489-3497 (2017).
144. Golobic, I., Petkovsek, J., Baselj, M., Papez, A. & Kenning, D. Experimental determination of transient wall temperature distributions close to growing vapor bubbles. *Heat Mass Transfer* **45**, 857-866 (2009).
145. Gibbons, M., Howe, C., Di Marco, P. & Robinson, A. Local heat transfer to an evaporating sessile droplet in an electric field. *J. Phys.: Conf. Ser.* **745**, 032066 (2016).
146. Gibbons, M., Di Marco, P. & Robinson, A.J. Local heat transfer to an evaporating superhydrophobic droplet. *Int. J. Heat Mass Transfer* **121**, 641-652 (2018).
147. Qi, W., Li, J. & Weisensee, P.B. Evaporation of Sessile Water Droplets on Horizontal and Vertical Biphobic Patterned Surfaces. *Langmuir* **35**, 17185-17192 (2019).
148. Qi, W. & Weisensee, P.B. Dynamic wetting and heat transfer during droplet impact on bi-phobic wettability-patterned surfaces. *Physics of Fluids* **32**, 067110 (2020).
149. Ross, D., Gaitan, M. & Locascio, L.E. Temperature measurement in microfluidic systems using a temperature-dependent fluorescent dye. *Anal. Chem.* **73**, 4117-4123 (2001).
150. Nakano, A., Luo, J. & Ros, A. Temporal and spatial temperature measurement in insulator-based dielectrophoretic devices. *Analytical Chemistry* **86**, 6516-6524 (2014).
151. Narayanan, S., Fedorov, A.G. & Joshi, Y.K. in 2010 12th IEEE Intersociety Conference on Thermal and Thermomechanical Phenomena in Electronic Systems 1-10 (IEEE, 2010).
152. Mao, Z. et al. Experimental and numerical studies on standing surface acoustic wave microfluidics. *Lab Chip* **16**, 515-524 (2016).
153. Johansson, L. et al. Surface acoustic wave-induced precise particle manipulation in a trapezoidal glass microfluidic channel. *Journal of Micromechanics Microengineering* **22**, 025018 (2012).
154. Sekiguchi, M., Kameda, S., Kurosawa, S., Yoshida, M. & Yoshimura, K. Thermotaxis in *Chlamydomonas* is brought about by membrane excitation and controlled by redox conditions. *Scientific Reports* **8**, 1-10 (2018).
155. Gui, M. et al. Structures of radial spokes and associated complexes important for ciliary motility. *Nature structural & molecular biology* **28**, 29-37 (2021).
156. Horani, A. et al. Establishment of the early cilia preassembly protein complex during motile ciliogenesis. *Proceedings of the National Academy of Sciences* **115**, E1221-E1228 (2018).
157. Reiter, J.F. & Leroux, M.R. Genes and molecular pathways underpinning ciliopathies. *Nature reviews Molecular cell biology* **18**, 533-547 (2017).
158. Leigh, M.W. et al. Clinical and genetic aspects of primary ciliary dyskinesia/Kartagener syndrome. *Genetics in Medicine* **11**, 473-487 (2009).
159. Ibañez-Tallon, I. et al. Dysfunction of axonemal dynein heavy chain Mdnah5 inhibits ependymal flow and reveals a novel mechanism for hydrocephalus formation. *Human molecular genetics* **13**, 2133-2141 (2004).

160. Merchant, S.S. et al. The Chlamydomonas genome reveals the evolution of key animal and plant functions. *Science* **318**, 245-250 (2007).
161. Geyer, V.F., Jülicher, F., Howard, J. & Friedrich, B.M. Cell-body rocking is a dominant mechanism for flagellar synchronization in a swimming alga. *Proceedings of the National Academy of Sciences* **110**, 18058-18063 (2013).
162. Geyer, V.F., Sartori, P., Friedrich, B.M., Jülicher, F. & Howard, J. Independent control of the static and dynamic components of the Chlamydomonas flagellar beat. *Current Biology* **26**, 1098-1103 (2016).
163. Guasto, J.S., Johnson, K.A. & Gollub, J.P. Oscillatory flows induced by microorganisms swimming in two dimensions. *Physical review letters* **105**, 168102 (2010).
164. Brumley, D.R., Wan, K.Y., Polin, M. & Goldstein, R.E. Flagellar synchronization through direct hydrodynamic interactions. *Elife* **3**, e02750 (2014).
165. Wan, K.Y. & Goldstein, R.E. Coordinated beating of algal flagella is mediated by basal coupling. *Proceedings of the National Academy of Sciences* **113**, E2784-E2793 (2016).
166. Ruffer, U. & Nultsch, W. High - speed cinematographic analysis of the movement of Chlamydomonas. *Cell motility* **5**, 251-263 (1985).
167. Min, T.L. et al. High-resolution, long-term characterization of bacterial motility using optical tweezers. *Nature methods* **6**, 831-835 (2009).
168. Zhang, Z., Kimkes, T.E. & Heinemann, M. Manipulating rod-shaped bacteria with optical tweezers. *Scientific reports* **9**, 1-9 (2019).
169. Jones, C. et al. Stochastic force dynamics of the model microswimmer Chlamydomonas reinhardtii: Active forces and energetics. *Physical Review E* **103**, 032403 (2021).
170. Peterman, E.J., Gittes, F. & Schmidt, C.F. Laser-induced heating in optical traps. *Biophysical journal* **84**, 1308-1316 (2003).
171. Daldrop, P., Brutzer, H., Huhle, A., Kauert, D.J. & Seidel, R. Extending the range for force calibration in magnetic tweezers. *Biophysical journal* **108**, 2550-2561 (2015).
172. Van Oene, M.M. et al. Biological magnetometry: torque on superparamagnetic beads in magnetic fields. *Physical review letters* **114**, 218301 (2015).
173. Krishnan, M., Mojarad, N., Kukura, P. & Sandoghdar, V. Geometry-induced electrostatic trapping of nanometric objects in a fluid. *Nature* **467**, 692-695 (2010).
174. Zhang, P. et al. Acoustoelectronic nanotweezers enable dynamic and large-scale control of nanomaterials. *Nature Communications* **12**, 1-10 (2021).
175. Durmus, N.G. et al. Magnetic levitation of single cells. *Proceedings of the National Academy of Sciences* **112**, E3661-E3668 (2015).
176. Itoh, H. et al. Mechanically driven ATP synthesis by F<sub>1</sub>-ATPase. *Nature* **427**, 465-468 (2004).
177. Li, Q., Li, S., Zhang, X., Xu, W. & Han, X. Programmed magnetic manipulation of vesicles into spatially coded prototissue architectures arrays. *Nature communications* **11**, 1-9 (2020).
178. Ruiz-Hernandez, E., Baeza, A. & Vallet-Regi, M. Smart drug delivery through DNA/magnetic nanoparticle gates. *ACS nano* **5**, 1259-1266 (2011).
179. Guo, F. et al. Three-dimensional manipulation of single cells using surface acoustic waves. *Proceedings of the National Academy of Sciences* **113**, 1522-1527 (2016).
180. Wu, M. et al. Isolation of exosomes from whole blood by integrating acoustics and microfluidics. *Proceedings of the National Academy of Sciences* **114**, 10584-10589 (2017).

181. Goldstein, R.E., Polin, M. & Tuval, I. Noise and synchronization in pairs of beating eukaryotic flagella. *Physical review letters* **103**, 168103 (2009).
182. Brokaw, C., Luck, D. & Huang, B. Analysis of the movement of Chlamydomonas flagella: the function of the radial-spoke system is revealed by comparison of wild-type and mutant flagella. *The Journal of Cell Biology* **92**, 722-732 (1982).
183. Hyams, J.S. & Borisy, G.G. Isolated flagellar apparatus of Chlamydomonas: characterization of forward swimming and alteration of waveform and reversal of motion by calcium ions in vitro. *Journal of Cell Science* **33**, 235-253 (1978).
184. Qin, B., Gopinath, A., Yang, J., Gollub, J.P. & Arratia, P.E. Flagellar kinematics and swimming of algal cells in viscoelastic fluids. *Scientific reports* **5**, 1-7 (2015).
185. Ruffer, U. & Nultsch, W. Flagellar coordination in Chlamydomonas cells held on micropipettes. *Cell motility and the cytoskeleton* **41**, 297-307 (1998).
186. Dutcher, S.K. Asymmetries in the cilia of Chlamydomonas. *Philosophical Transactions of the Royal Society B* **375**, 20190153 (2020).
187. Bayly, P. et al. Propulsive forces on the flagellum during locomotion of Chlamydomonas reinhardtii. *Biophysical journal* **100**, 2716-2725 (2011).
188. Leptos, K.C. et al. Antiphase synchronization in a flagellar-dominance mutant of Chlamydomonas. *Physical review letters* **111**, 158101 (2013).
189. Cortese, D. & Wan, K.Y. Control of helical navigation by three-dimensional flagellar beating. *Physical Review Letters* **126**, 088003 (2021).
190. Wilson, K.S., Gonzalez, O., Dutcher, S.K. & Bayly, P.V. Dynein - deficient flagella respond to increased viscosity with contrasting changes in power and recovery strokes. *Cytoskeleton* **72**, 477-490 (2015).
191. Brokaw, C.J. & Luck, D. Bending patterns of chlamydomonas flagella I. Wild - type bending patterns. *Cell motility* **3**, 131-150 (1983).
192. Brokaw, C. & Luck, D. Bending patterns of Chlamydomonas flagella: III. A radial spoke head deficient mutant and a central pair deficient mutant. *Cell motility* **5**, 195-208 (1985).
193. Dell, A.I., Pawar, S. & Savage, V.M. Systematic variation in the temperature dependence of physiological and ecological traits. *Proceedings of the National Academy of Sciences* **108**, 10591-10596 (2011).
194. Majima, T. & Fumio, O. Response of Chlamydomonas to temperature change. *The Journal of Protozoology* **22**, 499-501 (1975).
195. Beveridge, O.S., Petchey, O.L. & Humphries, S. Mechanisms of temperature-dependent swimming: the importance of physics, physiology and body size in determining protist swimming speed. *Journal of Experimental Biology* **213**, 4223-4231 (2010).
196. Humphries, S. A physical explanation of the temperature dependence of physiological processes mediated by cilia and flagella. *Proceedings of the National Academy of Sciences* **110**, 14693-14698 (2013).
197. Kim, M., Barnkob, R. & Meacham, J.M. Rapid measurement of the local pressure amplitude in microchannel acoustophoresis using motile cells. *arXiv preprint arXiv:201441* (2021).
198. Ledbetter, A.D., Shekhani, H.N., Binkley, M.M. & Meacham, J.M. Tuning the coupled-domain response for efficient ultrasonic droplet generation. *IEEE transactions on ultrasonics, ferroelectrics & frequency control* **65**, 1893-1904 (2018).

199. Barnkob, R., Augustsson, P., Laurell, T. & Bruus, H. Acoustic radiation- and streaming-induced microparticle velocities determined by microparticle image velocimetry in an ultrasound symmetry plane. *Physical Review E* **86**, 056307 (2012).
200. Barnkob, R., Augustsson, P., Laurell, T. & Bruus, H. Measuring the local pressure amplitude in microchannel acoustophoresis. *Lab on a Chip* **10**, 563-570 (2010).
201. Barnkob, R., Iranmanesh, I., Wiklund, M. & Bruus, H. Measuring acoustic energy density in microchannel acoustophoresis using a simple and rapid light-intensity method. *Lab on a Chip* **12**, 2337-2344 (2012).
202. Thalhammer, G. et al. Combined acoustic and optical trapping. *Biomedical optics express* **2**, 2859-2870 (2011).
203. Bassindale, P., Phillips, D., Barnes, A. & Drinkwater, B. Measurements of the force fields within an acoustic standing wave using holographic optical tweezers. *Applied Physics Letters* **104**, 163504 (2014).
204. Lamprecht, A., Lakämper, S., Baasch, T., Schaap, I.A. & Dual, J. Imaging the position-dependent 3D force on microbeads subjected to acoustic radiation forces and streaming. *Lab on a Chip* **16**, 2682-2693 (2016).
205. Cacace, T. et al. Retrieving acoustic energy densities and local pressure amplitudes in microfluidics by holographic time-lapse imaging. *Lab on a Chip* **18**, 1921-1927 (2018).